



Norwegian University of
Science and Technology

Wet Gas Compression - Transients

Håkon Myklestad

Natural Gas Technology

Submission date: June 2017

Supervisor: Lars Eirik Bakken, EPT

Co-supervisor: Tor Bjørge, EPT
Martin Bakken, EPT
Erik Langørgen, EPT

Norwegian University of Science and Technology
Department of Energy and Process Engineering

EPT-M-2017-53

MASTER THESIS

for

Student Håkon Myklestad

Spring 2017

Wet Gas Compression – Transients*Våtgass Kompresjon - Transienter***Background and objective**

Natural gas is one key to reduce emission and optimize efficiency. Increased production of gas demands new field development based on sub-sea production. Several wet gas compressors have been installed subsea at Gullfaks and Åsgard and novel experience from first operating phases is achieved.

Operation of subsea wet gas compressors represents challenges related to transient response at low flow condition. Of specific interest is to document transients close to surge at different impeller configurations and variations in gas mass fraction. Advanced techniques for transient detection, analyses and comparison between different cases are prioritised. Test data should be based on the existing NTNU wet gas compressor test rig.

The following tasks are to be considered:

1. Literature review to document different techniques to detect and analyse transients. The techniques should preferably be compatible to existing test rig equipment.
2. Propose and conduct transient tests at the surge area of the characteristic. Two impeller configurations, including dry and wet conditions should be covered.
3. Analyse and compare the different test cases. Guidelines of acceptable “transient” levels to be included in the documentation.

Within 14 days of receiving the written text on the master thesis, the candidate shall submit a research plan for his project to the department.

When the thesis is evaluated, emphasis is put on processing of the results, and that they are presented in tabular and/or graphic form in a clear manner, and that they are analyzed carefully.

The thesis should be formulated as a research report with summary both in English and Norwegian, conclusion, literature references, table of contents etc. During the preparation of the text, the candidate should make an effort to produce a well-structured and easily readable report. In order to ease the evaluation of the thesis, it is important that the cross-references are correct. In the making of the report, strong emphasis should be placed on both a thorough discussion of the results and an orderly presentation.

The candidate is requested to initiate and keep close contact with his/her academic supervisor(s) throughout the working period. The candidate must follow the rules and regulations of NTNU as well as passive directions given by the Department of Energy and Process Engineering.


Risk assessment of the candidate's work shall be carried out according to the department's procedures. The risk assessment must be documented and included as part of the final report. Events related to the candidate's work adversely affecting the health, safety or security, must be documented and included as part of the final report. If the documentation on risk assessment represents a large number of pages, the full version is to be submitted electronically to the supervisor and an excerpt is included in the report.

Pursuant to “Regulations concerning the supplementary provisions to the technology study program/Master of Science” at NTNU §20, the Department reserves the permission to utilize all the results and data for teaching and research purposes as well as in future publications.

The final report is to be submitted digitally in DAIM. An executive summary of the thesis including title, student's name, supervisor's name, year, department name, and NTNU's logo and name, shall be submitted to the department as a separate pdf file. Based on an agreement with the supervisor, the final report and other material and documents may be given to the supervisor in digital format.

- Work to be done in lab (Water power lab, Fluids engineering lab, Thermal engineering lab)
- Field work

Department of Energy and Process Engineering, 15. January 2017



L E Bakken
Academic Supervisor

Research Advisor:
T. Bjørge
M. Bakken
E. Langørgen

ABSTRACT

Today, most of the large and easily accessible oil and gas fields on the Norwegian continental shelf has been developed. Future production potential is found in development of fields at large depths and cost-efficient methods of improving the recovery of existing fields at the tail production stage. Development of wet gas compression technology for subsea boosting is one pathway to achieving this.

Introducing multiphase flow into the already complex flow pattern inside compressors makes it challenging to develop accurate analytical models. Current research is therefore highly dependent on test data from real scale compressor rigs. One such compressor rig is built at the Department of Energy and Process Engineering.

This thesis focus on transients aerodynamics phenomenons in centrifugal compressors. These primarily occur at low flow rate where the compressors performance is limited by stall and surge. Encountering stall or surge is highly unwanted during operation and it is therefore of interest to investigate how wet gas affect them. A compressor that is exposed directly to the wellstream also needs to handle inlet instabilities in the form of liquid content fluctuations, especially if the downstream pipelines are prone to slug formation. This is a unique challenge for wet gas compressors.

A vibration approach is taken, and the author has focused on analysis of frequency spectra, primarily based on dynamic pressure readings in the diffuser. The results show a mild increase of noise during wet conditions due to the dispersed liquid droplets causing reflection of pressure waves. Left limit tests suggest that the compressor encounters impeller rotating stall that is severe enough to cause flow instabilities, but no signs of surge oscillations are seen. The same is observed for wet gas, but this occurs at a lower flow rate. Slug tests performed in the surge area gives no indication of instability, as the stall cells are immediately re-energized and no excitations are observed around the rotors natural frequency.

SAMMENDRAG

De fleste av de store og tilgjengelige olje- og gassfeltene på den norske kontinentalsokker har blitt utvunnet. Fremtidens potensial finnes i utvikling av felt i dypt vann og kostnadseffektive metoder for å øke utvinningsgraden i felt som er inne i sin haleproduksjon. Utvikling av våtgasskompressor- teknologi til anvending subsea for å akselerere produksjonen er en vei mot dette målet.

Tilsetning av væske i det allerede kompliserte strømningsmønsteret i kompressorer gjør det vanskelig å utvikle nøyaktige analytiske modeller. Nåværende forskning er i stor grad avhengig av testdata fra kompressorrigger i reell skala. En slik rigg er bygd ved Institutt for energi- og prosessteknikk.

Denne avhandlingen fokuserer på transiente aerodynamiske fenomen i sentrifugalkompressorer. Disse oppstår primært ved lav væskestrømning hvor kompressorlytelsen er begrenset av stall og surge. Stall og surge kan føre til store skader på kompressorssystemet og det er derfor ønskelig å undersøke hvilken innvirkning våtgass vil ha. En kompressor som er direkte eksponert for brønnstrømmen vil også måtte være kapabel til å håndtere innløpsustabilitet i form av væskefluktuasjoner, spesielt hvis rørsystemet nedstrøms er utsatt for slug.

Opgaven tar utgangspunkt i vibrasjonsteori, og det er fokusert på analyse av frekvensspektra, primært basert på data fra dynamiske trykkmålinger i diffusoren. Resultatene viser en mild økning av støy under våte forhold på grunn av ekkoeffektene som væskedråpene fører med seg. Tester i kompressorens surgeområde viser at roterene stall i løpehjulet begrenser kapasiteten og er kraftig nok til å påvirke kompressoress stabilitet, men ingen surgesvingninger er observert. Det samme er tilfelle for våtgass, men dette skjer ved lavere strømningsrate. Sluttester gjennomført i surgeområdet gir ingen tegn til ustabilitet - stallcellene blir umiddelbart "vasket vekk", og ingen eksitasjoner er observert ved rotorens naturlige frekvens.

PREFACE

The work presented in this thesis is performed during the spring of 2017 and concludes my Master of Science program at the Norwegian University of Science and Technology, at the Department of Energy and Process Engineering.

First of all, I would like to thank my supervisor, Professor Lars Eirik Bakken for providing excellent guidance for this thesis. I would also like to thank my co-supervisors Tor Bjørge for his support.

In addition, I would like to thank PhD Candidate Martin Bakken and lab engineer Erik Langørgen for professional experimental guidance and valuable advice.

Finally, thanks to my fellow Master student, Martin Henriksen for great motivation and interesting discussions.

Håkon Myklestad
Trondheim, 11th of June 2017

Contents

List of figures	ix
List of tables	xiii
Nomenclature	xv
1 Introduction	1
1.1 Background: Subsea processing	1
1.2 Multiphase flow	3
1.3 Previous work	5
1.4 Project scope	6
2 Centrifugal Compressor Flow Dynamics	7
2.1 Viscous effects	8
2.2 Impeller	11
2.2.1 Flow analysis	11
2.2.2 Multiphase effects	16
2.3 Vaneless diffuser	17
2.3.1 Flow analysis	17
2.3.2 Multiphase effects	19
2.4 Volute	20
2.4.1 Flow analysis	20
2.4.2 Multiphase effects	22
2.5 Summary	22
3 Vibration and Spectrum Analysis	23
3.1 One dimensional vibration	23
3.1.1 Free vibration	23
3.1.2 Forced Vibration	25
3.2 Application to Rotor Vibration	28
3.2.1 Free Vibration	28
3.2.2 Forced Vibration	29
3.3 Spectrum Analysis	30
3.3.1 The Fast Fourier Transform	30
3.3.2 Wavelet transform	34
3.4 Signal detection	35
3.5 Attenuation	37
4 Compressor Instabilities	41
4.1 Stall	41

4.1.1	Impeller rotating stall	41
4.1.2	Diffuser rotating stall	43
4.2	Surge	45
4.3	Wet gas stall and surge	48
4.4	Dynamic surge detection	50
4.5	Slug	52
4.6	Wet gas rotor stability	55
4.7	Summary	56
5	Experimental Campaign	59
5.1	Test rig	59
5.2	Test matrices	63
5.3	Results	64
5.3.1	Steady state	64
5.3.2	Left Limit	69
5.3.3	Slug	75
6	Conclusion	83
A	Appendix	91
A.1	Derivation of Helmholtz Frequency	91
A.2	Estimating the Helmholtz Frequency	92
A.3	Research Plan	95
A.4	Risk Assessment	96

List of Figures

1.1	The subsea factory [45].	2
1.2	Relationship between GMF and GVF.	3
1.3	Regime map for multiphase flow	4
2.1	Pressure and velocity through a centrifugal compressor [9].	7
2.2	Viscous flow over a flat plate [7].	8
2.3	Boundary layer flow separation around a circular cylinder [54].	9
2.4	Boundary layer evolution across a curved surface.	10
2.5	Impeller geometry and force balance [55].	12
2.6	Velocity measurements by Eckardt in a radial impeller [18].	14
2.7	Boundary layer instability.	14
2.8	Slip in a backswept impeller.	15
2.9	Leakage design recommendations [39].	16
2.10	Liquid accumulation by compressor inlet. Fluorescent liquid was injected into the labyrinth seal to confirm the source [20].	17
2.11	Diffuser flow.	19
2.12	Symmetrical volute geometry [14].	21
3.1	Spring-mass system.	24
3.2	Damping of a spring-mass system.	24
3.3	Damped spring-mass system [40].	27
3.4	Rotor system model [40].	28
3.5	The principle of the Fourier transform [13].	31
3.6	Spectral leakage in FFT.	32
3.7	The effect of windowing.	33
3.8	Spectrum with noise and signal with associated spur and noise [31].	34
3.9	Time-Frequency resolution	35
3.10	Vibration and dynamic pressure spectra [40].	37
3.11	Speed of sound in homegenous water/air mixture.	38
3.12	Pressure wave propagation across boundary.	38
4.1	Impeller inlet velocity diagram.	42
4.2	Impeller rotating stall [53].	42
4.3	The principle of diffuser rotating stall.	43
4.4	Diffuser rotating stall [44].	44
4.5	Part-span stall and full-span stall [14].	44
4.6	Extended compressor curve and deep surge	46
4.7	Compressor system with exit duct and plenum [21].	47

4.8	Flow coefficient calculated from hotwire velocity measurement and plenum mass balance during surge [21].	48
4.9	Dynamic surge detection based on diffuser boundary layer probes [8].	50
4.10	Velocity profile in diffuser towards surge [29].	51
4.11	Dynamic surge detection based on inlet measurements [41]	52
4.12	Formation of hydrodynamic slug [4].	53
4.13	Formation of terrain slug [42].	53
4.14	Variation of momentum in impeller [6].	54
4.15	Vibration trend at increasing liquid content[62].	56
5.1	Cross-section of the centrifugal compressor at test facility [20].	60
5.2	Test rig PID.	60
5.3	Compressor block with diffuser instruments.	61
5.4	Test rig compression system.	62
5.5	Estimated Helmholtz frequency of compression system.	62
5.6	Compressor characteristics at 9000 rpm.	65
5.7	Fourier transform at $\phi=0.048$ and 100%GMF (Hanning window). . .	65
5.8	Magnitude of the zero-frequency component.	66
5.9	Steady state profile at compressor outlet pipe, 100%GMF (Hanning window).	67
5.10	Steady state profile at compressor outlet pipe, 60%GMF (Hanning window).	67
5.11	Signal quality at different GMF.	68
5.12	Steady state dynamic pressure profile at impeller outlet, 100%GMF .	69
5.13	Steady state dynamic pressure profile at impeller outlet, 60%GMF. .	69
5.14	100%GMF: Different analysis methods.	70
5.15	Left limit test 100%GMF: Impeller outlet.	71
5.16	Left limit test 100%GMF: Diffuser outlet.	72
5.17	Left limit test 100%GMF: Outlet pipe.	72
5.18	Left limit test 90%GMF: Impeller outlet.	73
5.19	Left limit test 90%GMF: Diffuser outlet.	73
5.20	Calculated GMF during wet gas left limit test.	74
5.21	Backflow during wet gas left limit test.	74
5.22	Compressor characteristics during left limit test at 100%GMF.	74
5.23	Compressor characteristics during left limit test at 90%GMF.	75
5.24	Superimposed compressor characteristics during left limit tests. . . .	75
5.25	Window comparison during slug test.	76
5.26	90%GMF at $\phi = 0.28$	76
5.27	90%GMF at $\phi = 0.24$	77
5.28	80%GMF at $\phi = 0.28$	77
5.29	80%GMF at $\phi = 0.24$	78
5.30	100%GMF at $\phi = 0.28$	78
5.31	100%GMF at $\phi = 0.24$	79
5.32	Outlet pressure during sequential slug injection at $\phi = 0.034$ with 80%GMF.	80

5.33	Pressure and flow during sequential slug injection at $\phi = 0.034$ with 80%GMF.	80
A.1	Helmholtz resonator.	91
A.2	Test rig volute geometry.	93
A.3	Test rig compression system.	93

List of Tables

3.1	National Instruments recommendation for FFT window choice.	33
5.1	Steady state test matrix.	63
5.2	Left limit test matrix.	63
5.3	Slug test matrix.	64
5.4	Slug sequence test matrix	64
A.1	Plenum measurements.	93
A.2	Compressor parameters	94

Nomenclature

Do not refer to symbols in the nomenclature when reading Section 3.1.

Roman Letters

Symbol	Description	Unit
A	Area	m^2
B	Greitzer's surge parameter	–
C	Absolute velocity	m/s
D	Diameter	m
F	Force	N
M	Mach number	–
N	Rotational speed	rpm
Q	Volumetric flow rate	m^3/s
R	Radius of curvature	m
R_0	Rossby Number	–
Re	Reynolds number	–
V	Volume	m^3
W	Relative velocity	m/s
U	Impeller blade velocity	m/s
a	Acceleration	m/s^2
a	Speed of sound	m/s
b	Width	m
c	Absolute velocity	m/s
f	Frequency	Hz
l	Length	m
m	Mass	kg
\dot{m}	Mass flow rate	kg/s
r	Radius	m
s	Streamline distance	m
u	Velocity	m/s

Greek Letters

Symbol	Description	Unit
α	Logarithmical spiral angle	$^{\circ}$
γ	Blade to blade surface inclination	$^{\circ}$
δ	Density ratio	—
δ	Boundary layer thickness	m
θ	Angular position	$^{\circ}$
μ	Dynamic viscosity	$kg/(s \cdot m)$
ν	Kinematic viscosity	m^2/s
ρ	Density	kg/m^3
σ	Surface tension	N/m
ϕ	Flow coefficient	—
ω	Angular velocity	rad/s

Subscripts

Symbol	Description
0	Stagnation
1	Impeller inlet
2	Impeller outlet
3	Diffuser outlet
C	Characteristic
H	Helmholtz
v	Volute
d	Droplet
g	Gas
l	Liquid
m	Mean
mp	Multiphase
p	Plenum
s	Superficial
t	Thrust
θ	Radial direction
∞	Outer region

Acronyms

Symbol	Description
ACD	Analog-to-Digital Converters
ASME	American Society of Mechanical Engineers
BPF	Blade Passing Frequency
CFD	Computational Fluid Dynamics
CWT	Continuous Wavelet Transform
FFT	Fast Fourier Transform
GMF	Gas Mass Fraction
GMRC	Gas Machinery Research Council
GVF	Gas Volume Fraction
HC	Hydrocarbon
LMF	Liquid Mass Fraction
LVF	Liquid Volume Fraction
NTNU	Norwegian University of Science and Technology
PMMA	Polymethyl methacrylate
PID	Piping and Instrumentation Diagram
PIV	Particle Image velocimetry
PSD	Power Spectral Density
PXI	PCI eXtensions for Instrumentation
SNR	Signal-to-noise ratio
SINAD	Signal-to-Noise and Distortion Ratio
VSD	Variable Speed Drive

INTRODUCTION

1.1 Background: Subsea processing

Today, most of the known large and accessible oil and gas fields on the Norwegian continental shelf has been developed. Future production potential is found in development of fields in harsh conditions at large depths, as well as in cost-efficient methods of improving the recovery of existing fields at the tail production stage. In a time of decreased oil price and global climate challenges this calls for new technological solutions.

As production moves into deeper water, construction of production platforms becomes more expensive, if not impossible. It has become increasingly apparent that subsea solutions is the way forward. In recent years, technology development has made it increasingly viable to incorporate processing tasks such as separation, water injection and wellstream boosting in subsea facilities.

The first experimentation on subsea separation systems goes all the way back to the 60's, but the Statoil Troll C pilot on water separation and injection in 2001 is by most regarded as the first modern subsea separation unit. The Troll system was installed in 340 meters of water depth, 3.5 kilometer from its host platform. Several subsea separation systems has been installed since, and the Perdido field in the Gulf of Mexico is currently the deepest application of subsea separation at approximately 2,500 meters [43].

The first subsea booster pump was a twin-screw multiphase pump installed at the Prezioso field in Italy in 1994. Since this first installation at only 50 meters, the technology has continuously been taken deeper. The Cascade oil field in the Gulf of Mexico is currently the deepest subsea boosting system installed, at a water depth of close to 2,500 meters [43]. Although the first multiphase booster pump was a twin-screw machine, it is the helico-axial pumps that has captured most of the market today. The booster technology for liquid dominated wellstreams is currently the most mature among subsea processing technologies.

For gas dominated wellstreams the story is different. Subsea wet gas compression is a technology under development and remains to be proven. Statoil is the main motivator for this technology and has acquired novel experience from two different systems. A compressor station was installed at Åsgard in june 2015, and at Gullfaks

later the same year. The compressor at Åsgard relies on separation of liquid from the well stream before compression. It is fed by reservoirs from Midgard, where the recovery factor is expected to rise from 71-86%; and Mikkel, where the recovery factor is expected to rise from 46-68%.

The work presented in this thesis relates to a system which feeds the wellstream directly into the compressor without pre-separation. This solution is relevant for gas/condensate fields that have a low liquid content. All compressors in traditional gas processing are protected by scrubbers, and this concept is therefore radical in that it defies the general industry consensus that the presence of liquids is highly unwanted in compressors. The constraints related to size, complexity and reliability are strict when installing subsea systems. Employing systems that avoid large footprint separators that require maintenance and complex control systems is therefore an attractive option.

The compressor station at Gullfaks was installed without a separation system, and it is therefore known to be the first true *wet gas compressors*. It was placed at a depth of 135 meters, 15 km from the Gullfaks C station, and two counter-rotating axial compressors were used for boosting the wet gas. However, this machine was retrieved later the same year due to leakage in an umbilical line [19].

Subsea processing is a field where technology elements remains to be proven. Rystad energy [43] estimates that as of 2015 there are 30 active liquid boosting projects, 15 separation projects and 3 compression projects worldwide. Among the challenges are power distribution, control systems, monitoring, maintenance and cost. For wet gas compression, as will become more apparent throughout this thesis, there are still many questions to be answered about the fundamental physics. The field of research is new, and the erratic behaviour of multiphase flow makes development of accurate analytical tools difficult. Experimental data from real scale compressors is therefore vital. Ongoing research aims to develop compressors that can operate in wet conditions while maintaining high performance levels.

Statoil envisions a future where "subsea factories" to a large extent has replaced topside facilities. Figure 1.1 displays an artist's impression of what such a facility may look like.

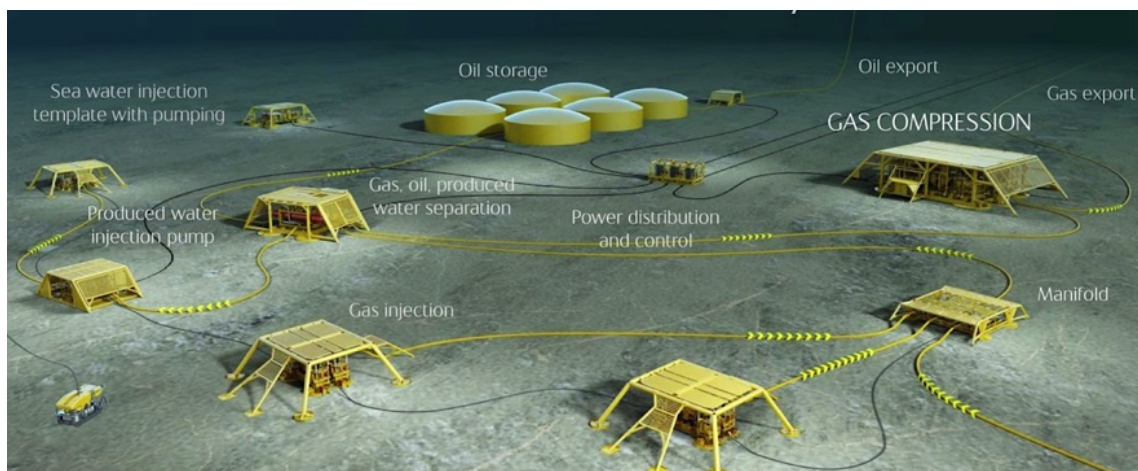


Figure 1.1: The subsea factory [45].

1.2 Multiphase flow

The phase content distribution can be described on a volumetric basis or a mass basis. The gas volume fraction is given as:

$$GVF = \frac{Q_g}{Q_g + Q_l} \quad (1.1)$$

Wet gas is typically defined as gas containing up to 5% liquid on a volume basis. Gas mass fraction is defined as:

$$GMF = \frac{\dot{m}_g}{\dot{m}_g + \dot{m}_l} \quad (1.2)$$

The density ratio is defined as the ratio between gas and liquid density:

$$\delta = \frac{\rho_g}{\rho_l} \quad (1.3)$$

Figure 1.2 shows the relationship between GMF and GVF for a typical wet gas hydrocarbon mixture (HC) at 50 and 80 bar in comparison to a water/air mixture at atmospheric conditions. Compressor tests that are conducted using an air/water mixture will have a GVF that is close to unity in all performance tests due to the large density difference. Evaluations performed by Grüner and Bakken [27] has showed that testing with air/water at low pressures gives the same performance trends as high-pressure hydrocarbon tests. It is recommended that comparison between different fluids and inlet conditions is based on the same GMF.

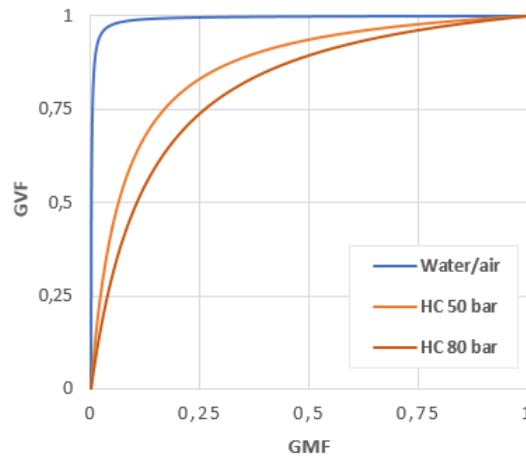


Figure 1.2: Relationship between GMF and GVF.

Other properties which are useful for describing multiphase flow are the Weber number and the Stokes number. The Weber number is a dimensionless number that relates to the inertia forces and surface tension forces in a two phase fluid. It predicts formation of liquid droplets or gas bubbles in multiphase flow.

$$We = \frac{\text{Inertia forces}}{\text{Surface tension forces}} = \frac{\rho l_C c^2}{\sigma} \quad (1.4)$$

The Stokes number characterizes the behaviour of droplets suspended in a fluid flow. It is defined as the ratio of the characteristic time of a droplet to the characteristic time of the flow. Droplets tend to follow fluid streamlines at Stokes number $\ll 1$. This implies that a mixture theory can be used instead of full multiphase approach [5].

$$St = \frac{\text{Droplet response time}}{\text{Fluid response time}} = \frac{\sigma c}{D_d} \quad (1.5)$$

where D_d is the droplet diameter. Multiphase flow is a complex phenomena that is difficult to predict and model. Single phase characteristics such as velocity profiles, boundary layers and turbulence are not easily adapted for describing multiphase flow. The flow is instead classified by flow regimes which depend on operating conditions, fluid properties and the geometry. Figure 1.3 shows a simple pattern map for horizontal flow, consisting of four flow regimes. The flow regimes depends on the superficial phase velocities:

$$u_{s,g} = \frac{Q_g}{A} \quad (1.6)$$

$$u_{s,l} = \frac{Q_l}{A} \quad (1.7)$$

where A is the total pipe cross sectional area.

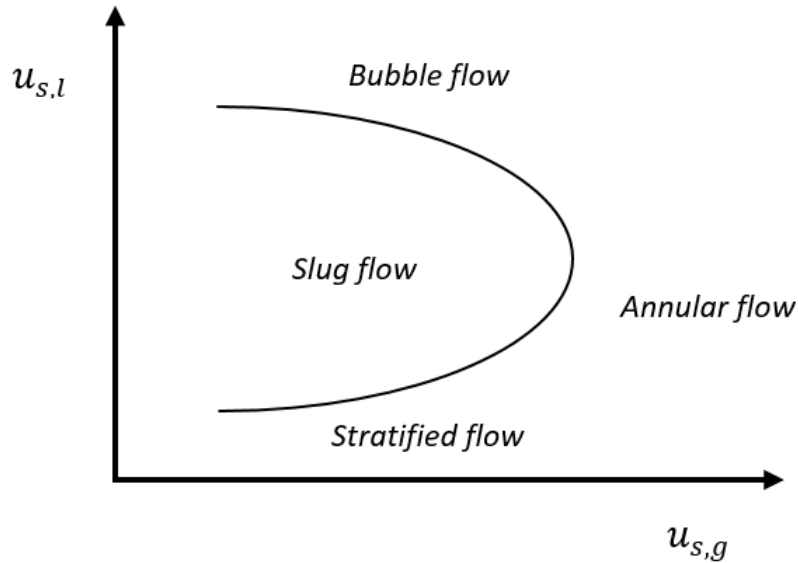


Figure 1.3: Regime map for multiphase flow

The four flow regimes are:

1. *Stratified flow* is found in the low flow region of the map. It is characterized by a single distinct horizontal phase interface. Common for pipelines with small density ratio where gravitational forces separate the phases.
2. *Annular flow* covers the high region of the map where the superficial velocity of gas is very high. A thin liquid film is present on the pipe wall, while the gas, with some liquid droplet entrainment, is flowing in the core of the pipe.

3. In *Slug flow*, the gas phase exist as large bubbles separated by liquid "slugs". Slug flow is formed from stratified flow initiated by a high velocity difference between the phases. A wave forms and grows due to the Kelvin-Helmholtz mechanism. Once the wave reaches the top of the pipe it forms a slug which pushes and accelerates the gas. The increased velocity of the gas then sweeps more liquid into the slug [4].

4. *Dispersed bubble flow* exist in liquid dominated systems. The gas is present in the higher region as entrained bubbles.

Flow pattern maps come in different variations. Other maps make further differentiations between flow patterns and introduce fluid properties such as density, viscosity and surface tension. Wet gas is dominated by a high velocity gas phase. The flow is therefore expected to be located within the annular flow region of the flow map during normal wet gas operation.

1.3 Previous work

Multiphase compression is a relatively new field of research. Prior to the emergence of wet gas compression as a viable alternative in subsea boosting applications, most of the research on wet gas is associated with axial compressors, in particular related to power augmentation by injecting water into the compressor. Such applications are aimed at increasing the output power in industrial gas turbines by reducing compressor power consumption. This is known as *wet compression*. Previous research in this field include Sanjeev [52] and Zachary et al. [67].

In 2003/2004 Statoil tested a single-stage centrifugal compressor operating on hydrocarbon mixtures with GVF between 1.00 and 0.97. Brenne et al. [11] reported a higher pressure ratio for wet gas, and explained it by the decrease in overall compressibility when introducing liquid to the mixture. Polytropic head decreased due to the higher density of the liquid. Polytropic efficiency was reduced and liquid film blockage inside the the compressor channels was considered to be a major factor for the increased losses.

A mass correction method was proposed by Hundseid et al. [30] in order to account for the density difference. In addition, a correction for polytropic head compressibility correction based on Wood's multiphase approach was developed.

Hundseid [28] also pin pointed seven effects of wet gas. These include increased fluid density, cooling due to evaporation, heat transfer between phases due to high liquid heat capacity, losses due to interaction between phases, reduction in speed of sound, liquid film formation in impeller and liquid leakage in seals and passages between compressor components.

Transient operation in compressors is traditionally associated with the left limit of the performance curve, where compressor instabilities leads to flow and pressure fluctuations. NTNUs wet gas compressor rig was constructed in 2006 and the left limit has been the focus of several experimental campaigns on this rig. This includes the work of Grüner [27] and Ferrara [20]. Exposing a compressor directly to the wellstream means that it may experience transients in the form of sudden variations

in GMF, especially during start-up and at low flow conditions. To the authors knowledge, this topic has not been covered in previous research.

The American Society of Mechanical Engineers (ASME) does not cover wet gas operation in their Performance Test Code on Compressors and Exhausters (PTC-10) [2]. Guidelines published by Gas Machinery Research Council (GMRC) in 2006 [12] recommended performance evaluation in wet gas conditions based on Brenne et. al's approach [11].

1.4 Project scope

The topic of this thesis is detection and analysis of compressor transients. The available test rig is equipped with dynamic pressure sensors mounted in the compressors diffuser, which are ideal for identifying transient aerodynamic behaviour. It was therefore considered to be appropriate for the author to focus on documenting detection techniques that employs vibration data, either as pressure fluctuations in the gas stream or as vibration measurements on the rotor.

The literature review covers the fundamentals of vibration, and documents how a spectrum analyzer can be used effectively to process the data. Performed tests are concentrated in the surge area of the compressors, and covers transients both in the form of flow and GMF variations. Due to limited test rig availability and a wide objective, it is decided to only include results obtained with one impeller configuration.

In order to give a correct interpretation of test data, a review of the flow dynamics of the centrifugal compressors is also needed, with particular focus on the characteristics of a compressor operating in the surge area. The goal is to identify the nature of flow instabilities in a wet gas compressor, as well as uncover eventual detection challenges that the presence of multiphase flow may inflict.

The thesis is constructed as a scientific report, with literature review and discussion followed by results and a final conclusion. The main content of each chapter is shown below:

- *Chapter 1* provides an introduction and introduce wet gas fundamentals.
- *Chapter 2* gives a thorough review of the centrifugal compressor flow dynamics and asses possible effects of multiphase flow.
- *Chapter 3* presents the fundamentals of vibration and documents the methods that exist for obtaining and processing vibration data.
- *Chapter 4* investigates compressor flow instabilities, both related to operation in proximity of the surge area and GMF fluctuations.
- *Chapter 5* presents the test rig and disusses the results obtained during the performed experimental campaign.
- *Chapter 6* concludes the report and includes recommendations for further work.

CENTRIFUGAL COMPRESSOR FLOW DYNAMICS

Even though the only wet gas compressor that has been in operation thus far was an axial flow machine, centrifugal compressors are dominant in gas processing. They are used extensively because of their smooth operation, large tolerance of process fluctuations and high reliability. Most of the research on the impact of wet gas is therefore focused on centrifugal compressors. The gas entering a centrifugal compressor is lead through three sections; the energy imparting impeller, which is mounted on a driven shaft; the diffuser, which decelerates the gas and increases the static pressure; and the volute, which collects the gas and delivers it to an outlet pipe. In multi-stage compressors the intermediate stages contains return bends that redirect the flow into the next stage instead of a volute. Figure 2.1 gives a side view of a centrifugal compressor as well as an indication of the static pressure and velocity through the impeller and the diffuser.

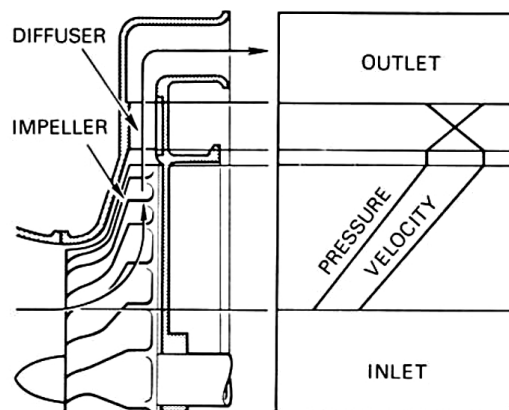


Figure 2.1: Pressure and velocity through a centrifugal compressor [9].

Flow study in centrifugal compressors is the most complicated in turbo machinery, mainly due to the unsymmetrical geometry of the impeller blades and volute, as well as the presence of secondary flow. The attention in this chapter will be spent on giving a review of the known flow dynamics in dry conditions while incorporating wet gas considerations along the way.

2.1 Viscous effects

Viscous effects are important to consider in centrifugal compressors, both because the geometry is characterized by long narrow channels and because it is vulnerable to flow separation due to the highly adverse pressure gradient that is present throughout the impeller and diffuser. This section gives an introduction to boundary layer theory and serves as a basis for discussions related to compressor flow dynamics and instabilities.

The Boundary Layer

Consider a viscous fluid of uniform velocity that approach a horizontal plate surface, as illustrated in Figure 2.2. The upper region of this flow field is unaffected by the incoming surface and have an uniform velocity field that is unaffected by viscosity. In most engineering problems, the force of attraction between fluid particles and solid particles (adhesive forces) are greater than the forces between the fluid particles (cohesive forces). Consequently, the flow will need to decelerate to zero at the fluid-solid interface. This is in fluid mechanics commonly referred to as the *no-slip condition*. Implicitly, a region of non-uniform flow needs to exist between the solid surface and the upper region. This region is known as the *boundary layer*, and is a region where flow can no longer be considered inviscid. The boundary layer is usually defined to include the area from the surface to the point y where:

$$u(y) = 0.99u_\infty \quad (2.1)$$

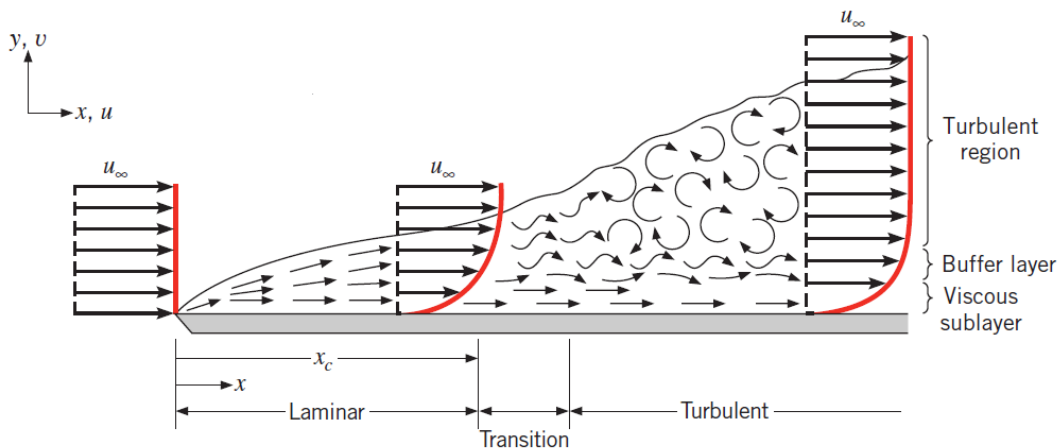


Figure 2.2: Viscous flow over a flat plate [7].

When the flow makes contact with the surface, the boundary layer takes shape as a retarded flow in the area between the plate surface and the inviscid outer flow. As the distance from the leading edge gets larger, a higher fraction of the fluid gets caught up by the retardation, and the thickness of the boundary layer grows.

Boundary layer thickness δ is therefore an increasing function of the distance from the leading edge x .

A fundamental principle in fluid mechanics is the distinction between laminar and turbulent flow. Laminar flow is characterized by orderly fluid motion where almost all particles move parallel to the stream lines. Turbulent flow is more chaotic and contains fluid swirls known as *eddies* that results in lateral mixing. The dimensionless Reynolds Number is used to predict the flow pattern, and represents the ratio of inertial forces to viscous forces. For flow over a flat plate this is:

$$Re = \frac{ux}{\nu} \quad (2.2)$$

Initially, the flow will always be laminar, but a transition to turbulent flow may occur at a critical length x_{crit} . The boundary layer for turbulent flow is divided into two separate sublayers. The *laminar sublayer* is the layer close to the no-slip boundary. As the name indicates, it behaves similarly to the boundary layer in laminar flow, and is highly viscosity dependent. In the upper region of the boundary layer, there is a *turbulent layer*, characterized by fluctuating motion. It is sometimes referred to as the frictional layer due to the losses associated with the chaotic motion. By inspection of Figure 2.2 it can be seen that a buffer layer is situated between the laminar layer and the turbulent layer. This is an intermediate region in which turbulent effects are becoming significant, but the flow is still dominated by viscous effects [7].

Flow separation

Flow separation can be visualized by considering flow around a circular cylinder. Figure 2.4 illustrates the flow pattern and the pressure distribution at various points around a cylinder.

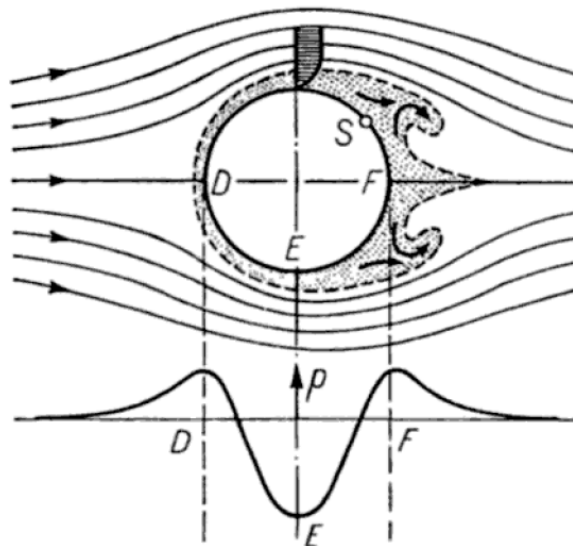


Figure 2.3: Boundary layer flow separation around a circular cylinder [54].

A particle that moves from point D to E will be deflected by the cylinder's surface and forced to accelerate, thus reducing the pressure. The same particle will from

point E to F experience a reversed effect where kinetic energy is transferred back to pressure. This is unproblematic for particles located in the outer flow because they can freely accelerate and decelerate without viscous interference. On the other hand, a particle that is situated inside the boundary layer will be slowed down by the viscous forces. This results in the particle losing its kinetic energy, and leaves it incapable of moving to point F. The particle instead detaches from the flow and moves in the pattern of an eddy or vortice [54].

As mentioned in the previous section, boundary layers can either be laminar or turbulent. This is of relevance because the flow pattern in the boundary layer is known to affect the separation point S. A turbulent flow will delay separation because of the high degree of integration between the fluid particles, allowing kinetic energy to be transferred to the low energy laminar sub-layer. This means that turbulent flow is more resistant to flow separation, and perhaps somewhat counterintuitively, the orderly laminar flow is more likely to cause flow instabilities.

Figure 2.4 illustrates the evolution of the boundary layer flowing over a curved surface with an adverse pressure gradient. A continuous retardation of flow brings the wall shear stress at the point S on the wall to zero. Downstream of this point the shear stress becomes negative and the flow reverses.

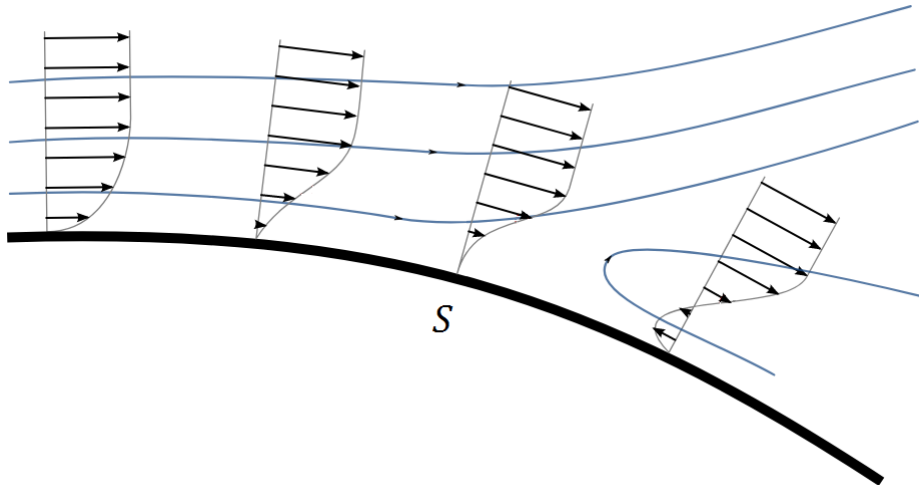


Figure 2.4: Boundary layer evolution across a curved surface.

The phenomenon can also be shown by referring to the streamwise momentum equation inside the boundary layer:

$$u \frac{\partial u}{\partial s} = -\frac{1}{\rho} \frac{dp}{ds} + \nu \frac{\partial^2 u}{\partial y^2} \quad (2.3)$$

where s is the streamwise coordinate. An adverse pressure gradient $dp/ds > 0$, causes the velocity u to decrease and go to zero if it is sufficiently strong.

The impeller and the diffuser in a centrifugal compressor are both components that are designed to have a strong adverse pressure gradient. Knowledge about the nature of flow separation is therefore vital, especially when analyzing performance

in the low flow, high pressure region of the compressor map. Flow separation will be closer related to compressor instabilities in Chapter 4.

2.2 Impeller

The impeller can be divided into two sections, termed the *inducer* and the *centrifugal section*. The inducer is responsible for efficiently guiding the flow into the impeller. Its design is critical for the operating range of the impeller. The centrifugal section changes the flow direction from axial to radial and essentially governs the momentum exchange. Most modern impeller have centrifugal vanes that are manufactured with a backsweep in order to increase the operating range. The impeller is a complex component that contains 3 dimensional curvature, and is highly dependent on viscous effects. Direct solutions of the Navier-Stokes equations through computational fluid dynamics (CFD) is needed to get a complete analysis of flow field. This is not the focus of this thesis, but instead a simplified flow analysis is presented. The flow analysis for both the impeller, diffuser and volute follows the method of Cumpsty [14], although adapted in order to illustrate the relevant points.

2.2.1 Flow analysis

Since the impeller is rotating, it is convenient to use a cylindrical coordinate system moving with the impeller. Considering an impeller channel with radial blades where the rotational rate of change is assumed to be zero, the momentum equation for compressible, inviscid flow can in vector form be written as:

$$m\vec{a}_{rel} = \vec{F} - m(2\vec{\omega} \times \vec{W} + \vec{\omega} \times (\vec{\omega} \times \vec{r})) \quad (2.4)$$

where \vec{a}_{rel} is the relative acceleration of the fluid, \vec{F} is the pressure force and the two last terms represent Coriolis force and centrifugal force, respectively. Calculating the cross products gives:

$$\vec{\omega} = [0 \quad 0 \quad -\omega], \quad \vec{W} = [W \quad 0 \quad 0], \quad \vec{r} = [r \quad 0 \quad 0]$$

$$\vec{\omega} \times \vec{W} = [0 \quad -\omega W \quad 0] \quad (2.5)$$

$$\vec{\omega} \times \vec{r} = [0 \quad -\omega r \quad 0] \quad (2.6)$$

$$\vec{\omega} \times (\vec{\omega} \times \vec{r}) = [-\omega^2 r \quad 0 \quad 0] \quad (2.7)$$

while the force from the pressure gradient is given by:

$$\vec{F} = -\frac{1}{\rho} \vec{\nabla} p m - \frac{1}{\rho} \left(\frac{\partial \vec{p}}{\partial r} + \frac{1}{r} \frac{\partial \vec{p}}{\partial \theta} m \right) \quad (2.8)$$

Inserting the calculated cross products and the equation for pressure force into the momentum equation, gives expressions for the force balance in the radial direction r and the tangential direction θ :

$$m\vec{a}_r = -\frac{1}{\rho} \left(\frac{\partial \vec{p}}{\partial r} \right) m + \omega^2 r m \quad (2.9)$$

$$m\vec{a}_\theta = -\frac{1}{\rho} \left(\frac{1}{r} \frac{\partial \vec{p}}{\partial \theta} \right) m + 2\omega W \sin(\gamma) m \quad (2.10)$$

Notice that a component of vorticity $2\omega \cos \gamma$ has been introduced in the θ -direction. As illustrated in Figure 2.5b, γ refers to the inclination angle of the blade-to-blade surface of the axis of rotation. In order to account for the backsweep that most impellers are designed with, a centrifugal acceleration component $\frac{mW^2}{R}$ working perpendicular to the relative velocity vector W would need to be added. R is here the impellers local radius of curvature, into the plane in Figure 2.5a.

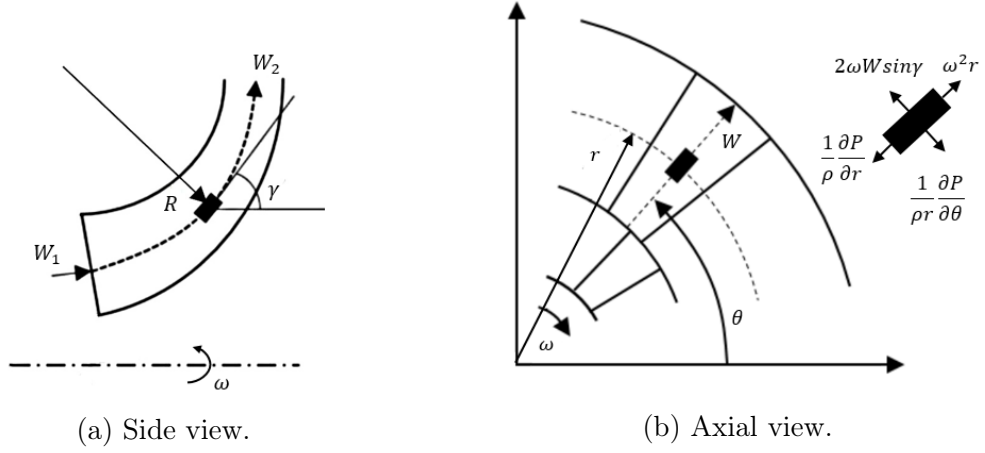


Figure 2.5: Impeller geometry and force balance [55].

An estimation of the pressure field in the impeller channel is obtained by assuming the radial and tangential acceleration vectors to be negligible and rearranging Equation 2.9 and Equation 2.12.

$$\frac{\partial \vec{p}}{\partial r} = \omega^2 r \rho \quad (2.11)$$

$$\frac{\partial \vec{p}}{\partial \theta} = 2\omega W \sin(\gamma) \rho \quad (2.12)$$

It is therefore clear by equation 2.11 that pressure increases in the radial direction and the head produced by the impeller is proportional to density. Also shown, by equation 2.12 is that there is a pressure rise occurring from the trailing side of one impeller blade to the leading edge of the next one.

One last consideration becomes apparent when taking the side view of the impeller channel (Figure 2.5a). The curvature of the impeller channel gives rise to another centrifugal force $\frac{mW^2}{R}$ acting normal to the local flow direction. Since the radius is greater on the hub-side, there also needs to exist a positive pressure gradient in the shroud to hub direction.

Secondary flow

The pressure gradients across the impeller channels give rise to what is known as secondary flows. In the general case, secondary flows can be described as minor flows superimposed on the primary flow. Cumpsty [14] states that secondary flows are

generated when a primary flow with non-uniform stagnation pressure is subjected to acceleration perpendicular to the primary streamline direction. In the case of a centrifugal compressor these arise both due to the curvature of the impeller channel and due to the Coriolis acceleration. The stagnation pressure is defined as:

$$p_0 = p + \frac{\rho C^2}{2} \quad (2.13)$$

In radial machines it is convenient to redefine this equation by expressing the absolute velocity C as the vector sum of the relative velocity W and the rotational velocity U , and using the relation $\omega r = U$. Equation 2.13 is then rewritten as:

$$p_0 = p + \frac{\rho W^2}{2} - \frac{\rho \omega^2 r^2}{2} \quad (2.14)$$

The uneven pressure distribution in the impeller channel therefore establish low relative stagnation pressure regions at both the shroud side of the impeller and at the suction side of the blades.

Equation 2.15 defines the dimensionless Rossby number, often used in relation to secondary flow. If this number is large, the effect of curvature will dominate over the rotation.

$$R_0 = \frac{W}{\omega R} \quad (2.15)$$

When a region of low p_0 is formed, it can be used to predict where it will be drawn. If the Rossby number is large (indicating large curvature), the fluid will be drawn towards the shroud, whereas it will be drawn towards the suction surface if the Rossby number is small, i.e. if rotation is dominant. These secondary flows give rise to what is known as the jet-wake pattern at the impeller outlet, where a low energy region is established as a wake at the shroud/suction side. Figure 2.6 shows velocity measurements performed by Eckard in 1976. The pattern is clearly visible in the fifth cross-section by the outlet, where the wake is measured to have a significantly lower velocity than the jet.

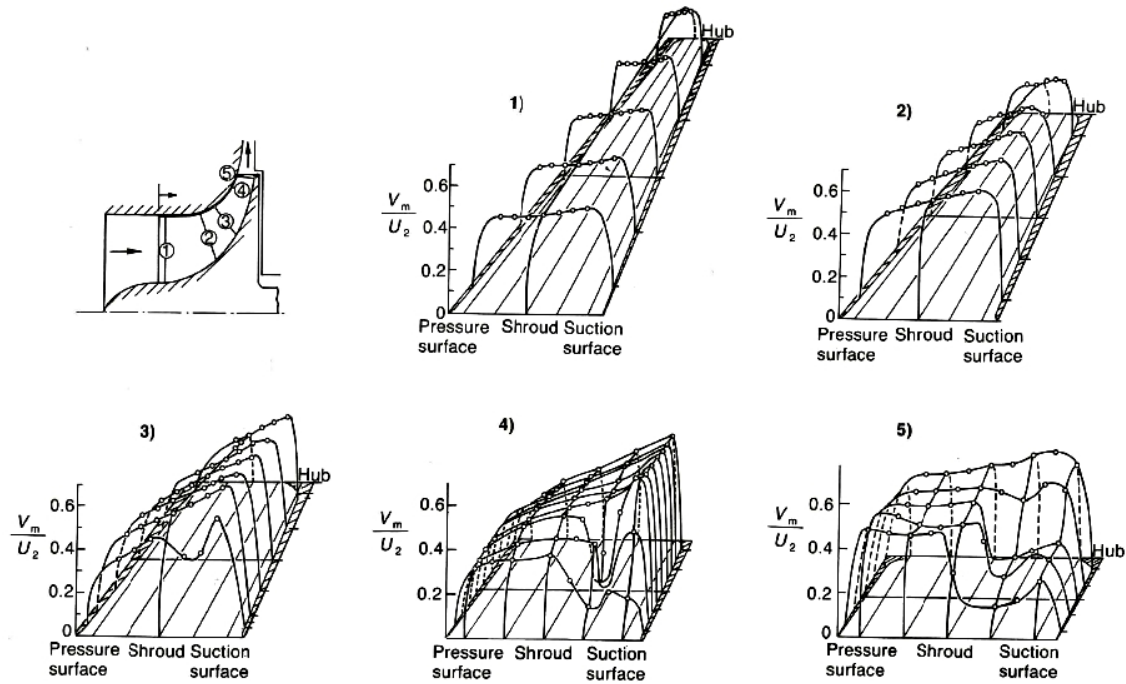


Figure 2.6: Velocity measurements by Eckardt in a radial impeller [18].

Boundary layer stability

Both rotation and curved surfaces are known to affect the stability of flow in a boundary layer. This can be understood heuristically by considering a fluid particle in the boundary layers at the suction surface of a radial impeller (Figure 2.7). There is a pressure gradient normal to the blade surface balancing the Coriolis acceleration expressed by its relative velocity $2\omega W \sin\gamma$. Imagine now that the particle is perturbed and displaced slightly away from the wall while flowing at the same velocity. The particle is now in a region where the particles at equilibrium has a slightly higher velocity $W + W'$, meaning that the local pressure gradient must be large enough to balance the Coriolis acceleration $2\omega(W + W')\sin\gamma$. The particle experience an acceleration $2\omega W'$ from the pressure gradient and is therefore pushed back to its initial position. The motion within the boundary layer is therefore stable.

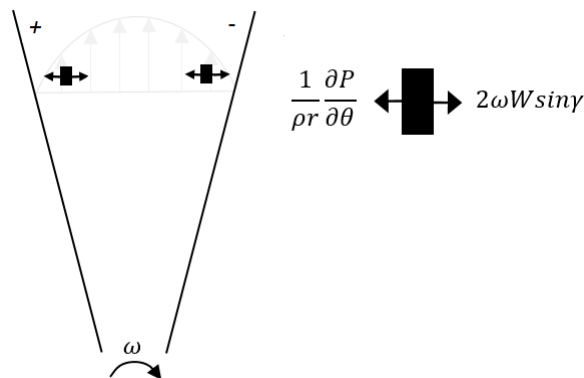


Figure 2.7: Boundary layer instability.

Now, consider a fluid particle in the boundary layers at the pressure surface. When subjected to a similar perturbation and displaced into a region of higher velocity, the pressure gradient still works in the same direction, i.e. away from the wall. This means that instead of being forced back to the wall, the particle moves further away from it. The particle is therefore free to move away from the boundary layer and the boundary layer is in this case unstable.

From Section 2.1 it is known that it is not favorable for a viscous flow to be stable, because it is the shear stresses of unstable, turbulent flow that delays flow separation. For the corresponding case of flow between the hub and shroud side of the impeller the argument is the same, but the premise contains the centripetal acceleration W^2/R instead of the Coriolis acceleration. This means that the low pressure shroud side can be identified as the side where turbulence is delayed.

In conclusion, the suction and shroud sides are shown to be sides where turbulence is delayed and flow separation may occur. According to Cumpsty [14], most experiences suggest that the attention should be at the surface of the strongly curved shroud.

Slip

In an idealized flow analysis the flow exiting the impeller would uniformly flow in the same way as the blades are pointing. This is not the case in reality. As soon as the flow exits the rotating frame, the distinct pressure and suction side of the impeller blades are equalized. A component of relative velocity in the opposite direction to the rotation is therefore created, known as the *slip velocity*. Figure 2.8 illustrates the slip velocity, as well as its influence on the ideal velocity diagram.

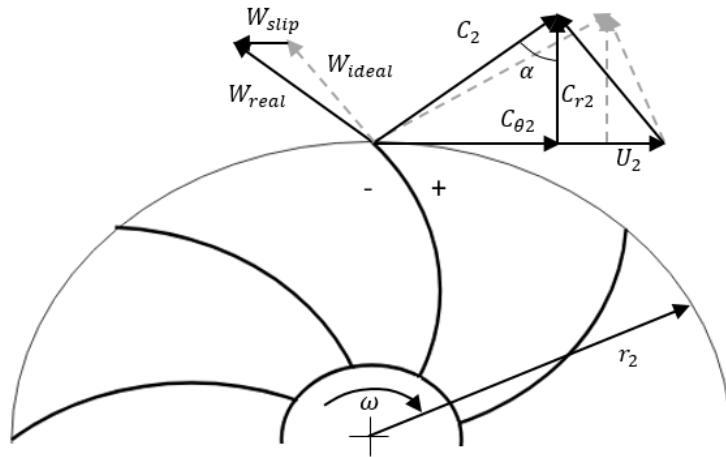


Figure 2.8: Slip in a backswept impeller.

The quantification of the slip velocity is based on empirical relations between the velocity components, as well as the number and geometry of the blades. Several models have been derived, Boyce [9] includes a comparison of six models in his handbook on Gas Turbines.

Leakage

Leakage around the impeller is inevitable since it rotates within a casing. In order to reduce the leakage, it is common to employ simple labyrinth seals. They are made up of a number of fins that form a series of annular orifices, acting as a restriction for the fluid. The volumetric leakage across this seal is a function of the pressure difference across the impeller and the design of the seal, mainly the number of fins [3]. Of most interest for the compressor flow regime is the gap between the impellers inlet and outlet. The leakage here may become significant and affect the flow regime at low flow/high pressure conditions.

The component configuration by the impeller inlet will also influence the effect that the leakage has on the inlet flow regime. For narrow impellers, Lüdtke [39] recommends a configuration where the leakage flow is guided in the direction of the main flow, providing an almost tangential blend-in. On the other hand, orthogonal leakage re-entry is discouraged as it disturbs the inlet flow and may even trigger vortex formation. The different design are shown in Figure 2.9.

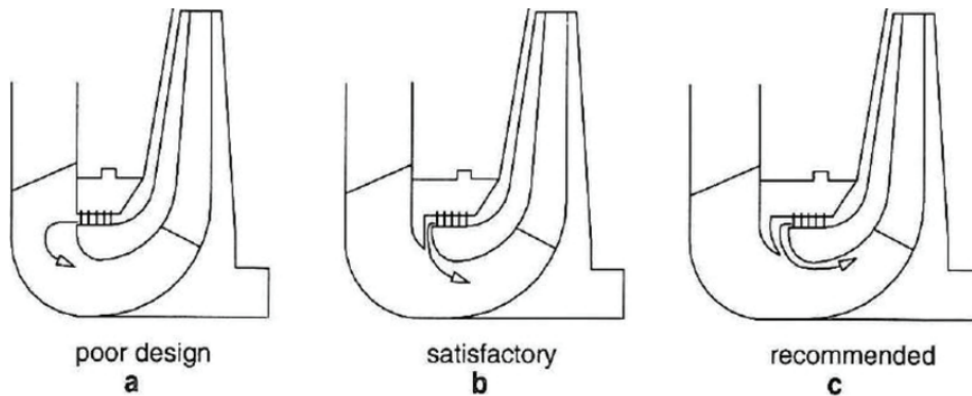


Figure 2.9: Leakage design recommendations [39].

2.2.2 Multiphase effects

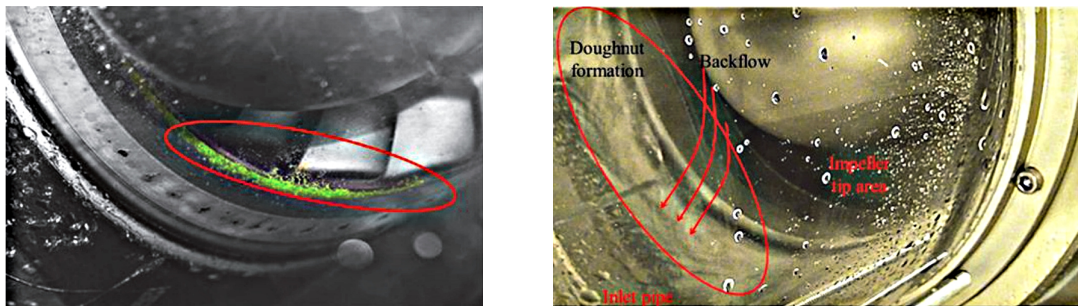
Multiphase flow in the impeller channels is not covered in compressor theory, but a number of predictions can be made by inspecting the forces acting on the fluid elements. The four forces that have been shown to act in the inviscid center flow of an impeller channel are the coriolis force $2\omega W \sin(\gamma)m$, the centrifugal force from impeller rotation $\omega^2 rm$, the centrifugal force from blade to blade curvature $\frac{mW^2}{R}$ and the centrifugal force from impeller inlet to outlet curvature $\frac{mW^2}{R}$. All of which are balanced by the static pressure force. By expressing mass as a product of volume and density, it is seen that the forces increase with increasing density. In a two phase mixture, especially at high Stokes number and low density ratio, the impeller channel is therefore a zone where flow segregation is expected.

More specifically, the liquid phase will be forced towards the hub and pressure side of the impeller channel and the gas phase will flow along the shroud and suction side. The formation of a liquid film was briefly mentioned in the introduction, and is one important reason for the necessity of a full multiphase approach when

evaluating the flow dynamics in a wet gas compressor. Introduction of a liquid layer will change the velocity profile across the impeller channel since a new interaction region is formed between the liquid and gas phase. In the next instance this will also alter the flow structure at the impeller exit. Characterized by high momentum, the liquid film will be less affected by the pressure gradient at the exit of the impeller. Hence, a reduction in slip is likely.

The viscosity ratio between the gas and liquid depends on the composition. For an air/water mixture the kinematic viscosity of the gas is higher, which suggest that liquid dominated regions will be highly turbulent and resistant to flow separation. The introduction of a liquid phase therefore makes the flow at the hub/pressure side of the impeller even less likely to separate.

In order to maintain a stable flow pattern at the impeller inlet, the fluid particles that exits into the inlet flow through the labyrinth seal depends on the drag forces of the main flow being able to carry them into the impeller. This becomes increasingly difficult as the density of the high density fluid particles increase. Multiphase flow thus creates a risk zone for stalling and liquid blockage near the impeller eye. This phenomenon is well documented at the NTNU test rig. Figure 2.10 refers to Ferraras work and shows how the liquid is affected by the impellers motion and forms a liquid "doughnut" in the inlet pipe with a substantial tangential velocity component.



(a) Leakage by the inducer tip.

(b) Doughnut formation in the inlet pipe.

Figure 2.10: Liquid accumulation by compressor inlet. Fluorescent liquid was injected into the labyrinth seal to confirm the source [20].

2.3 Vaneless diffuser

The vaneless diffuser is a very simple component, only consisting of an annular channel surrounding the impeller. However, the aerodynamic behaviour is complicated by the non-uniformity of the the jet-wake flow entering, and by the viscous effect that the long flow path provide. The diffuser also needs to cope with flow variations in the axial and circumferential direction.

2.3.1 Flow analysis

The axial width of a diffuser is usually constant, i.e straight walled, although it can be designed with a width that vary in the radial direction, either to increase pressure recovery or to stabilize the flow. Equations 2.16 to 2.18 give the cylindrical

continuity- and momentum equations for inviscid flow in a diffuser with constant width and uniform inlet velocity.

$$\frac{1}{r} \frac{\partial(\rho r C_r)}{\partial r} = 0 \quad (2.16)$$

$$C_r \frac{\partial C_r}{\partial r} - \frac{C_\theta^2}{r} = -\frac{1}{\rho} \frac{\partial p}{\partial r} \quad (2.17)$$

$$C_r \frac{\partial C_\theta}{\partial r} + \frac{C_r C_\theta}{r} = 0 \quad (2.18)$$

Integrating equation 2.16 and 2.18 from diffuser to a point (r, θ) gives:

$$C_r r = C_{r2} r_2 \quad (2.19)$$

$$C_\theta r = C_{\theta2} r_2 \quad (2.20)$$

By inserting these two equations into the radial momentum equation (Equation 2.17), an expression for the pressure increase over the diffuser is obtained, showing that the pressure gradient is proportional to the radius ratio squared:

$$\frac{p - p_2}{\frac{1}{2} C_2^2} = \left(1 - \left(\frac{r_2}{r} \right)^2 \right) \quad (2.21)$$

In order to describe the diffuser flow path, it is useful to consider the streamline equation, which for incompressible, inviscid flow is given as:

$$\frac{1}{r} \frac{\partial r}{\partial \theta} = \frac{C_r}{C_\theta} \quad (2.22)$$

From Equation 2.19 and Equation 2.20 it is known that $\frac{C_r}{C_{\theta2}} = \frac{C_{r2}}{C_{\theta2}}$. The streamline equation can therefore be integrated, yielding an expression for the diffuser flow path:

$$\ln \frac{r}{r_2} = \frac{(\theta - \theta_2)}{\tan \alpha} \quad (2.23)$$

Here α is designated to the logarithmic spiral angle and is defined as $\alpha = \tan^{-1} \left(\frac{C_{\theta2}}{C_{r2}} \right)$. This means that the flow in diffuser can be approximated as logarithmic spiral streamlines, as Figure 2.11 shows. Assuming the flow to be inviscid and incompressible leads to some inaccuracies that should be addressed. Introducing compressibility to the fluid will lead to an increased density in the outer region of the diffuser, demanding a decrease in radial velocity in order to satisfy mass conservation. The diffuser flow is also highly dependent on the viscous effects near the boundary layers of the hub and shroud walls, meaning that a non-uniform velocity profile across the diffuser width is likely.

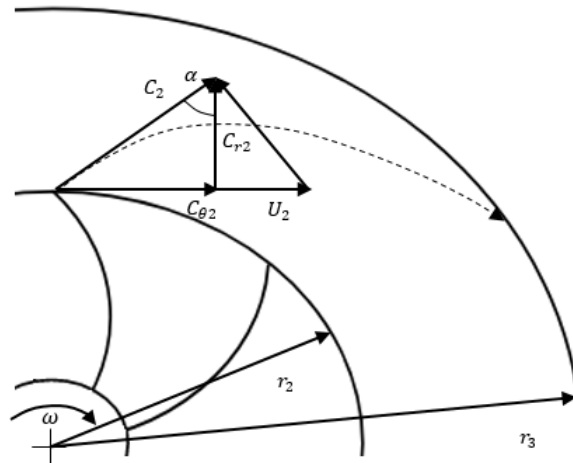


Figure 2.11: Diffuser flow.

The wide surge margin of backswept impellers also becomes apparent when studying the velocity diagram at the diffuser inlet. The associated acceleration component $\frac{W^2}{R}$ increase the absolute velocity C at the impeller outlet, which in turn reduce the diffuser flow path.

One last consideration is the highly separated jet-wake flow exiting the impeller. Knowing that that the jet velocity is higher than the wake velocity it can be seen that the flow at the diffuser inlet will be highly non-uniform, characterized by wake streamlines with high flow angle α . According to Cumpsty [14], most researches shows that this unsteadiness has little influence on the diffuser performance because the flow quickly merge into one uniform flow.

2.3.2 Multiphase effects

As established in section 2.2, a heavy liquid will tend to separate from the gas phase in the impeller and accumulate in the hub/pressure side. When the liquid enters the open diffuser channel the liquid film will take a shorter flow path owing to its high density. As long as the liquid film is continuous, it will also guide the gas phase towards a shorter flow path.

The segregated flow regime in the impeller can be described as an artificial flow regime since it is a consequence of the centrifugal forces. This force diminishes as the film exits into the diffuser. The Weber number suggest that the dispersion of the film will be more rapid if the inertia is high. However, the increased logarithmic flow path at low flow complicates the picture since it leads to phases with flow paths that crosses each other to a larger degree, thus creating larger impact forces between the particles that contribute to break up of the film. Skjefstad [55] investigated the flow regime in the diffuser at 90 % GMF and observed visible water jets that dispersed after a certain radial distance, thus establishing a region of segregated flow and a region of mixed flow. It was also found that this occurred nearer the impeller exit at low flow conditions.

Brenne [10] performed an experimental investigation of a straight walled diffuser subjected to air-water flow. It was found that the diffuser performance was reduced

with increased liquid mass flow rate, due to velocity profile distortion. Clustered droplets, with high inertia, travelled along the centerline, and were only slightly decelerated by the surrounding gas. The liquid was found to accumulate in low energy regions and initiate premature separation. Brenne therefore suggested for wet gas compressors to incorporate a "slim" diffuser design that was longer in the radial direction, but still had a smaller area ratio in order to stabilize the flow.

2.4 Volute

The volute is the compressor component responsible of collecting the gas and deliver it to the discharge pipe. Figure 2.12 shows the geometry of a symmetrical volute surrounding a compressor with backswept impeller blades and a vaneless diffuser. Volutes are generally designed to keep the circumferential velocity constant, meaning that they can be assumed to have no effect on the compressor performance. Perhaps for this reason, it is often neglected in compressor research and flow analysis. From the previous section it is known that the diffuser changes its flow pattern when operating at off-design conditions, and it is therefore undeniable that this will have downstream effects in the volute.

2.4.1 Flow analysis

The volute has a large cross sectional area and relatively low flow velocity. For the purpose of flow analysis, it is therefore assumed to have no frictional losses. With uniform static pressure it then follows from conservation of momentum:

$$r_3 C_{\theta 3} = r C_{\theta} \quad (2.24)$$

This means that for any volute shape, the circumferential velocity of the volute is entirely fixed by the local streamline radius. In particular, it is useful to refer to the mean radius of the volute r_m , which follows the center line of the volute cross section area:

$$r_3 C_{\theta 3} = r_m C_{\theta m} \quad (2.25)$$

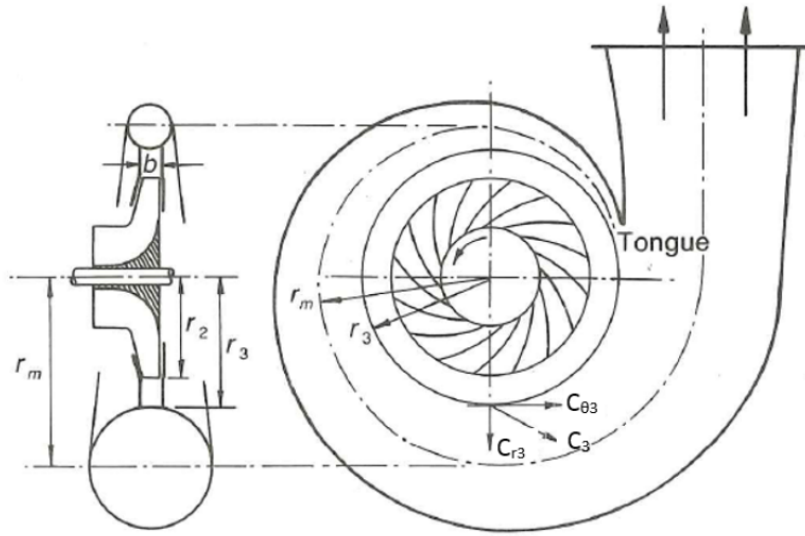


Figure 2.12: Symmetrical volute geometry [14].

The mass flow entering the volute control volume depends on the radial velocity C_{r3} , while the mass flow exiting is dictated by the tangential component $C_{\theta m}$. For a small arc around the circumference, the conservation of mass along a streamline s can be written as:

$$\frac{d}{ds}(\rho_m C_{\theta m} A) ds = \rho_3 C_{r3} b r_3 d\theta \quad (2.26)$$

where b is the axial width of the diffuser and A is the cross-sectional area of the volute. Here ρ_m and $C_{\theta m}$ are taken to give a reasonable average for the whole cross section.

Introducing Equation 2.25 into Equation 2.26, using the relation $ds = r_m d\theta$ and rearranging gives an expression for the geometric quantity that characterizes the volute, the ratio A/r_m

$$\frac{d}{ds} \left(\frac{A}{r_m} \right) = \frac{\rho_3 C_{r3} b}{\rho_m C_{\theta 3} r_m} \quad (2.27)$$

The important thing to notice here is that once a volute design is specified, i.e. a A/r_m ratio, uniform circumferential flow can only be achieved for one particular value of the ratio $V_{r3}/V_{\theta 3}$. This means that for each speed curve along the compressor map there will only be one point where the desired uniform flow is achieved.

At mass flows higher than this point fluid will enter the volute with large radial- and small tangential velocity components. The consequence of this is a large cross-sectional swirl because of the large radial component. In addition, the tangential velocity is too small to transport the fluid through the volute, and is forced to accelerate from volute tongue to volute outlet. The static pressure is therefore discontinuous along the volute - decreasing along the circumference and rising at the volute tongue.

At low mass flows the opposite is true. Small radial and large tangential velocity components lead to less swirl and a circumferential static pressure rise.

These effects were documented experimentally by Braenbussche and Hande in 1990 [61]. The latter effect is of concern for the stability of the compressor since an

adverse pressure gradient can lead to flow separation in the boundary layers. Even though compressor stall normally is associated with the impeller and diffuser, as will be discussed in Chapter 4, this means that the volute tongue can also a critical point for instability occurrence.

2.4.2 Multiphase effects

Introducing a variable amount of liquid to the compressor, means that the compressor has a new dimension of operating points. Since the volute is designed for a specific operating point it is apparent that this will affect the volutes performance. The incoming flow will have a larger radial component due to the reduced flow path in the diffuser, leading to swirl and acceleration through the volute. On the other hand, the flow will also have a decelerating component because of an increased density, both due to the increased mass flow rate, and due to the cooling effect of the liquid. These factors depends on operating point and fluid properties. A quantification of these factors is therefore necessary in order to predict the performance of the volute.

2.5 Summary

A review of the compressor flow dynamics is given. Potential effect of multiphase flow on the compressor is identified on the basis of single phase flow analysis. Multiphase effects include:

- Formation of liquid film in hub/pressure side of impeller due to centrifugal and coriolis forces. Increase head produced by impeller due to increased mass. Liquid will tend to accumulate by the impeller inlet at low flow conditions.
- Breakup of liquid film in diffuser due to free flow with high inertia, i.e. high Weber number. Degraded diffuser performance has been observed by previous researchers.
- Counteracting factors affecting volute performance with magnitude depending on operating point and fluid composition.

VIBRATION AND SPECTRUM ANALYSIS

Focus is now shifted away from the fluid mechanics. This chapter documents the fundamentals of vibration, and shows how the frequency spectrum analysis can be used to detect vibration phenomena in the compressor, both periodic and transient. In order to give correct diagnostication when analyzing the compressor, a solid understanding of the nature of vibration is needed.

3.1 One dimensional vibration

Fortunately, many vibration related problems can be adequately described by referring to a one degree of freedom system. The theory presented in this section is well documented in textbooks on this subject, e.g. Timoshenko et al. [60].

3.1.1 Free vibration

The simplest version of a vibrating system is an undamped spring-mass system, illustrated in figure 3.1a. The Equation of motion for this system is given in Equation 3.1, and the general solution is defined by Equation 3.2. If this system is moved from its equilibrium position, the vibration continues forever at the *harmonic frequency*, since dampening and external forces are absent. The harmonic frequency is defined by Equation 3.3.

$$m\ddot{x} + kx = 0 \tag{3.1}$$

$$x = X \sin(\omega_n t + \Phi) \tag{3.2}$$

$$\omega_n^2 = k/m \tag{3.3}$$

where:

m = Mass

\ddot{x} = Acceleration

k = Spring coefficient

x = Position/amplitude

X = Maximum position/amplitude

ω_n = Natural frequency

t = Time

Φ = Phase angle

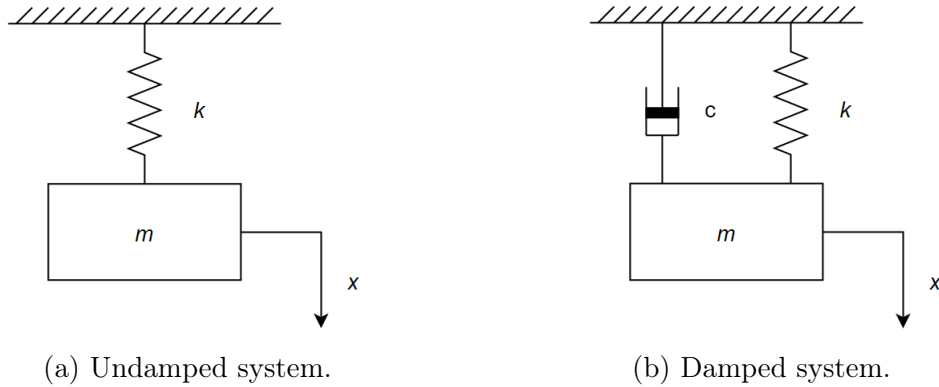


Figure 3.1: Spring-mass system.

In order to make the system more realistic, the system is modified by adding a viscous damping element, as depicted in figure 3.1b. The Equation of motion for this system is given by Equation 3.4, and Equation 3.5 defines the critical damping. If $c < C_{cr}$ the system is underdamped, meaning the system will experience an oscillating decay if disturbed; if $c > C_{cr}$ the system is overdamped and will come to rest without oscillating if disturbed; and if $c = C_{cr}$ the system is critically damped and returns to equilibrium as quickly as possible without oscillating. Figure 3.2 gives the characteristic movement in each of these cases.

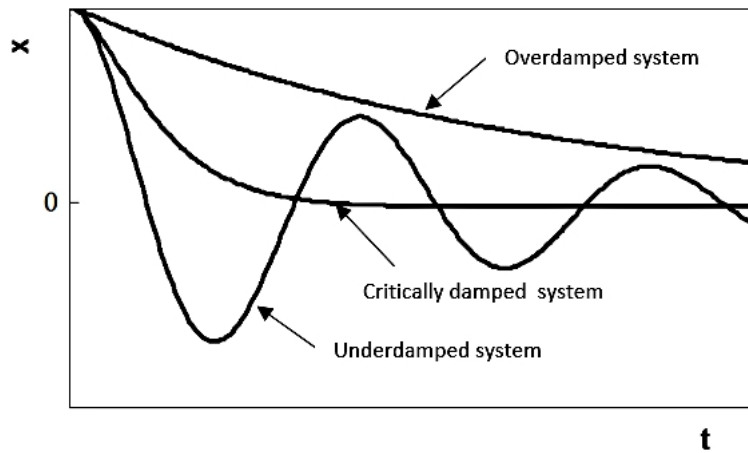


Figure 3.2: Damping of a spring-mass system.

Investigating only the case where damping is less than critical, the solution given by Equation 3.6 can be generated. This system has a decaying component $e^{-\mu t}$ where $\mu = \frac{c}{2m}$, and a harmonic component $\cos(pt + \Phi)$ with a natural frequency pt , where $p = \sqrt{\omega_n^2 - \mu^2}$. The rate at which the vibration of the system will return to zero is determined by the coefficient μ in the decaying component. Over one period T , this

coefficient is defined by Equation 3.7 where δ is known as the logarithmic decrement.

$$m\ddot{x} + c\dot{x} + kx = 0 \quad (3.4)$$

$$C_{cr} = 2\sqrt{km} \quad (3.5)$$

$$x = Xe^{-\mu t} \cos(pt + \Phi) \quad (3.6)$$

$$\delta = \mu T \quad (3.7)$$

where, in addition to earlier definitions:

c = Damping coefficient

\dot{x} = Velocity

C_{cr} = Critical damping

This means that as long as the system is free, damped or undamped, it will only vibrate at its natural frequency. The amplitude is defined by the motion at the natural frequency, and if damping is present, the rate of decay is defined by the logarithmic decrement.

3.1.2 Forced Vibration

The external forces acting on a compressor rotor can be characterized as either periodic or non-periodic (arbitrary). Harmonic forces, which is a special form of periodic force, is introduced first.

Harmonic External Forces

Harmonic forces are steady-state by nature and are given their name because they can be represented by a single sine wave as in the form of Equation 3.8. For a single degree of freedom system, it results in motion described by Equation 3.10, and the general solution of this equation is given in Equation 3.11. For a given relative force level $D = F/k$, the amplitude depends on both the ratio between the frequency of the forcing function to the system natural frequency $\tau = \omega/\omega_n$, as well as the amount of damping in the system $\rho = \frac{c}{2m\omega_n}$. As shown in Equation 3.11, the frequency of the vibration is at the same frequency as the forcing function, not the natural frequency. If the system is underdamped at the same time as the forcing frequency approach the natural frequency, the force will approach infinity. This is the well known phenomenon that is *resonance*.

$$s(t) = F \cos(\omega t) \quad (3.8)$$

$$m\ddot{x} + c\dot{x} + kx = F \cos(\omega t) \quad (3.9)$$

$$x = P \cos(\omega t - \Phi) \quad (3.10)$$

$$P = \frac{D}{[(1 - \tau^2)^2 + 4(\rho\tau)^2]^{1/2}} \quad (3.11)$$

where, in addition to earlier definitions:

$s(t)$ = Harmonic forcing function

ω = Frequency of forcing function
 F = Maximum of forcing function
 P = Maximum of response amplitude

By inspection of Equation 3.10 it can be seen that the response of a system subjected to a harmonic forcing function is harmonic motion at the same frequency as the force, with maximum amplitude occurring if the system is in resonance.

Periodic External Forces

The term periodic force is used if the signal is not a clean sine wave, but does repeat itself over a time period at a frequency ω . Any periodic signal can be expanded in a Fourier series, enabling the force to be described as in Equation 3.12. It is this capability which allows a Fourier transform to transform a vibration or pressure signal from the time domain to the frequency domain. This transformation is further described in Section 3.3.1.

When a force in the form of Equation 3.12 is exerted onto the mass in the damped spring-mass system, its response is given by Equation 3.13. This implies that the vibration occurs at the frequency of the forcing function and its multiples. The multiples are often referred to as *harmonics* - and is not to be mistaken with the harmonic forcing function explained above. Equation 3.14 gives the maximum amplitude. Here it can be noted that the amplitude is maximized when the systems natural frequency is equal to the frequency of the base forcing function or any of its harmonics.

$$s(t) = \sum_1^{\infty} F_n \cos(n\omega t + \theta_n) \quad (3.12)$$

$$x = \sum_1^{\infty} P_n \cos(n\omega t + \theta_n - \phi_n) \quad (3.13)$$

$$P_n = \frac{D_n}{[(1 - n^2\tau^2)^2 + 4(\rho n\tau)^2]^{1/2}} \quad (3.14)$$

where, in addition to earlier definitions:

F_n = The nth multiple of the force

n = The nth multiple

θ_n = The phase angle of the nth multiple force

P_n = The maximum of the nth multiple position/amplitude

ϕ_n = The phase angle of the nth multiple amplitude

D_n = The relative force level of the nth multiple

Non-periodic Forces

Non-periodic, or arbitrary, external forces are transient by nature. A common way to investigate them is by considering an impulse force, i.e. a force that acts for a short, finite time, and possesses a significant amplitude. Equation 3.15 represents such a force. A spring-mass system that is subjected to this impulse will respond in free vibration with initial conditions of $x = 0$ and $\dot{x} = F/m$. Equation 3.16 describes

the resulting vibration, and it is evident that the frequency is that of the system while the amplitude is linear to the impulse force.

Excitation due to non-periodic external forces can be treated as a series of impulses by using the principle of superposition, illustrated in Figure 3.3. A superposition integral, in the form of equation 3.17, defines the response of the system.

$$f = \int_{t_1}^{t_2} F dt \quad (3.15)$$

$$x = \frac{f}{m\omega_n} \sin(\omega_n t) = fg(t) \quad (3.16)$$

$$x = \int_0^t f(t')g(t-t')dt' \quad (3.17)$$

Where, in addition to earlier definitions:

f = The unit impulse force

F = The amplitude of the impulse force

$g(t)$ = Response to the unit impulse force

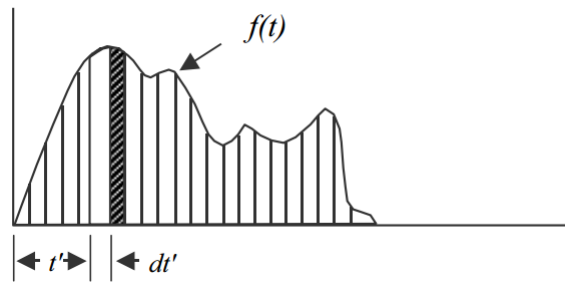


Figure 3.3: Damped spring-mass system [40].

From this it can be observed that the general response of the system is expected to be movement due to the impulse forces, in addition to vibration at a natural frequency, where the amplitudes depend on the timing as well as the magnitude of the forces.

Summary

Presented section serves as an introduction to the concept of vibration and points out distinctions between its forms. Periodic forcing functions will result in vibration at the the frequency of the force and its multiples (harmonics), with amplitudes depending on the proximity of the natural frequency, or any of its multiples, to the systems natural frequency. On the other hand, vibration due to non-periodic forces will occur at the systems natural frequency, with amplitudes that depend on the timing.

3.2 Application to Rotor Vibration

A compressor rotor can be considered as a multiple degree of freedom system that can exhibit both free and forced vibrations. The principles described in the previous section still applies, but the system is more complicated. The system consist of a rotor which represents the mass of the system, while stiffness and damping coefficients at any bearings and seals represent the spring components K and damping components C . Each of the bearings and seals have spring and damping coefficients in multiple radial directions. Figure 3.4 gives an illustration of how a rotor can be modelled.

3.2.1 Free Vibration

Considering a damped rotor, as in Figure 3.4a, for each degree of freedom, there will be a damped natural frequency called an *eigenvalue*. All these frequencies has a corresponding mode shape that describe the way the rotor vibrates, as well as a decay rate, defined by the logarithmic decrement. The consequence of this is that free vibration characteristics of the system as a whole will be a combination of all the natural frequencies and mode shapes. Angular velocities that coincide with a natural frequency of the rotor are known as critical speeds. Typically only the first critical speed is within a compressors operating range.

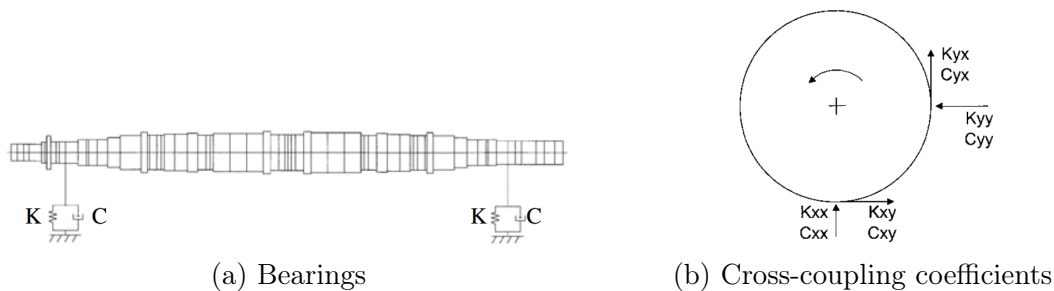


Figure 3.4: Rotor system model [40].

The situation most closely resembling free vibration is rotor instability, where a mode is caused only by the passive excitation, represented by the spring and damping coefficients in Figure 3.4b. This is not a phenomenon that is very relevant for this project, and will therefore not be discussed in detail. However, it is worth noting that the natural frequency of a rotor is in fact function of the total mass, including the impeller, as well as a function of the stiffness coefficients of the seals. This means that it is also a function of the density as well as the stiffness coefficients of the process fluid, i.e. GMF and flow pattern.

It is likely that this effect is negligible for a single stage compressor, both because the weight contained by the impeller at any given time is much smaller than the weight of the rotor and because the seals only have a minor role in supporting the rotor. For a compressor consisting of multiple stage, the mass of the gas stream is a much larger fraction of the combined weight, which means that the effect can be significant.

3.2.2 Forced Vibration

Harmonic Forces

The most common harmonic force on a rotor is unbalance, where the center of balance is out of alignment with the center of rotation. The frequency accompanying rotor unbalance is equal to the angular velocity of the rotor, often referred to as the 1Xrev, while the vibration mode shape will depend on how close the speed is to any natural frequencies. Since a perfectly balanced rotor is unrealistic, the 1Xrev vibration will always be present.

Generally a vibration signal due to a lasting harmonic external force is expected to be a steady vibration, with an amplitude depending on the forcing function and the proximity to a rotor natural frequency [40].

Periodic Forces

External periodic forces seen by compressor rotors are usually caused by aerodynamic forces. Vibration due to such forces will, as for the single degree of freedom systems, be at the frequency equal to the forcing function as well as its multiples. These type of forces are problematic because the presence of multiple harmonics means that they have a high chance of being in resonance with the rotors natural frequencies. The primary sources of these type of forces, stall and surge, will be described and discussed in chapter 4.

Arbitrary Forces

For arbitrary external forces the most common source is a transient aerodynamic event. The reaction of a rotor to transient activity is usually not evaluated analytically because of the innumerable variations that are possible. It is therefore left to evaluation of the signals in order to determine the possible cause, and whether they should cause any concern [40]. As for a single degree of freedom system, arbitrary forces can cause a vibration at a rotor natural frequency, and response excitations at a random frequency and amplitude.

Summary

Predictions about rotor dynamic behaviour is derived from basic one dimensional vibration problems. The most important findings are summarized as:

- Unforced sub-synchronous vibration, i.e. rotor instability, will give a relatively pure signal at the a natural frequency of the rotor.
- Forced sub-synchronous vibration due to a harmonic force will be a pure signal that does not need to be at a rotor natural frequency
- Forced sub-synchronous vibration due to a periodic force will be at the frequency of the forcing function and its harmonics. The existence of harmonics increase the chance for this frequency to coincide with a natural frequency and potentially causing resonance.

- Forced vibration due to non-periodic/impulse forces will be at continuously varying frequencies and amplitudes. Max amplitudes usually occurs near a rotor natural frequency.

With this basis, attention in the following sections is shifted towards the methods used for processing and obtaining and data.

3.3 Spectrum Analysis

Spectrum analysis is a widely used tool when vibration or just periodic phenomena in general are studied. This section gives a description of two different techniques that are used. The task for all spectrum analyzers is to take a continuous signal in the time domain and transform it into the frequency domain.

3.3.1 The Fast Fourier Transform

As mentioned in Section 3.1 any periodic signal, harmonic, or non-harmonic can be expanded in a Fourier series. This is the fundamental principle exploited by the Fourier Transform. The periodic square-like signal in Figure 3.5a illustrates this. The Fourier transform is employed to identify the combination of sinusoids that can replicate such a signal (3.5b). The resulting spectrum in the frequency domain displays the fundamental frequency with highest amplitude, and several harmonics at integer multiples of the fundamental frequency (3.5c).

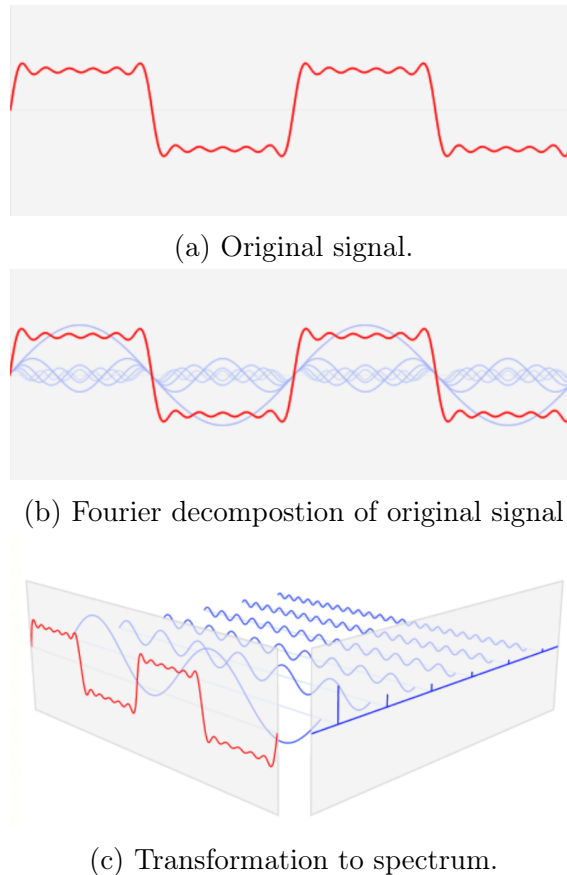


Figure 3.5: The principle of the Fourier transform [13].

A disadvantage of the Fourier transform is that the time information is lost during the process, meaning that any non-periodic events will not be detectable. This issue is solved by the Fast Fourier Transform (FFT), which discretise the Fourier transform into a set number of sample points. The resulting spectrum then adds the a time axis, which makes it possible to identify transients.

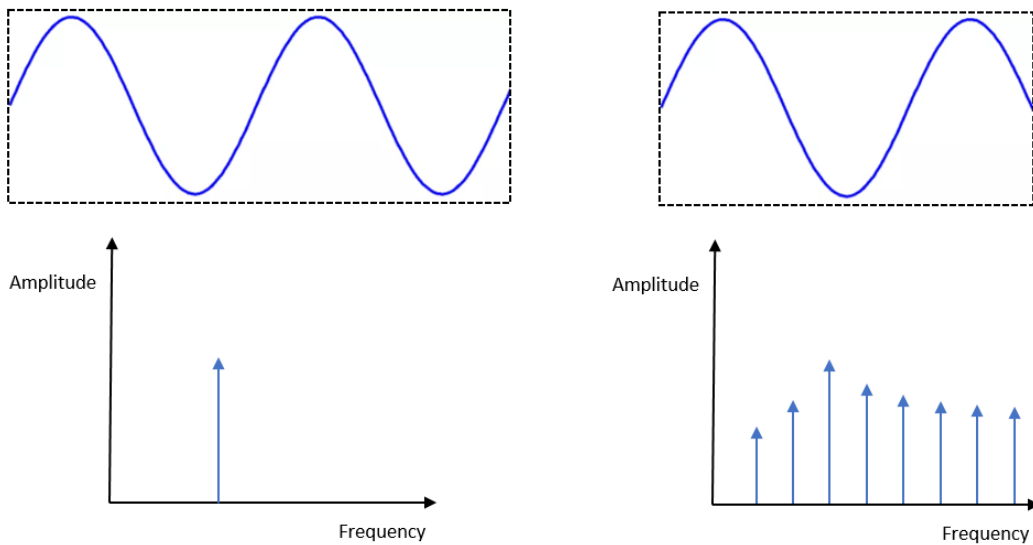
A detailed description of the algorithms that carries out the FFT is not given here, as this belongs more to the field of signal processing than turbomachinery engineering. FFT has an innumerable amount of applications within engineering and mathematic disciplines and was in 1994 described as "the most important numerical algorithm of our lifetime" by G. Strang [57].

Windowing

When the FFT is used to measure frequency components of a signal, the analysis is based on a finite set of data. The time domain and the frequency domain are circular topologies, implying that the endpoint of the waveforms are interpreted as if the endpoint of the wave within one sample point is connected with the wave within the next sample point. This is fine if the measured signal is periodic and an integer number of periods fill the acquisition time interval, such as in Figure 3.6a. In most scenarios however, this will not be the case. The unfortunate implication of this is that the measured signal may result in a truncated waveform with different charac-

teristics from the original signal. In particular, sharp transitions appear between the acquisition time intervals. These artificial transitions result in false high-frequency signal components, and the spectrum will represent a smeared version of the original signal. It appears as if energy contained within one frequency leaks into other frequencies. This is known as *spectral leakage* and an example is shown in Figure 3.6b.

The actual signal frequency is shown with the highest amplitude. It is called the *main lobe*, and it is surrounded by unwanted components, known as *side lobes*. If two signals of different amplitude are situated close to each other in the frequency domain, the side lobes of the stronger signal may overpower the main lobe of the weaker signal.



(a) Harmonic signal with integer periods. (b) Harmonic signal with non-integer periods.

Figure 3.6: Spectral leakage in FFT.

In order to minimize the effects of spectral leakage it is possible to employ a technique called windowing (Figure 3.7). Windowing attempts to remove spectral leakage by making the endpoints of the waveform meet. It does this by multiplying the time record by a finite-length window with an amplitude that gradually goes towards zero at the edges, thus creating a waveform that is without sharp transitions across the sample intervals. This reduces the magnitude of the side lobes in the resulting spectrum - it causes the side lobes to "roll off".

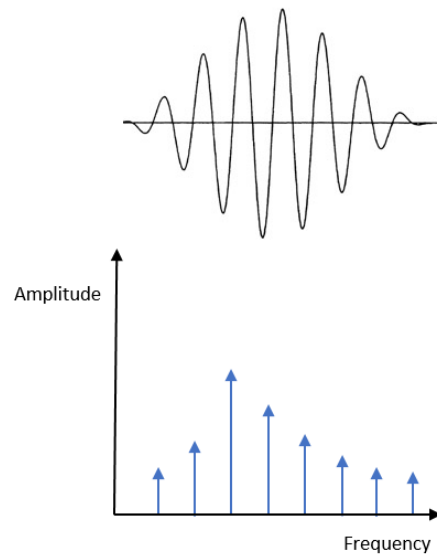


Figure 3.7: The effect of windowing.

A number of different windows are available, each with its own characteristics. The selection of window is a trade-off between roll-off rate, amplitude accuracy and frequency resolution. National Instrument's [33] recommendations for window choice is give in Table 3.1.

Table 3.1: National Instruments recommendation for FFT window choice.

Signal	Window
Sinewave or combination of sine waves	Hanning
Sinewave (amplitude accuracy is important)	Flat Top
Narrowband random signal (vibration data)	Hanning
Broadband random (white noise)	Uniform
Closely spaced sine waves	Uniform, Hamming
Excitation signals (Hammer blow)	Force
Response signals	Exponential
Unknown content	Hanning

The Hanning window is a compromise between good frequency resolution and reduced spectral leakage. It is therefore claimed to be satisfactory in 95% of the cases. It is also pointed out that for analyzing transients such as impact and response signals, the exponential window is useful because it damps the end of the signal, ensuring that the signal fully decays by the end of the acquisition interval. A window that does not manipulate the side lobes at all is referred to as a rectangular window.

Power spectral density

The data can also be displayed as power spectral density (PSD). The power spectrum is the average of the squared magnitude of a number of successive instantaneous spectra. The magnitude of the PSD is normalized to a single Hertz bandwidth, hence the word "density" is used. PSD more accurately assigns the power to the

correct frequencies and averages to reduce noise-induced fluctuations in the power amplitudes. The tradeoff is that the frequency resolution is reduced because fewer data points are available for each FFT calculation.

Noise

The noise level can be quantified by calculating the Signal-to-noise ratio (SNR). Within a given bandwidth it is defined as the ratio of the power of the signal of interest and the power of background noise:

$$SNR = \frac{P_{signal}}{P_{noise}} \quad (3.18)$$

where P is the average power. SNR excludes the harmonics of the signal from its calculation. Signal-to-noise and distortion ratio (SINAD) is another indicator of the the noise level. It is defined in Equation 3.19 as the ratio of total power and unwanted power. The unwanted components include both noise and distortion, where distortion is both harmonics and *spurs*.

$$SINAD = \frac{P_{signal}P_{noise}P_{distortion}}{P_{noise}P_{distortion}} \quad (3.19)$$

Spurs are frequency components that sometimes accompany a signal. These are usually caused by electrical components of the instrument, and examples of spurs include interleaving anomalies in analog-to-digital converters (ADCs) and leakage of oscillator clock signals [31]. Similarly to harmonics they are normally smaller in amplitude than the fundamental frequency component, but they appear at random non-integer frequencies of the fundamental frequency. The main difference between SNR and SINAD is that SNR excludes harmonics from its calculation. Figure 3.8 illustrates what a real spectrum may look like.

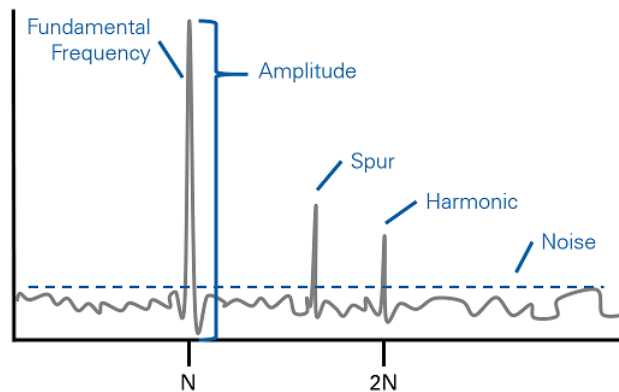


Figure 3.8: Spectrum with noise and signal with associated spur and noise [31].

3.3.2 Wavelet transform

The Continuous Wavelet transform (CWT) is an alternative to the Fast Fourier transform. It is a relatively new signal processing tool developed in the late 80's

mainly used for data compression and image processing, but can also have utility value in vibration analysis. It is included because it is pointed out by several researchers as an improved method of compressor transient detection, e.g. [51] and [34]. Similarly to the Fourier transform it is a linear operation that transforms an input signal to a frequency domain, but instead of sine waves the wavelet transform uses wavelets as basis functions. Wavelets are waveforms of effectively limited duration that has an average value of zero, described by its "mother"-function ψ :

$$\psi_{a,b}(t) = \frac{1}{\sqrt{a}} \psi\left(\frac{t-b}{a}\right) \quad (3.20)$$

with a as the parameter of compression and b as time translation. This means that a wavelet can be compressed or expanded in its frequency and located in time [51].

The main selling point of the wavelet transform is illustrated in Figure 3.9. It shows the difference in time resolution at ascending frequencies for the Fourier transform and the wavelet transform. All frequencies within the Fourier transform uses the same time window (in this case a simple square window) and therefore the maximum resolution is restricted by this windowing. The wavelet transform, due to its transformation method, uses a dyadic time resolution which scales with the frequency. This means that it gives a more correct interpretation of transient signals at low frequency and a faster detection of transient high frequency signals [51].

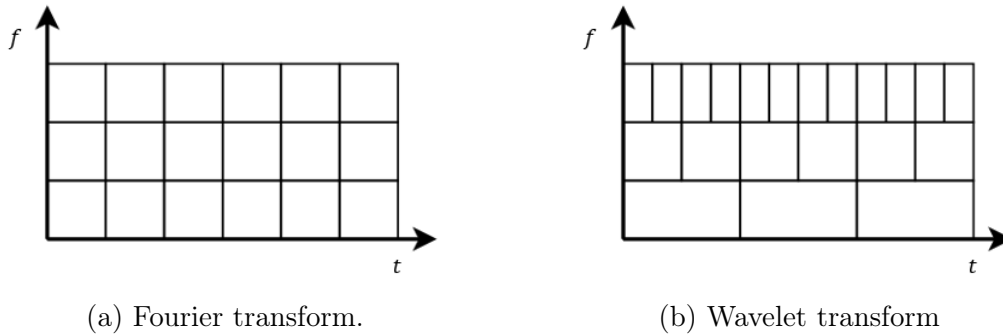


Figure 3.9: Time-Frequency resolution

CWT is very efficient in determining the damping ratio of oscillating signals, and is also very resistant to the noise in the signal [38].

3.4 Signal detection

The gathering of signal data relies on proper selection of transducers. In a compressor, transducers can either monitor the motion of the rotor, or the flow field itself.

Vibration transducers

Shaft vibration is measured using displacement transducer, velocity transducers or acceleration transducers. Accelerometers are full-contact transducers typically

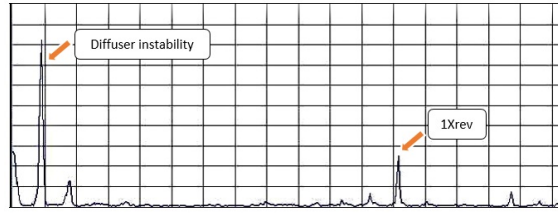
mounted directly on high-frequency elements, such as a bearing. Advantages include linearity over a wide frequency range and a large dynamic range. Velocity transducers has a limited response range, and is therefore rarely preferred over accelerometers. Displacement transducers are non-contacting probes that measure distance to a target. These are used almost exclusively in rotating machinery to measure shaft vibration and are suitable for detecting low frequency vibrations [32].

Dynamic pressure

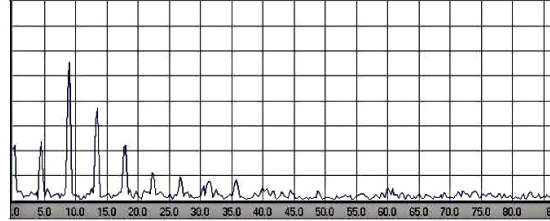
Dynamic pressure sensors can be placed in direct contact with the compressor flow. These pressure sensors are often piezoelectric ("electric from pressure"), where a crystal is mounted in such a way that any force applied to it either stretches or compresses it. The crystal then generates a charge proportional to the force. Piezoelectric technology is very effective at measuring changes in pressure due to the piezoelectric materials high modulus of elasticity, enabling an excellent linearity over a wide amplitude range [50].

If the pressure applied on a piezoelectric pressure transducer remains constant, charge migration in the material and its surroundings will nullify the charge separation in the material, and the electric charge will eventually leak to zero. The consequence of this is that the piezoelectric material is only suitable to record dynamic events, and the absolute value of the static pressure is not a valid measurement [48].

Since the dynamic pressure sensors are placed in the gas flow they are excellent for detecting aerodynamic instabilities. Figure 3.10a gives a vibration and a dynamic pressure spectra taken at the same time by Marshall and Stokes [40]. The forces originate from a flow instability in the compressors diffuser, which gives a signal with multiple harmonics. Some of the information is lost in the vibration signal, which only shows the primary signal with a very high amplitude and the first harmonic. This is symptomatic for systems which have high damping relative to stiffness. It can also be noticed that the 1Xrev frequency is visible on the vibration spectrum, but not on the dynamic pressure data.



(a) Vibration



(b) Dynamic pressure

Figure 3.10: Vibration and dynamic pressure spectra [40].

In order to minimize undesirable flow intrusion effects such as turbulence it is desirable to flush mount the dynamic pressure sensors. This assures that the sensors ability to measure high frequency pulsations is not degraded [46].

3.5 Attenuation

In idealized materials, the energy contained in a travelling pressure wave is conserved and the reduction in amplitude is only due to the spreading of the wave. A wave that travels through real materials however, will lose its energy due to scattering and absorption. This effect is known in physics as attenuation, and is a general term that applies to gradual loss in intensity of any kind of flux through a medium. This section intends to shed light on the mechanisms that can make detection of pressure signals difficult, particularly in wet conditions.

For a pressure wave the attenuation is expressed as:

$$p = p_0 e^{-\alpha x} \quad (3.21)$$

where p_0 is the amplitude at some initial point, x is the distance travelled and α is the attenuation coefficient. The attenuation of pressure in a homogeneous flow is caused by viscous shear stresses. It can be estimated by using *Stokes' law of sound attenuation* [56]:

$$\alpha = \frac{2\nu f^2}{3a^3} \quad (3.22)$$

The most dominant term here is the speed of sound, which when cubed, is inversely proportional to the attenuation coefficient. A peculiarity of multiphase flow is that adding small amounts of liquid in a gas will reduce the acoustic velocity by a large amount; even though liquids generally have a higher speed of sound than gases. Several multiphase speed of sound models exist. One that is commonly referred to is Wood's model [66]. It is defined by equation 3.23 and plotted for an air/water

mixture at atmospheric conditions on mass basis in figure 3.11. This model assumes homogeneous flow and only gives reasonable estimates at high GMF.

$$a_{mp} = \sqrt{a_g^2 \frac{1 + \frac{1-GVF}{GVF}}{GVF \left(1 + \frac{1-GVF}{GVF} \frac{\rho_l}{\rho_g}\right)}} \quad (3.23)$$

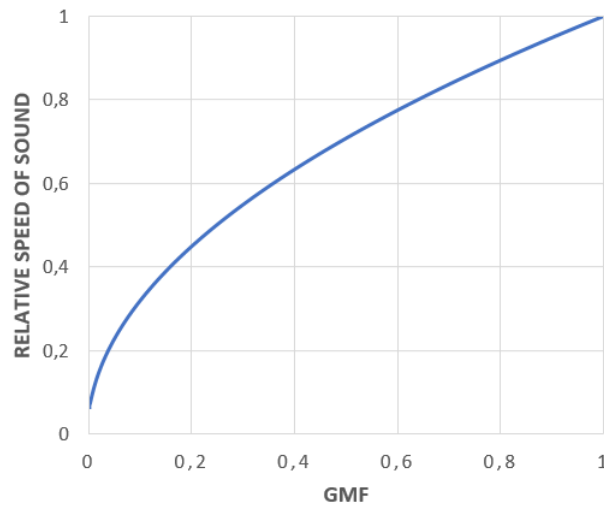


Figure 3.11: Speed of sound in homogenous water/air mixture.

This suggest that a decrease in GMF will increase the attenuation coefficient and thereby weaken the pressure wave at a faster rate. The attenuation coefficient is also highly dependent on the frequency of the signal. For instance, a typical impeller blade pass signal at 2000 Hz will have an attenuation coefficient that is 1 million times larger than a surge signal at 4 Hz.

A phenomena that becomes relevant when multiphase flow is considered is illustrated in Figure 3.12. When a wave propagates into the boundary between two media, a portion of the wave undergoes reflection and a portion of the wave undergoes transmission across the boundary.

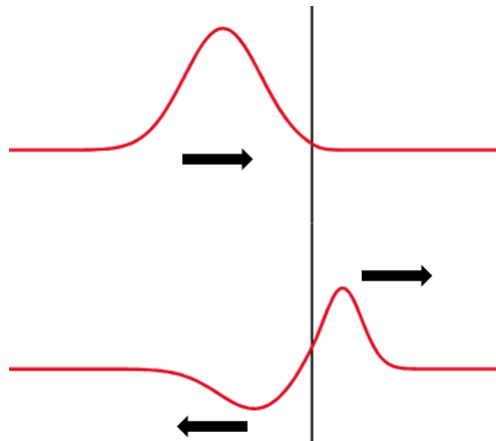


Figure 3.12: Pressure wave propagation across boundary.

The amount of reflection and transmission depends on the acoustic *impedance* of the materials. Impedance is a property that quantifies the opposition of a medium to wave propagation. The specific acoustic impedance of a medium opposing the propagation of a plane pressure wave is equal to:

$$Z = \sqrt{K\rho} \quad (3.24)$$

where K is the stiffness of the medium and ρ is the density of the medium. Impedance can be related to the speed of sound by introducing the relation $K = c^2\rho$:

$$Z = \rho a \quad (3.25)$$

The reflection coefficient is related to the impedance across a boundary as defined by Equation 3.26 and the transmission coefficient is defined in Equation 3.27 [37].

$$R = \frac{Z_1 - Z_2}{Z_1 + Z_2} \quad (3.26)$$

$$T = \frac{2Z_1}{Z_1 + Z_2} \quad (3.27)$$

where, referring to Figure 3.12 subscript 1 represents the material left of the boundary and subscript 2 represents the material right of the boundary. This means that liquid/gas interfaces, characterized by large difference in density and speed of sound will have a very low transmission coefficient. The dispersed liquid droplets in the compressor will create a condition where especially the weak signals will tend to echo and disappear into noise. Additionally, the appearance of a liquid film between a pressure sensor and a pulsation source may appear as rigid for a weak pressure signal and block it altogether.

In summary, Stokes' law of sound attenuation states that high frequency signals are attenuated very quickly, especially at reduced acoustic velocity. Additionally, the multiphase flow regime will introduce reflection effects that may scatter and corrupt the signals. This means that detecting pressure signals is expected to be more difficult in wet conditions.

COMPRESSOR INSTABILITIES

The operating range of a centrifugal compressor is limited in the low flow region by the aerodynamic performance of its components. This chapter picks up the thread from Chapter 2 and relates the nature of compressor instabilities with vibration theory. This is followed by a literature review on alternative techniques of detecting transients before addressing possible challenges related to slug flow and GMF fluctuations.

4.1 Stall

Aerodynamic stall is a phenomenon that is often associated with aviation, but it is in fact relevant in all applications that depends on an airfoils that are able to generate a lift force from the fluid pressure difference, or vice versa. If the adverse pressure gradient becomes too strong in a boundary layer, flow separation and vortex formation will occur. This in turn deteriorates the airfoil performance by increasing its drag force and decreasing its lift force. In the case of a compressor, this will become apparent as a decline in produced head.

Although stationary stall can be present in compressor components such as return channels, guide vanes or volute tongues; most of the concern in centrifugal compressors is directed towards its more common rotating counterpart, because rotating stall is associated with continuous pressure pulsations within the machine that can cause rotor instability and blade fatigue.

Rotating stall can take place in both the impeller and the diffuser. It takes shape of a nonuniform circumferential pressure field that rotates at a certain speed relative to the impeller speed. This means that vibration or dynamic pressure data can be used to detect it.

4.1.1 Impeller rotating stall

According to Marshall and Sorokes [40], many researchers have investigated impeller stall, and there is almost an equal number of theories about its nature and influence of compressor performance. The classical impeller stall that is usually described in textbooks starts in the inducer section.

Figure 4.1 shows the inlet velocity diagram of the impeller at best efficiency point. A decrease in flow rate, corresponding to a decreased fluid velocity C_1 ; or increased compressor speed, corresponding to a larger peripheral velocity U_1 ; will lead to a larger angle of attack, and a thickening of the boundary layer on the suction side of the blade. If the angle is increased above a certain point, flow separation will occur and region of stalled flow is formed, usually referred to as a stall cell.

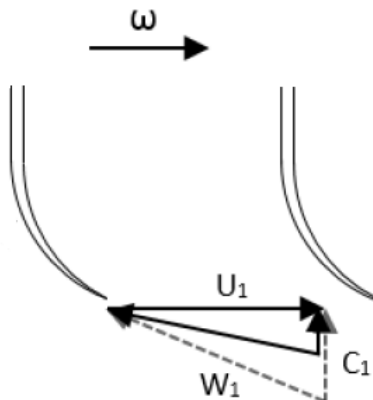


Figure 4.1: Impeller inlet velocity diagram.

Figure 4.2 illustrates rotating stall as explained by Saravannamutto et al. [53]. A flow breakdown in channel B causes the air to be deflected in such a way that channel C receives fluid at a reduced incidence angle, and channel A at an increased incidence angle. Channel A then stalls, causing an incidence angle reduction and stall recovery in channel B. The stall therefore passes from channel to channel in the opposite direction of impeller rotation.

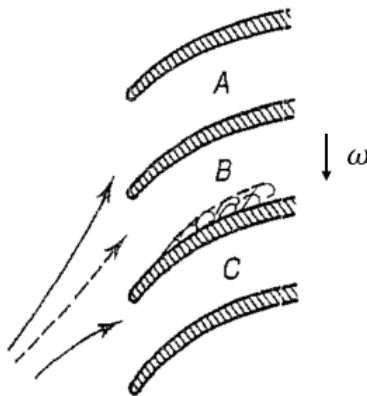


Figure 4.2: Impeller rotating stall [53].

Frigne and Van den Braembussche published an extensive work on rotating stall in 1984 [22]. They made a distinction between two types of impeller stall; progressive stall and abrupt stall. Progressive stall, which is the phenomenon explained in the previous paragraph, is a consequence of the impeller flow field itself, usually triggered by the impeller incidence angle. Abrupt stall on the other hand, by some referred

to as interaction stall, is a result of flow perturbations at the impeller exit that disturbs the flow through the impeller. A possible reason is the diffuser walls being misaligned and causing interference with the impeller exit, which results in a strong interactions between the impeller and the diffuser. Furthermore, the frequency range at which the two types of impeller stall occurs was also identified. Progressive stall is said to occur at 50 to 80 percent of compressor running speed, while abrupt stall occurs at 20 to 40 percent of running speed. Typically there is no hysteresis zone associated with impeller stall, meaning that the onset will appear at some flow rate, and disappear again if the flow is increased beyond that point. The pressure pulsations associated with impeller stall are relatively harmonic [40].

4.1.2 Diffuser rotating stall

The diffuser is by nature a component that is vulnerable to flow separation since it is specifically designed to contain an adverse pressure gradient. A reduction in flow rate reduces the impeller outlet angle and elongates the flow path in the diffuser, i.e. the distance of viscous interaction is increased. This can lead to flow separation and reversal in the boundary layers. Some confusion may arise due to the fact that the diffuser is not an airfoil, and can not experience stall by the definition given in the introduction of the chapter. However, the term is also commonly used in fluid mechanics to describe breakdown of diffuser performance, e.g. [65].

As in the impeller, stall in a vaneless diffuser also rotates at some speed relative to the compressor speed. Diffuser rotating stall is illustrated in Figure 4.3. It is initiated if a region at the outer edge of the diffuser is brought to a halt and forms a stall cell. This stall cell then acts as a blockage for the flow on either side of it, and changes the path of the fluid stream above the blockage to a more radial direction, implying a reduced flow path and stabilization. The flow below the stall cell will incline in a tangential direction, elongating its flow path and cause a new stall cell to form. The mechanism is similar to the stall propagation in the impeller, but it rotates in the opposite direction.

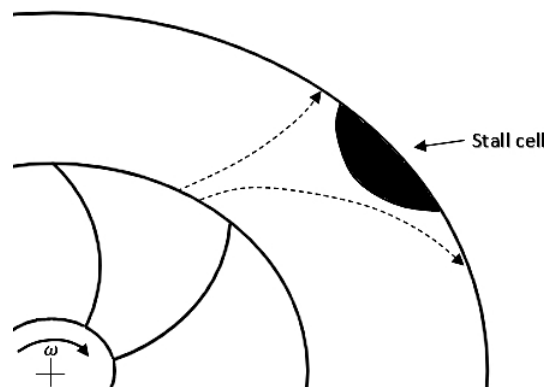


Figure 4.3: The principle of diffuser rotating stall.

Figure 4.4 shows rotating stall in a vaneless diffuser documented by Ohuchida et al.[44]. The colour indicate the magnitude of the radial velocity component. For

the stall cells (blue) the velocity is zero. Particle image velocimetry (PIV) was used to obtain the results.

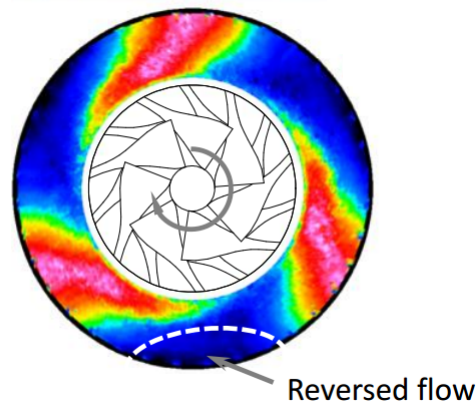


Figure 4.4: Diffuser rotating stall [44].

The frequency of the pressure pulsations depend on the number of stall cells. Frigne and Van den Braembussche reported typical values of 6-33 percent of running speed.

Cumpsty [14] makes a differentiation between full-span stall and part-span stall. As illustrated in figure 4.5, stall can either exist as multiple cells around the annulus or as one cell that extends across the it. The frequency of part-span cells is around 50% of rotating speed, while full-span cells usually rotate more slowly in the range of 20-40%. Sudden jumps in frequency will occur if new stall cells are formed. In the case where part-cell stall are placed symmetrically around the annulus, the radial forces acting on the rotor cancel each other. Dynamic pressure sensors placed in the gas stream is therefore more suited for detecting rotating diffuser stall.

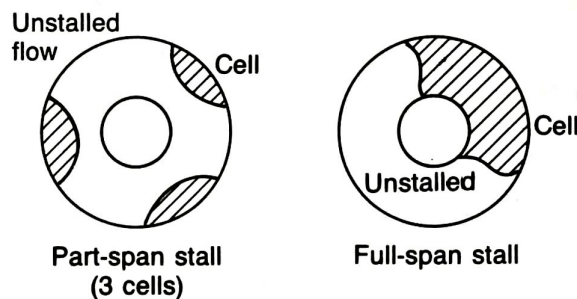


Figure 4.5: Part-span stall and full-span stall [14].

Contrary to impeller stall, there is usually a hysteresis zone associated with diffuser stall flow rate, meaning that the flow rate has to be increased significantly beyond the original stable limit after stall has occurred, in order to "wash out" the stall cells. The pressure pulsations created by diffuser stall is also characterized by prominent harmonics [40].

Whether the impeller or diffuser stalls first in a vaneless diffuser is difficult to determine, but various opinions are found in the literature. According to Boyce [9],

extensive testing has shown that flow separation tends to occur first in low pressure ratio compressors. For machines with single-stage pressure ratio exceeding 3:1, flow separation usually starts in the inducer. Kammer and Rautenberg [36] conducted experiments on a low pressure ratio machine and concluded that at lower speeds the impeller is likely to cause compressor stall, while at higher speeds the diffuser is more likely to stall first. Certainly the choices made in the design process of the compressor also matters a great deal. As explained in Section 2.2 the flow pattern and boundary layer stability in the impeller is strongly related to the meridional curvature. Also, the destabilizing adverse pressure gradient in the diffuser can be manipulated by making the channel converge from inlet to outlet.

Rotating stall is a mechanism that allows the compressor to operate steadily. Even though individual sections of the compressor is subject to flow oscillations, the total throughput is constant. Generally, a properly designed compressor will only encounter stall when operating in the left limit range. Rotating stall is often a precursor to the more severe aerodynamic phenomenon that is surge.

4.2 Surge

While centrifugal compressor can operate fairly satisfactory with moderate stall this is not the case if the compressor surges. Surge occurs if the adverse pressure gradient is strong enough to cause flow reversal across the whole annulus, leading to instabilities across the entire compressor system. Whereas stall is caused by compressor components being forced to operate outside their aerodynamic limit, surge is caused by the compressor as a whole not being capable of delivering the head that the receiving system requires.

With respect to the compressor characteristics, surge is often defined as the operating point at which the compressor peak head capability and minimum flow limit are reached, e.g. [35]. This is somewhat misleading because this point is more often the point where stall prevents the compressor from delivering more head, but the compressor does not necessarily enter surge. The area left of this point is anyways referred to as the *surge area* and this is the area where it is possible to encounter surge.

Figure 4.6 introduces the *extended compressor curve*. Left of point A, the compressor enters an area of instability. This is an area where a decrease in flow also leads to a decrease in pressure, i.e., a positive slope. Eventually the compressor will reach a point of no flow (C). Since the diffuser cannot increase pressure without a flow, the pressure is equal to the head produced by the impeller. Backflow then occurs if the downstream pressure is greater than the combined upstream- and impeller produced pressure. Hence, the pressure gradient changes direction when the ordinate is crossed.

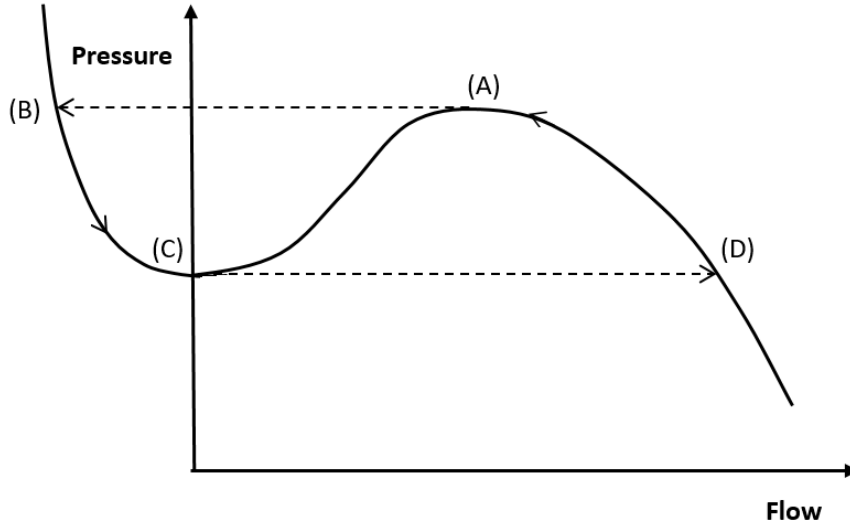


Figure 4.6: Extended compressor curve and deep surge

Also shown in figure 4.6, is the *deep surge* cycle as illustrated by Gravdahl and Egeland [24]. It is explained by considering a compressor that feeds a reservoir with a finite volume. Deep surge is a cycle consisting of four stages. It starts near the zero-slope point where the flow becomes unstable (A). Because the system requirement is greater than what the compressor can deliver, the operating point is forced into the backflow region, where it finds a point with high pressure (B). The upstream pressure then drops since the reservoir downstream of the compressor is being emptied. As the compressor crosses the point of no flow (C), it needs to find a point of lower pressure. It therefore jumps to point (D), and follows the characteristic back to (A), initiating a new cycle.

Surge may also take the form of a smaller scale flow oscillation around a point in the positive flow region of the compressor map. This is usually referred to as *mild surge*. The oscillation frequency of mild surge can be estimated for a geometry as in figure 4.7 by calculating the Helmholtz resonance frequency of the compression system [17]:

$$f_H = \frac{a_p}{2\pi} \sqrt{\frac{A_C}{V_p L_C}} \quad (4.1)$$

where a_p is the speed of sound in the plenum, V_p is the volume of compressed air, A_C is the equivalent cross-sectional compressor duct area, and L_C is the equivalent length of the duct. The Helmholtz frequency is essentially the natural frequency of the duct-plenum system, in other words the frequency at which the air will tend to vibrate when subjected to perturbations from the compressor. The derivation of the Helmholtz frequency is found in Appendix A.1.

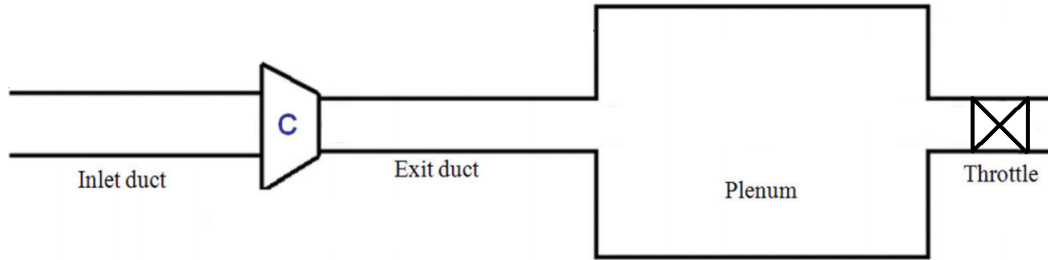


Figure 4.7: Compressor system with exit duct and plenum [21].

A further differentiation between the different types of surge is made by de Jaager [16]. Classic surge, and modified surge is described in addition to mild surge and deep surge. Classic surge is defined as a more severe form of mild surge, where the oscillations are larger and slower, with a less linear flow pattern and prominent harmonics. Modified surge is described as being a mix of rotating stall and surge, where the entire annulus flow fluctuates in the axial direction, but rotating stall is superimposed, so the flow is unsteady and non-axisymmetric.

A number of dimensionless models has been developed in order to predict surge behaviour in both axial and centrifugal compressors. Greitzer's approach [25] is the model most often referred to in literature. It formulates a set of nonlinear equations to estimate the system dynamics for the same configuration as in figure 4.7. The purpose of it is to estimate the type of instability that the compressor will encounter. The model defines a dimensionless number:

$$B = \frac{U_2}{2a_2} \sqrt{\frac{V_p}{A_C L_C}} \quad (4.2)$$

where, in addition to definitions given above, U_2 is the impeller blade tip speed and a_2 is the impeller tip speed of sound. The B-parameter can be given a physical meaning by rewriting it as:

$$B = \frac{(\rho U_2^2 / 2) A}{\rho A_C L_C U f_H} \quad (4.3)$$

where the numerator gives an indication of the pressure rise capability of the impeller multiplied with impeller eye area. In other words it represents the force that the impeller produces. The air velocity out of the compressor can be assumed to be approximately proportional to the tip speed U_2 . This component is in the denominator together with the mass ($\rho A_C L_C$), and therefore represents the force required to produce small oscillations of the flow in the duct at the Helmholtz frequency. The parameter can therefore be interpreted as the ratio of the compressor rise capability and the pressure rise required to induce mass flow oscillations.

Greitzer states that with a given compressor, there is a critical value of B. For larger values the mode of instability encountered at low flow will be flow and pressure oscillations that characterize mild surge; for much larger values the resulting instability will be deep surge, which may include negative flow; for smaller values the result of the instability will be a transient to a new operating point in rotating stall at a reduced flow and pressure head [25].

McMillan and Gregory [6] suggest using this model also for compressor system that does not resemble a typical Helmholtz resonator, but only contains an outlet pipe between the compressor and the choke valve. In this case the L_C (length of the duct) is replaced by the length of the flow path in the compressor, while the outlet pipe represents the plenum volume V_p .

As an example of surge, Figure 4.8 reports experimental data of a test performed by Fink [21] at a high B-value compressor system. The deep surge period is divided into four phases, starting with a quiet build-up period at stable flow, before entering a mild surge (instability growth) where the Helmholtz resonance period is clearly visible. The flow coefficient is based on velocity measurements from a hotwire anemometer, which does not measure flow direction. In order to distinguish between forward and reverse flow during deep surge, Fink applied a mass balance to the plenum volume and estimated the flow coefficient from it. The flow coefficient derived from the plenum mass balance confirms that the flow is reversed during the "blowdown" phase, which is followed by a recovery period and initiation of a new surge cycle.

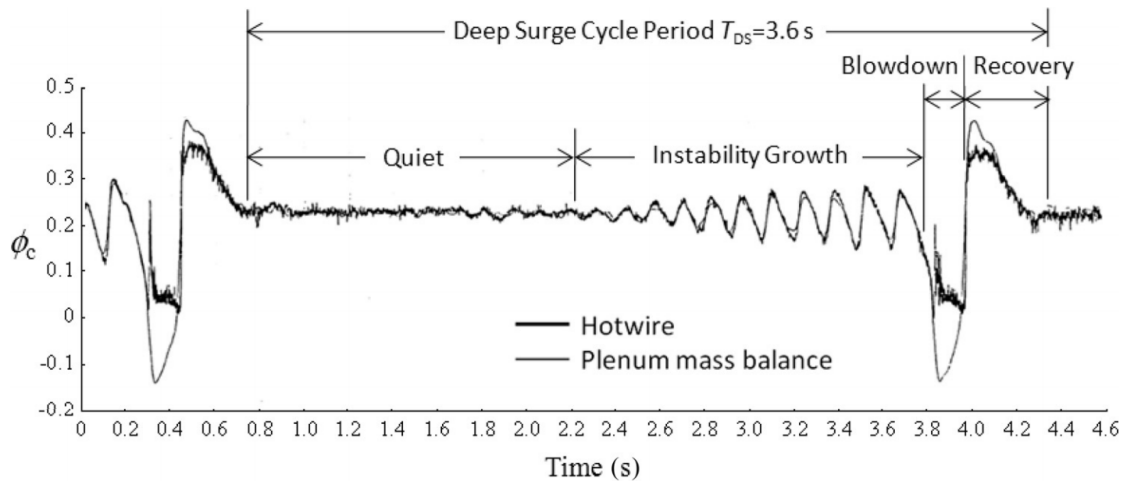


Figure 4.8: Flow coefficient calculated from hotwire velocity measurement and plenum mass balance during surge [21].

Surge is a highly unwanted event during operation that leads to large forces acting on the compressor. Although the surge process may become effectively axisymmetric when fully developed, this is not the case during preceding transient. One of the most damaging effects of surge is the large transverse load that is placed on the rotor because of the non-axisymmetric of the transient, leading to impeller blades rubbing against surfaces [14]. Surge is also accompanied by axial vibration due the flow fluctuations.

4.3 Wet gas stall and surge

A glance at the streamwise moment equation provides a simple prediction related to flow separation when conditions are changed from dry to wet; for a given pressure

gradient, an increase of the fluid mixture density will hinder the deceleration and thus delay flow separation. This also means that if the flow is segregated, flow separation is more likely to occur in the lighter gas phase.

In reality, the multiphase interactions are complex and single phase assumptions are not valid. Multiphase flow is known to deteriorate the performance of airfoils. Grüner [26] conducted air/water experiments and found a degraded performance decreased gas mass fractions owing to premature boundary layer separation. This coincide with reports from aeronautical science, e.g. [63], where Wan and Wu found the degradation of airfoil performance to be most prominent at high angles of attack and low flow. The studies that are done on axial compressors, which are fully dependent on efficient airfoils, reflect this. Day et al. [15] investigated the effect of rain ingestion in a an axial compressor and found premature stalling in most cases. Similar results were obtained by Roumeliotis and Mathioudakis [49], who reported a negative influence on the surge margin.

For a centrifugal compressor, the consequence of wet operation is not limited to airfoil performance. The pressure head produced by the impeller is due to centrifugal effects, which will occur even in the presence of flow separation. It also introduces a completely different flow pattern, which depending on composition and operating conditions, contains regions of segregated flow and regions of more homogeneous flow. The reports on wet gas test on centrifugal compressors therefore tell a different story. The consensus from tests obtained at the NTNU compressor rig is that liquid injection extends the instability onset at low flow. This has been observed by both Grüner and Bakken [27], and Ferrara [20]. Earlier findings on wet compression supports this, e.g. [64], where Wang et. al found an increased surge margin for a small gas turbine with a two-stage centrifugal compressor.

None of the researchers are categorical in explaining the reasons for it, and it remains somewhat obscure. Grüner pointed to the liquid imparting momentum to the gas flow and divert the flow into a more favorable path. This is in agreement with what was established in Chapter 2, where the reduced flow path in the diffuser and delayed pressure build up in the volute were considered to be stabilizing factors.

Recalling that the sound of speed decreases with increasing liquid content, and knowing that the Helmholtz resonance frequency is proportional with the acoustic velocity in the plenum, it can be assumed that the frequency associated with mild surge will decrease during wet conditions. The Greitzer B-parameter depends on the impeller tip Mach number and is inversely proportional to the acoustic velocity. According to Greitzer's model, the flow range at which rotating stall is present is therefore reduced during wet conditions. A more direct transition into surge can be expected.

A weakness of the Greitzer's model with respect to multiphase flow is that it does not account for the adjusted flow pattern which change the nature of instability onset. For a given compressor the B-parameter cannot simply be adjusted with GMF in order to predict the mode of instability. One way to accomodate for this would be to replace the term $\rho U_2^2/2$ with the pressure difference across the entire compressor at the point of instability ($p_{out} - p_{in}$). This would however be more cumbersome, because the compressor operating points at which instability occurs for different GMF would need to be identified in advance.

4.4 Dynamic surge detection

Since compressor surge is a highly unwanted event, it is common to employ an anti-surge system which prevents the compressor from entering the unstable area. Anti-surge systems are based on flow recycling, which means that the compressor is brought out of the dangerous region by opening a valve that redirects the flow at the outlet back to the inlet. The standard procedure for deciding which point recycling is initiated is by coupling the control system to a flow element upstream of the compressor. The surge point is then identified from the compressor characteristics and a margin is added, typically around 10% [35]. This can be described as *static surge detection*, and is what gas processing compressors is equipped with.

Even though compressors operate with a margin, surge may still occur due to inappropriate compressor design, poor matching of the compressors to the system's requirement or inadequate anti-surge control systems [9]. Many researchers has looked towards developing systems that can detect the transient behaviour associated with surge before the situation becomes critical. These can be described as *dynamic surge detection* systems. A literature review of some of these systems are given since they are, in essence, methods for detecting transients.

Figure 4.9 shows an illustration of a system proposed by Boyce [8]. Velocity probes are installed in the boundary layer of the diffuser. Flow reversal in the boundary layer is then detected and interpreted as impending surge. A bleed line is connected to the diffuser which opens and recycles a portion of the boundary layer flow back to the compressor inlet.

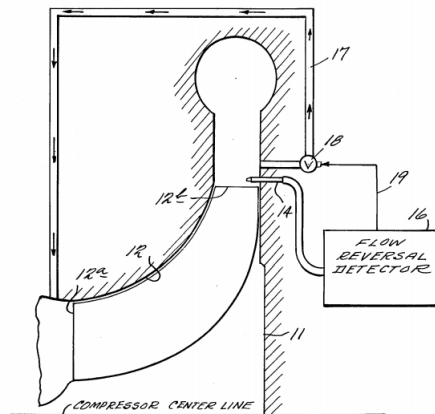


Figure 4.9: Dynamic surge detection based on diffuser boundary layer probes [8].

Ferrara [20] observed that flow reversal distinctively started on the shroud side, during wet conditions as a consequence of the increased momentum in the impeller liquid film. This is illustrated in Figure 4.10. One could therefore argue that the signal that is sent from the probe to the reversal detector is going to be less ambiguous than if instabilities could start at both sides, as is the case for dry gas. For wet gas this system may therefore be appealing, although the probe would need to be on the opposite side or both sides.

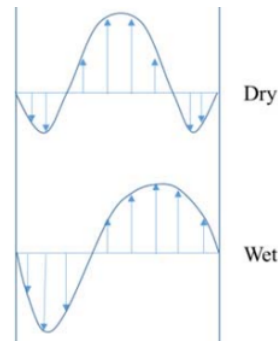


Figure 4.10: Velocity profile in diffuser towards surge [29].

The diffuser flow pattern have been investigated in previous experimental campaigns on the NTNU test rig, e.g. [55] and [58]. Measurement techniques include differential pressure readings and multi-hole probes.

Figure 4.11 shows an illustration of a surge protection system proposed by McKee and Carl [41] in 2006. It was observed during laboratory testing of a small centrifugal compressor that a recirculation zone (42) develops in the inlet passage just upstream of the impeller as the compressor approaches surge. Flow and relative temperature is measured near the wall of the inlet passage (22). During normal operating conditions, the inlet flow (38) is uniform in temperature and the axial velocity may be described as steady state. As the compressor operating point moves towards surge, the flow velocity near the inlet wall decrease considerably more than the mean flow through the inlet, before reversing and creating a recirculation zone. Consequently, the temperature of the gas in the outer inlet area increases relative to the bulk inlet gas temperature. A tangential or rotational component is also imparted to the impeller suction flow near the wall. These changes can be measured by installing velocity and/or temperature probes at the inlet wall. If the control system receives measurements indicative of incipient surge, a traditional recycling system is activated.

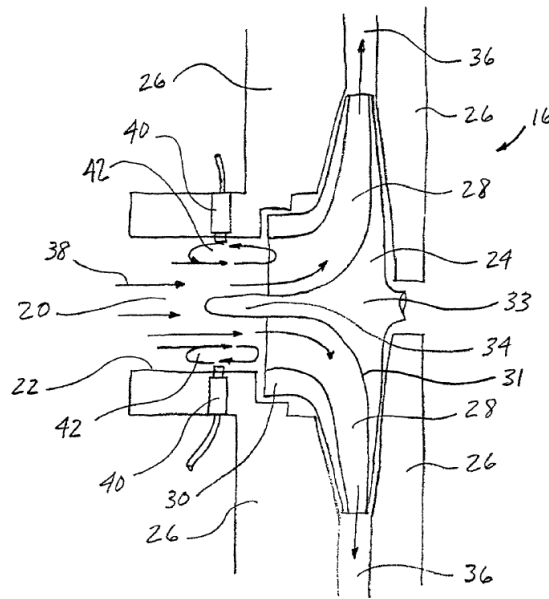


Figure 4.11: Dynamic surge detection based on inlet measurements [41]

For wet gas, this may be relevant because of the liquid accumulation that tends to occur in the inlet region at low flow. The amount of accumulated liquid depends on design, fluid properties and operating point, and the liquid accumulation does not necessarily mean that surge is imminent. The question that needs to be addressed then is what consequences this liquid accumulation has on the compressor performance within normal operating range. If it is significant, there exist an incentive for monitoring the conditions by the impeller entrance.

Garcia et al. [23] suggest a dynamic surge detection method based on statistical tools. Singular Spectrum Analysis was employed on static inlet and outlet pressure sensors. This is essentially a method of enhancing the pressure fluctuations associated with surge inception. It was found to give a very clear indication between stable and unstable signals, thereby alerting the user of surge.

4.5 Slug

Slug flow is a unique challenge for wet gas compressors, since traditional gas processing always include separators that protects the compressor from inlet instabilities. In gas processing literature it is common to distinguish between *hydrodynamic slugging* and *terrain slugging* as illustrated in Figure 4.12 and Figure 4.13. The former corresponds to the phenomenon explained in the introduction, which means that it can be predicted using a flow pattern map. Terrain slugs on the other hand, are formed if liquids accumulate in lower-lying regions and forms a blockade for the gas. Pressure then builds up and eventually blows the liquid plug through the pipeline.

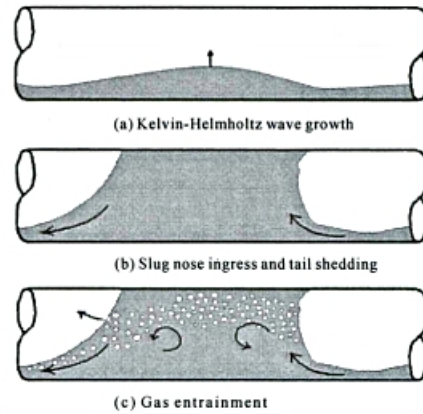


Figure 4.12: Formation of hydrodynamic slug [4].

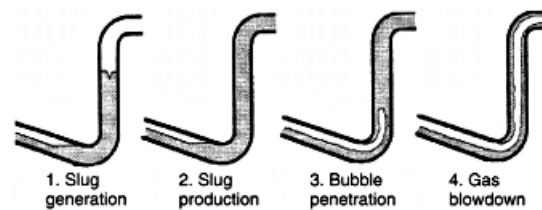


Figure 4.13: Formation of terrain slug [42].

Neither of these phenomena are expected to occur during normal wet gas operating conditions which includes very high superficial gas velocities. Encountering slug is however a risk towards the end of fields lifetime when the flow from reservoirs are decreased and become more liquid dominated. It is also a risk during start-ups, since the gravitational forces has been allowed to work unobstructed by the flow drag and made the phases separate vertically.

The compressor station at Gullfaks used a mixer unit which ensured homogeneous flow and provided some protection against GMF fluctuations. With respect to the flow field at the compressor inlet, the author uses the term "slug" to express a rapid decrease in GMF, which comes as a consequence of some sort of slug flow in the upstream pipelines. Exposing the compressor directly to a pipeline where more or less immediate transitions from 100-0% GMF can occur is not within the frame of current research, and the test rig used in this thesis is not built for it. It should be taken into account that no research relating slug flow to compressor operation is found in open literature. The overview given in this section is therefore based on evaluating the known flow mechanisms and reviewing literature that covers analogous phenomena.

Drive response

Perhaps the most obvious challenge is that increase in GMF implies an increase in compressor load. This is especially of concern if the drive is operating at peak capacity; a rapid increase in GMF will rapidly increase the load, thus decelerating

the compressor and render it unable to deliver the required pressure. In other words, the compressor will be forced towards surge.

Axial load

The axial thrust acting on the rotor of a single stage centrifugal compressor is a result of the non-uniform pressure distribution in the impeller channel, the differential pressure acting on the faces of the balance piston and momentum variation in the process flow [6]. The axial thrust related to momentum variation is the component of most interest and is illustrated in Figure 4.14. In steady state operation it is simply proportional to the mass flow rate:

$$F_T = \dot{m}v_{ax,in} - \dot{m}v_{ax,out} \quad (4.4)$$

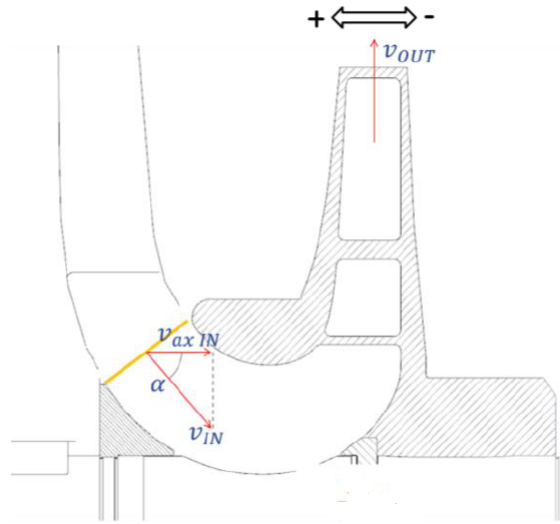


Figure 4.14: Variation of momentum in impeller [6].

Slug flow is characterized by large fluctuations in GMF, and therefore also mass flow. Given the high velocity that compressors operate at, the result will be large amplitude oscillations that may cause vibration in the axial direction.

Aerodynamic instabilities

Hydrodynamic slug flow is intrinsically unstable because of its local phase fluctuation which leads to constant variations in pressure, density, velocity and momentum flux. It is therefore considered by researchers to be the most complicated phenomenon among all the internal two-phase flows in a pipeline [1]. Injecting a slug with irregular pressure and flow profiles through the compressor at, or near an unstable operating point may cause the compressor to operate less steadily.

Most studies that focus on the effect of unsteady inlet flow conditions on the surge margin are related to automotive turbocharger applications. These centrifugal compressors operate at highly unsteady inlet conditions because they need to respond to the intake and exhaust manifolds of the internal combustion engine.

Marelli et al. used a pulsator and found unsteady flow performance which deviated significantly from steady flow conditions in the surge area. In particular, the mass flow rate plotted against the pressure ratio resulted in a hysteresis loop surrounding the steady state curve. In addition, the fluctuation of the surge line spanned over a large area, especially at high speed and high pulsation frequency. These tests were conducted at compressors operating at very high speed (80-140 krpm), with pulsation frequencies from 45-80 Hz. This is different from typical subsea compressor conditions. Still, if there are hydrodynamic slugs in the flowlines upstream of a compressor, the ratio between compressor speed and pulsation frequency can be expected to be of a similar order.

Pipeline instabilities

A known effect of the mentioned variations associated with hydrodynamic slug flow is that it can cause resonance, and subsequent fatigue in piping systems if the excitation force frequency is close to the natural frequency of the pipe [59]. While pipeline resonance is somewhat on the outside of the frame of this thesis, it is considered to be relevant because the compressors outlet pressure is highly dependent on GMF. The periodic forces associated with slug flow will therefore increase in magnitude through the compressor, meaning that the pipeline downstream of the compressor is a high risk zone for vibration.

This is especially true for subsea equipment, which are designed to be easily retrievable. Piping elements therefore needs to be flexible and simply stiffening the pipes in compensation will not always be an option.

Fluid hammer

A fluid hammer is a pressure wave that can occur when a fluid is force to stop or change its direction in a very short amount of time. It is of most concern in liquid pipelines where valves are positioned downstream of a pipeline system. Rapidly shutting the valve will lead to a pressure wave that has a propagation speed that exceeds the wave speed, thereby creating a shock wave.

The impeller is susceptible to such a phenomenon since it consist of sharp curves that forces the liquid to change direction in a very short time. If shock waves are formed inside an impeller channel, these could damage the impeller. Whether significant shocks can be created, or if the impeller curvature will make it improbable is not known.

4.6 Wet gas rotor stability

In recent years a few articles have been released where rotor stability during wet conditions have been reported. A review of these are given in this section.

Radial vibration levels were monitored during the K-lab tests in 2005. The main finding by Brenne et al. [11] was that machine vibrations were not significantly affected by the hydrocarbon condensate. Interestingly, a 0.5Xrev subsynchronous vibration appeared at high liquid loads. This was attributed to liquids entrained in

the seal areas at the impeller eye and balance piston, causing some type of rotor instability. These results refer to steady state tests however. Slug flow was not simulated.

More recently (2014), Vannani et al. [62] performed a test campaign on a single stage centrifugal compressor operating with an air/water mixture, where the goal was to evaluate the effect wet gas has on rotordynamics. The shaft behaviour was investigated through a flux controlled magnetic bearing. These types of bearings are able to excite the shaft through a rotating force. Furthermore, the force can be controlled in amplitude and frequency, and is therefore ideal for analyzing the rotor's response. A thrust bearing with on-board strain gauge load cells allowed for monitoring of axial thrust during the test.

The results showed that the 1X frequency was not heavily affected by the presence of liquid, and the general vibration level, measured by displacement probes did not change significantly from the dry case. A slow increase was observed with decreasing GMF, although far below the alarm level in all cases, as seen in Figure 4.15. The vibration appeared as a widespread noise, both sub and super-synchronous. The tests also showed that the presence of liquid had a mildly stabilizing effect on the logarithmic decrement of the rotor.

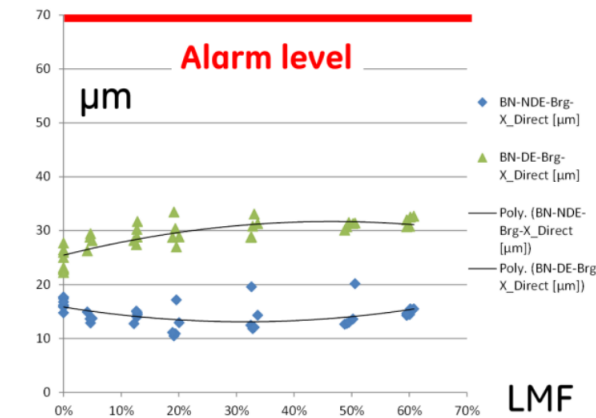


Figure 4.15: Vibration trend at increasing liquid content[62].

Curiously, the effect on axial load was not reported in this article. However, Ransom et al. [47] performed tests on a two stage centrifugal compressor also operating with an air/water mixture. It was concluded that wet gas operation had a significant impact on axial thrust. Also, a low frequency axial vibration was documented.

4.7 Summary

Chapter 4 gives a review of the nature of compressor flow instabilities, predicts the expected compressor behaviour during transient GMF scenarios and gives a literature review on previous experiences of rotordynamics during wet gas conditions. Important statements include:

- The impeller and the diffuser can both experience rotating stall, with excitation frequency that depends on compressor speed and number of stall cells.
- Impeller stall gives a relatively harmonic signal at frequencies between 50% and 80%, while diffuser stall gives less harmonic signals at frequencies in the range of 6 percent to 33 percent. There is normally a hysteresis zone associated with diffuser stall, but not with impeller stall. Impeller abrupt stall occurs
- The pulsations characteristics of compressor surge depends on the plenum geometry as well as the speed of sound. Greitzer's model predict a more direct transition into surge when GMF is decreased.
- Possible challenges related to slug include drive response, flow instabilities (leading to vibration in both axial and lateral direction), fluid hammer and pipeline resonance.
- Alternative methods of detecting transient behaviour are reviewed in the form of dynamic surge detection systems.
- Previous experience suggest that rotordynamics is not heavily affected by the presence of liquid, but a mild increase in the vibration level has been observed by multiple researchers, as well as a significant increase in axial load.

This concludes the theory and literature review. Chapter 5 presents and discussed the results that are obtained by the author during his test campaign.

EXPERIMENTAL CAMPAIGN

This chapter reports the results obtained from the test campaign performed by the author in cooperation with research advisers. A description of the test rig is given, before the test procedure and results are presented. The test campaign is divided into three parts:

- Steady state profile, where noise and attenuation is discussed.
- Left limit investigation, where the compressors behaviour in the surge area is explored.
- Slug tests, where GMF is rapidly decreased while the compressor is operating around the surge limit.

5.1 Test rig

Results presented are based on tests conducted at the wet gas compressor rig at Norwegian University of Science and Technology's. It was first installed in 2006, but has received several minor modifications since to take account of increased knowledge about wet compression mechanisms. A complete redesign of the compressor and inlet section was implemented in 2013. The rig was constructed in collaboration with industry partners and is used for both academic purposes and industry related research.

Specifications

The compressor is a low pressure ratio one-stage compressor that operates on air and water. Ambient air is drawn into the compressor through a piping system, and a water injection system is installed approximately one meter upstream of the compressor inlet. The injection system consists of 16 nozzles mounted circumferentially and a pump is used to regulate the water pressure.

A cross-section of the compressor is shown in Figure 5.1. It is equipped with a vaneless diffuser and a symmetrical circular volute that collects the fluid and delivers it to the outlet pipe. The diffuser is straight-walled in its standard configuration,

but it can be trimmed in order to adjust performance. Multiple impeller configurations are also possible. For this project, the compressor was configured with a contracted diffuser and a backswept and shrouded impeller with splitter blades. The volute design is adjusted for wet gas operation by decreasing the cross-sectional area, thereby compensating for increased fluid density.

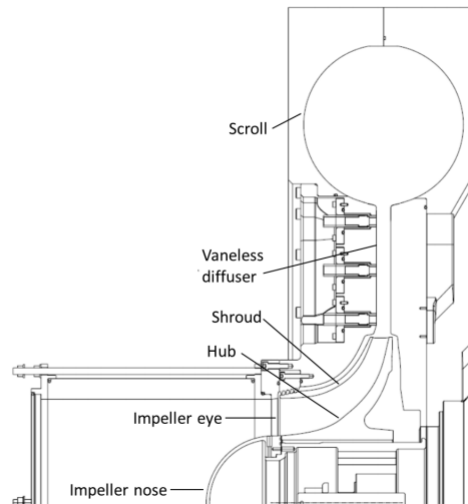


Figure 5.1: Cross-section of the centrifugal compressor at test facility [20].

The compressor is driven by a 450kW electric motor and is equipped with a variable speed drive (VSD). Compressor inlet and outlet pressures are controlled by hydraulically actuated V-ball valves. This system provides a fast valve response with high precision. Additional performance regulation can be achieved by equipping variable inlet guide vanes (VIGVs) to induce prewhirl. An overview of the rig components is shown in Figure 5.2.

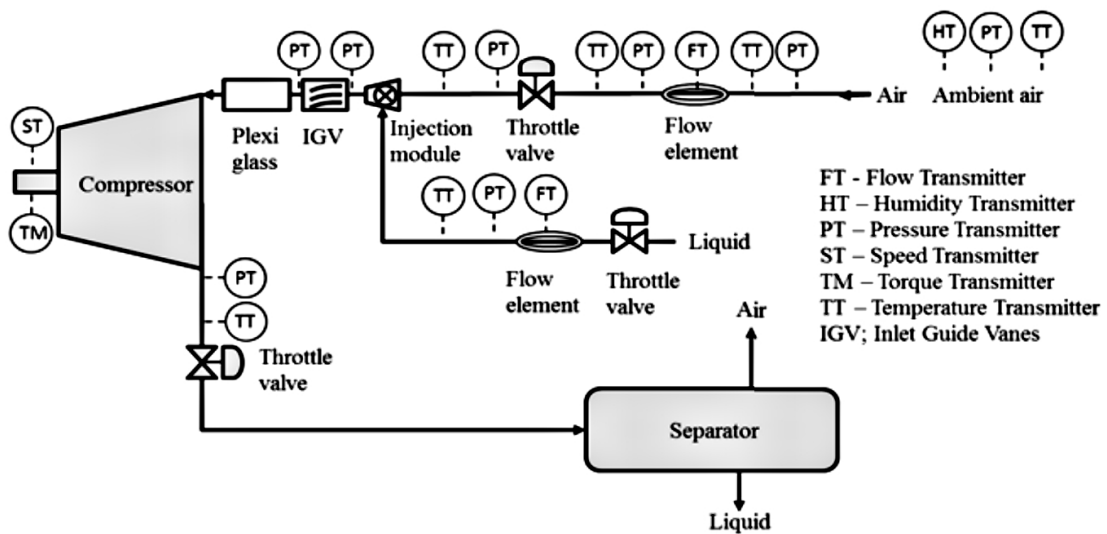


Figure 5.2: Test rig PID.

Multiphase flow measurements inside the compressor channels is very difficult.

A signature feature of the test rig is the large degree of visual access, enabling visual inspection of flow phenomena. This is achieved by using sections of transparent thermoplastic in the pipe inlet, in the diffuser shroud wall and in the volute.

Instrumentation

The acquisition system for the test rig is the National Instruments PXI solution, which permits synchronous sampling up to 20kHz. Instrumentation is in accordance with ASME PTC-10 standards for compressors and exhausters [2]. Static pressure sensors are placed at the inlet, upstream of the injection module, and at the outlet. An orifice plate is installed at the inlet pipe, and is used to determine the flow rate at the compressor inlet. Temperature sensors are placed at both inlet and discharge.

Figure 5.3 displays the transmitters located in the diffuser. The prime interest for the experiments in this thesis is the three high-responsive pressure sensors that are flush-mounted at the shroud side of the bottom part of the diffuser. These are piezoelectric dynamic pressure sensors with a natural frequency of 250kHz.

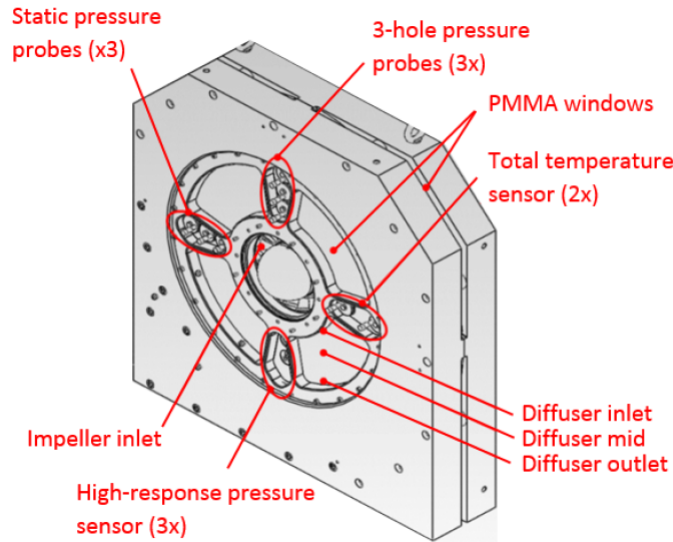


Figure 5.3: Compressor block with diffuser instruments.

The rotor of the machine is very rigid, both because the compressor is a single stage machine, and because it is mounted using ceramic ball bearings. Ceramic ball bearings have a higher stiffness coefficient than traditional steel bearings and are also characterized by very high damping coefficients. Vibration probes are therefore not considered to be useful for monitoring radial forces.

A complete evaluation of the radial excitations would require flux controlled magnetic bearings, and a thrust bearing with on-board strain gauge load cells would be needed for the axial forces to be measured. The stability evaluation is therefore limited to dynamic pressure readings in the diffuser. In addition, the rigs static pressure sensors are of high resolution and can be used to detect more global instabilities in the compressor system. The rotors natural frequency has been identified to be within the range of 6300-7400 rpm.

Compression system

The compression system of the test rig is illustrated by Figure 5.4.

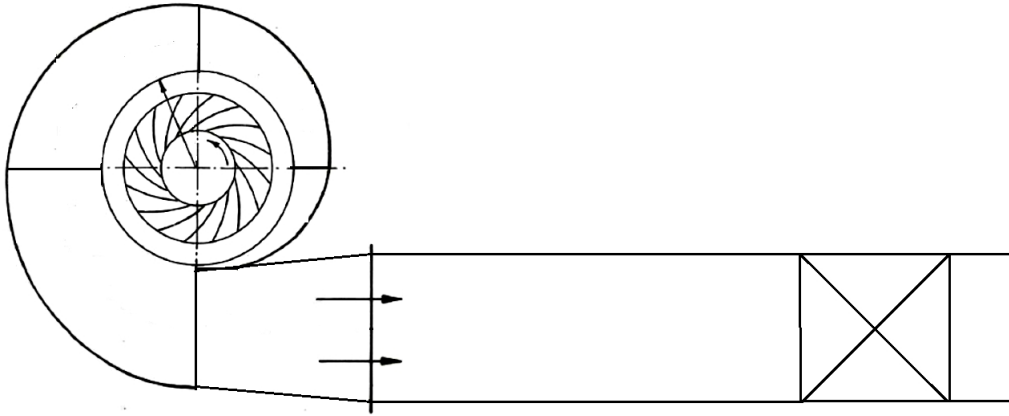


Figure 5.4: Test rig compression system.

It does not represent a perfect Helmholtz resonator, due to the outlet only consisting of a short pipe segment, and no clear boundary being present between the characteristic volume that produces the pressure oscillations and the plenum. This makes it difficult to accurately determine the natural frequency of the compression system. Still, an estimate was made in order to make identification of pressure pulsations easier when evaluating the test data. The boundary between the diffuser and the volute represents the boundary most closely resembling a resonator, and the calculations were based on assuming a resonator to be formed across this boundary. This resulted in an estimated Helmholtz frequency of 39 Hz for dry gas. Its dependency on GMF based on Wood's model for speed of sound is shown in Figure 5.5. The description of the procedure for obtaining this estimate is given in Appendix A.2.

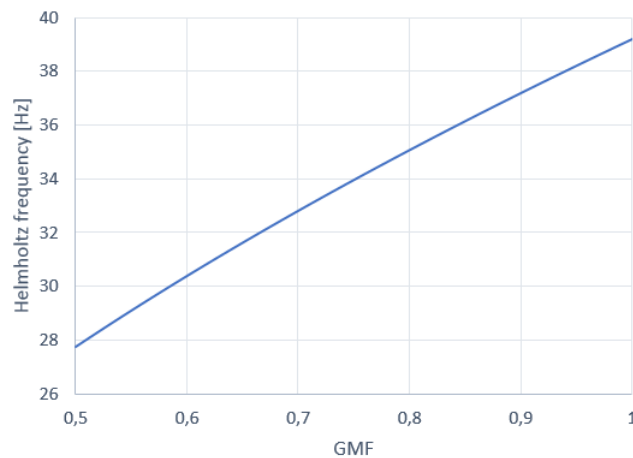


Figure 5.5: Estimated Helmholtz frequency of compression system.

5.2 Test matrices

In order to give an evaluation of the noise level and attenuation of the pressure pulsations within the compressor, a set of steady state-tests were devised and performed. These tests also forms a baseline for the transient tests and gives an indication of the compressors operating range. In Table 5.1, the test conditions are given. The tests are limited to one speed, but a relatively high GMF resolution is prioritized in order to avoid observing false GMF correlations. For each curve, six points are tested; from maximum flow to a set flow coefficient where the compressor has entered the surge region during dry conditions.

Table 5.1: Steady state test matrix.

Speed [rpm]	GMF			
9000	1.0	0.90	0.80	0.60

For the left limit tests the compressors mode of instability was found by ramping the outlet valve for a brief period. The flow rate was lowered until the compressor expressed flow and pressure instability. Due to a large amount of liquid being filled up in the inlet pipe, the wet gas test was limited to 90% GMF in order to avoid pressure buildup in the plexiglas window. The outlet valve was also ramped faster. The test procedure is documented by Table 5.2.

Table 5.2: Left limit test matrix.

Speed [rpm]	GMF	Valve opening	Hold time [s]	Ramp time [s]
9000	1.0	35-20%	5	15
9000	0.90	35-24%	5	5

In order to document the transient compressor response a number of slug tests with homogeneous water injection were carried out at the compressors point of peak pressure head ($\phi = 0.028$) and inside the surge region ($\phi = 0.024$). A slug test can be performed using either the main water control valve, or by manually opening one or two nozzles simultaneously while adjusting the water pump pressure. The latter option was found to give the most immediate flow transition and was therefore the method of choice in the performed tests (Table 5.3). These tests were limited to 60%GMF as it was difficult to go lower than this while at the same time avoiding significant backflow in the inlet pipe.

Table 5.3: Slug test matrix.

Speed [rpm]	Slug GMF	Flow coefficient
9000	0.90	0.028
9000	0.90	0.024
9000	0.80	0.028
9000	0.80	0.024
9000	0.60	0.028
9000	0.60	0.024

It was also of interest to see if a hydrodynamic slug could lead to instability in the compression system. Tests where multiple slugs were injected in sequence was therefore conducted. The slug duration was set to a short time in order to increase the chance of observing resonance with the Helmholtz frequency. The test conditions are given in Table 5.4.

Table 5.4: Slug sequence test matrix

Speed [rpm]	Slug GMF	Flow coefficient	Slug duration [s]	Number of slugs
9000	0.80	0.024	1	5
9000	0.80	0.028	1	5
9000	0.80	0.048	1	5

5.3 Results

Obtained results are presented in the same order as the test matrices, starting with the steady state results. The spectrum analysis is performed on the basis of FFT, both because this is proven and widespread within condition monitoring of turbomachinery, and because the software employed in the data processing, National Instruments Diadem, does not provide options for CWT. Hanning window is used in most of the spectra. A comment about window choice is given in Section 5.3.2.

5.3.1 Steady state

Figure 5.6 shows the characteristics of the compressor with pressure ratio on the ordinate. The general trend is that with a decrease in GMF, a slight increase in pressure ratio follows at low flow and around the best efficiency point ($\phi = 0.056$), while a decrease in range and pressure ratio follows at high flow. The surge area of the characteristics is identified to be at $\phi < 0.028$ for 100%GMF, and the extended surge margin for wet gas is indicated by the negative slope what continuous into the surge area.

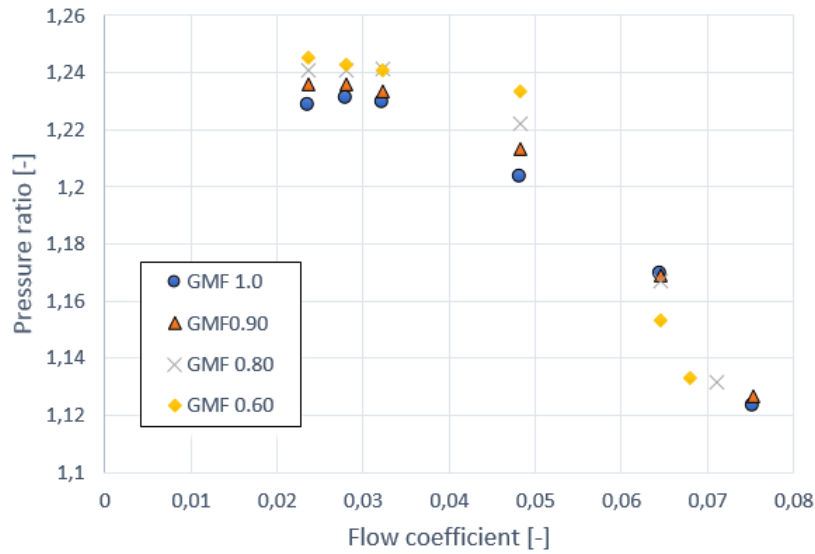


Figure 5.6: Compressor characteristics at 9000 rpm.

A Fourier Transform of the dynamic pressure signal at the impeller outlet at stable dry conditions is reported in Figure 5.7. A very periodic 1Xrev is visible at 150 Hz, with harmonics throughout the spectrum. This does not concur with the harmonic force that normally is exerted by an unbalanced rotor, suggesting that the transfer of force between the rotor and the compressors working fluid is not entirely linear. However, this force is insignificant, and because its spike is very narrow, it disappears when power spectral density is employed.

The impeller has 18 blades, leading to a blade pass frequency (BPF) at 2700 Hz. Because the impeller is designed with splitter blades of shorter length than the main blades, the pressure pulsations accompanying the jet-wake pattern has an additional component at 0.5XBPF. The rotors natural frequency is in the subsynchronous area of the spectrum (105-123 Hz), meaning that periodic forces with similar frequency may resonate.

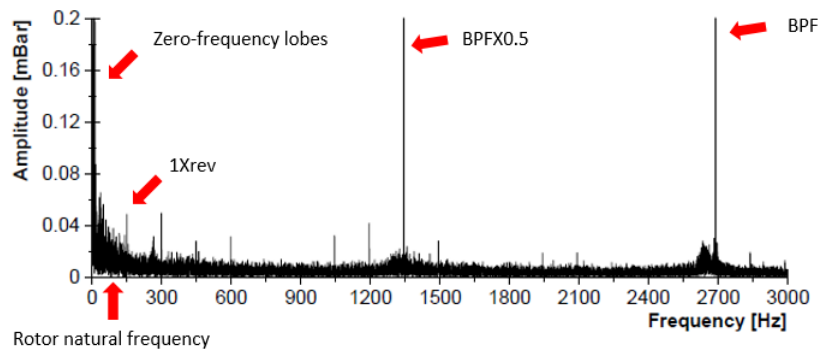


Figure 5.7: Fourier transform at $\phi=0.048$ and 100%GMF (Hanning window).

From 0-10 Hz there is a region where side lobes from a zero-frequency component dominate, making it difficult to identify weak signals that appears in this range. The reason for this component is found when analyzing the raw data, as in Figure 5.8.

Because of the piezoelectric sensors inability to measure static pressure, the average readings will instead oscillate around arbitrary values. If this value is not zero, the FFT will within a time window interpret this value as a periodic oscillation with a frequency approaching zero.

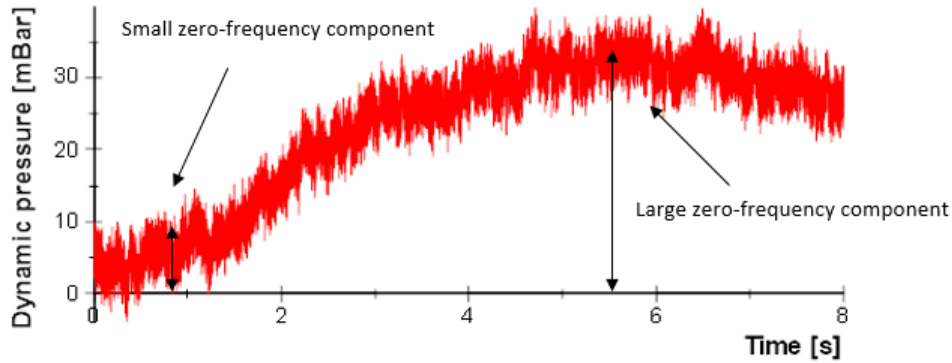


Figure 5.8: Magnitude of the zero-frequency component.

This is not an issue for the analysis presented in the following sections and this region will in most cases be filtered out. However, if the compressor was operated at low speed and slowly propagating rotating stall was developing in the diffuser, these lobes would delay the detection of it.

Figure 5.9 and Figure 5.10 displays the evolution of the spectrum when moving the compressors operating point along the characteristics for dry and wet gas. The points around the surge limit leads to the appearance of strong subsynchronous components, harmonics, spurs and a general increase in noise level across the spectrum.

As a side note for future research, it is pointed out that the relative magnitude between the BPF and the 0.5XBPF can be correlated with the angle of the inlet velocity diagram. At the best efficiency point (in this case at $\phi = 0.048$) these components should be equal in magnitude because the flow is guided equally on each side of the splitter blades. The pattern for wet gas is clearly different from that of dry gas. This is an indication of flow segregation as a result of the inducer curvature, leading to unequal liquid distribution between the impeller channels. Monitoring the BPF may therefore hold some valuable information if the wet gas flow regime in an impeller with splitter blades is investigated.

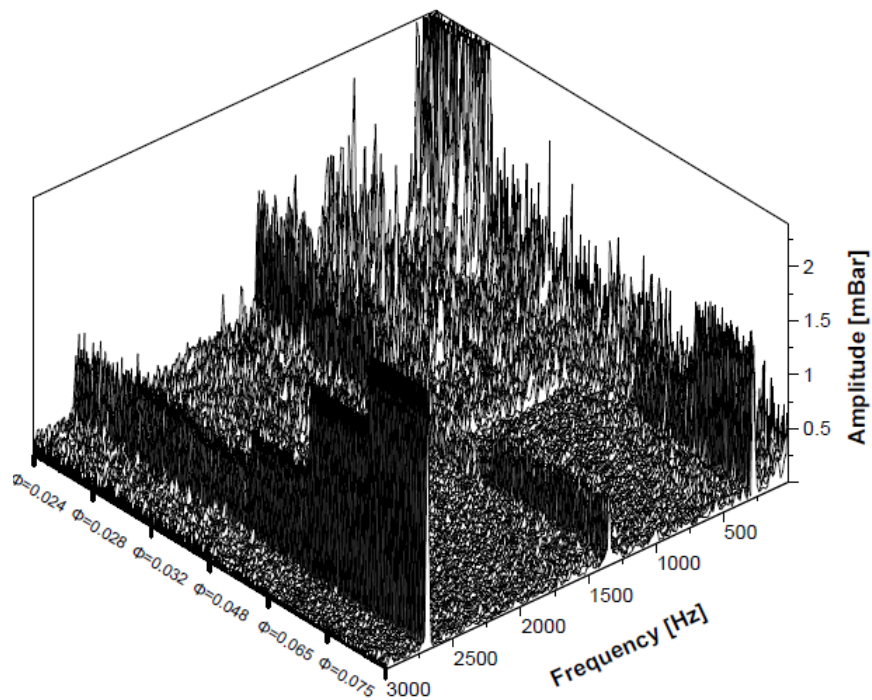


Figure 5.9: Steady state profile at compressor outlet pipe, 100%GMF (Hanning window).

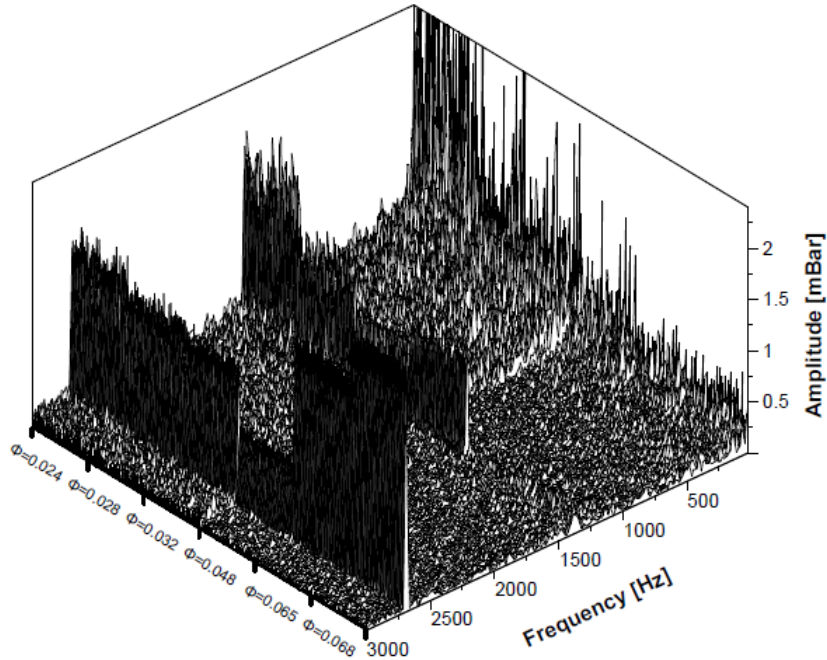


Figure 5.10: Steady state profile at compressor outlet pipe, 60%GMF (Hanning window).

In order to evaluate the liquids effect on the noise level in the diffuser a SINAD analysis was performed, and is reported in Figure 5.11. The blade pass frequency

was used for this purpose since its amplitude remains approximately constant when GMF is changed. The analyser was set to search for any signal occurring near 2700 Hz and consider all other signals as noise. In order to avoid other signals effecting the noise power, the analysis was restricted to tests performed at $\phi = 0.048$ and $\phi = 0.065$, where the BPF is of similar magnitude and subsynchronous components are not prominent.

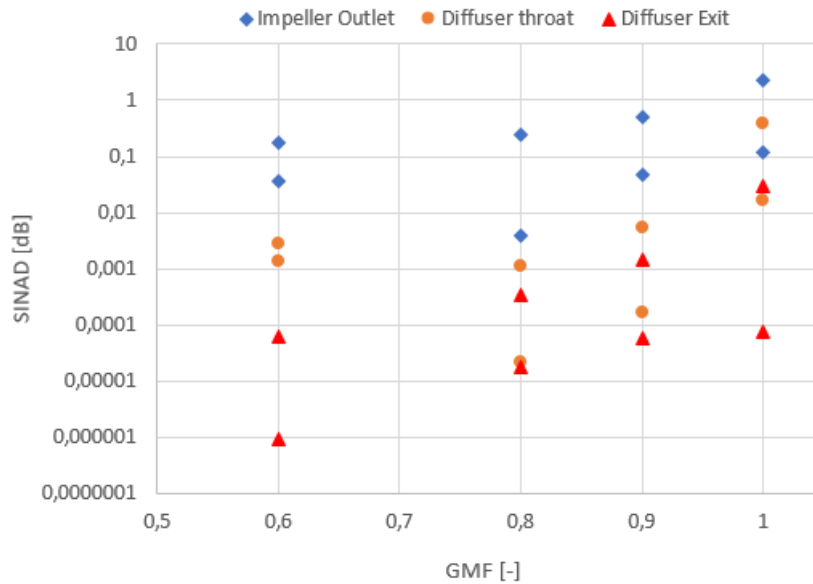


Figure 5.11: Signal quality at different GMF.

A weak positive slope is present, indicating an increase in noise level at reduced GMF. The effect is mild however, suggesting that shroud mounted dynamic pressure sensors are suitable for detecting aerodynamic transients in wet conditions. Figure 5.15 and Figure 5.13 shows PSD spectra obtained from the pressure sensor at the outlet pipe. In dry conditions, the BPF is still visible, but it is completely vanished in wet conditions and replaced by noise. This is a prime example of the increased attenuation of high frequency components during wet gas conditions.

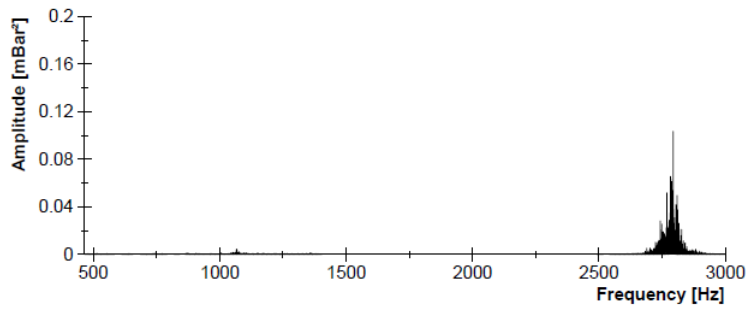


Figure 5.12: Steady state dynamic pressure profile at impeller outlet, 100%GMF

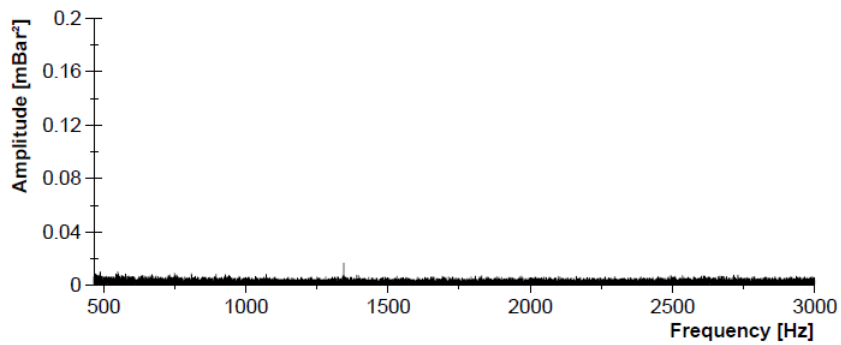


Figure 5.13: Steady state dynamic pressure profile at impeller outlet, 60%GMF.

5.3.2 Left Limit

This section summarize the results from the left limit tests, introducing with a comment about FFT settings.

Figure 5.14 shows the low frequency spectrum obtained from the pressure sensor at the impeller outlet during the left limit test for dry gas. Four different settings are compared:

- Rectangle window with raw signal analysis (amplitude peak)
- Hanning window with raw signal analysis (amplitude peak)
- Rectangle window with power spectral density
- Hanning window with power spectral density

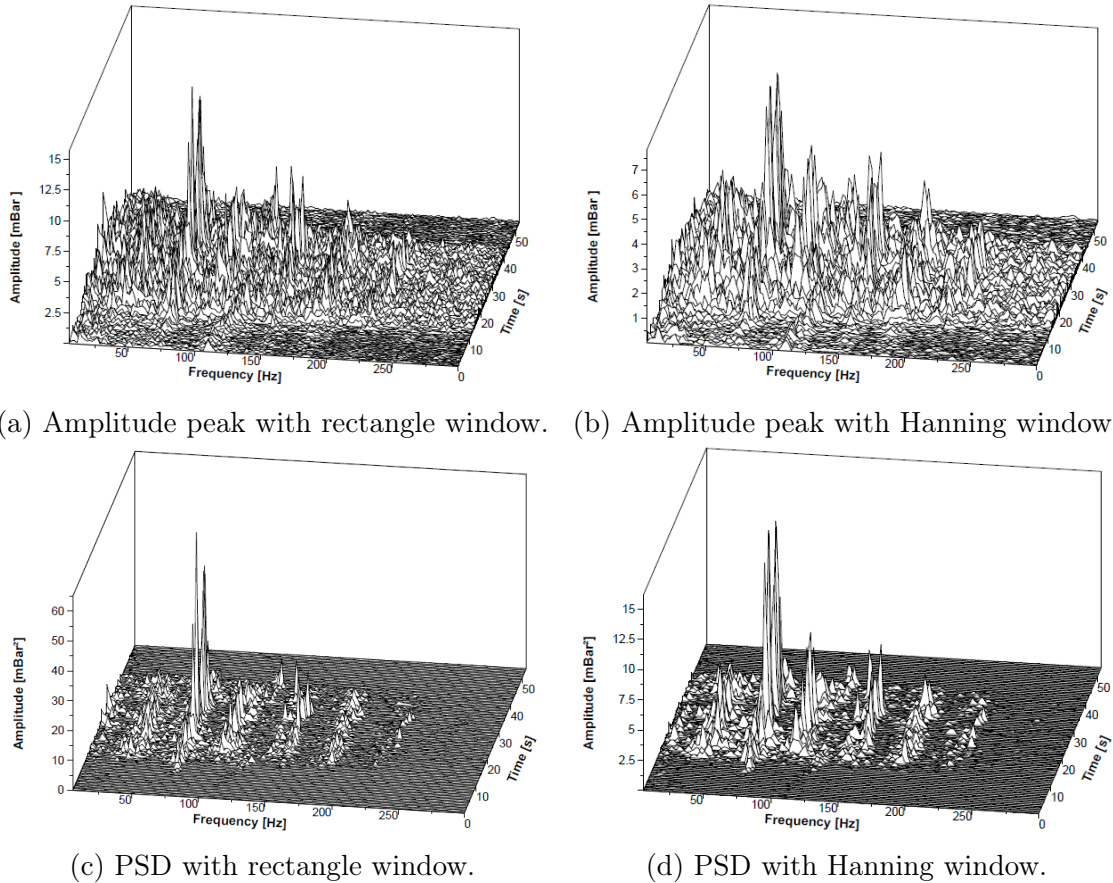


Figure 5.14: 100%GMF: Different analysis methods.

When amplitude peak is employed together with the rectangle window (5.14a), the large side lobes makes it difficult to identify the signals since there are multiple signals within close proximity of each other. The Hanning window is in this case not found to remove the lobes in an effective manner (5.14b), but on the other hand, the PSD is very effective in enhancing the signals. The selected method for spectrum analysis is therefore PSD with Hanning windowing (5.14b).

It can also be noticed that the maximum peak is halved when the Hanning window is applied to the amplitude peak spectrum and quartered when applied to the PSD. Being consistent in the analysis method is therefore critical when comparing different cases.

In order to identify the components, it is useful to refer to a contour map. Figure 5.15 shows the spectrum observed at dry conditions together with the flow and pressure ratio trend.

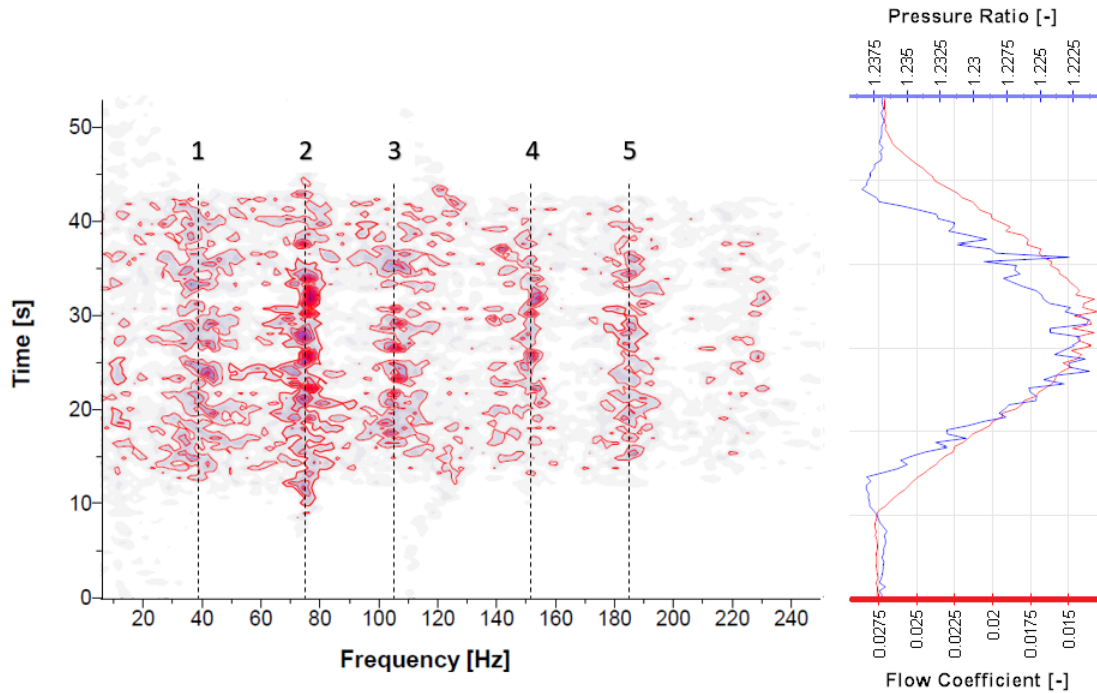


Figure 5.15: Left limit test 100%GMF: Impeller outlet.

The dominating component is identified at 75 Hz (2), equivalent of $0.5X_{rev}$, together with its harmonic at approximately 150 Hz (4). This component clearly appears before the other ones and its effect on the system stability becomes apparent after 34 seconds, when its diminishment leads to a large drop in the pressure ratio. This component has a frequency that is typical of progressive impeller rotating stall, and the readings from the diffuser outlet (Figure 5.16) confirms that the fluctuations originate from the impeller since the amplitude is reduced. Another indication of impeller stall is that there is no hysteresis - the point at which disappearance of the stall cell is observed coincide with the point at which it appears.

A component of low frequency (38 Hz, equivalent of $0.25X_{rev}$) appears at $\phi=0.025$, which falls within the range of both diffuser stall and expected Helmholtz frequency. Both of these are refuted as possible sources when investigating the spectrum at the diffuser outlet, where this component is barely visible. Since this component has a frequency half of that of the impeller rotating stall, this is likely a transformation of the stall pattern, where the cell alternates between two shapes when progressing across the impeller channels.

Component 3 and 5 may be mistaken for harmonics at first sight, but they are not integer multiples of any other components, which means that they most likely are spurs belonging to the 75 Hz-component.

It can also be observed that components 2-4 all gradually increase after inception, while component 1 and 5 does not. Since components 2-4 are in close proximity to the rotors natural frequency this growth may be attributed to resonance.

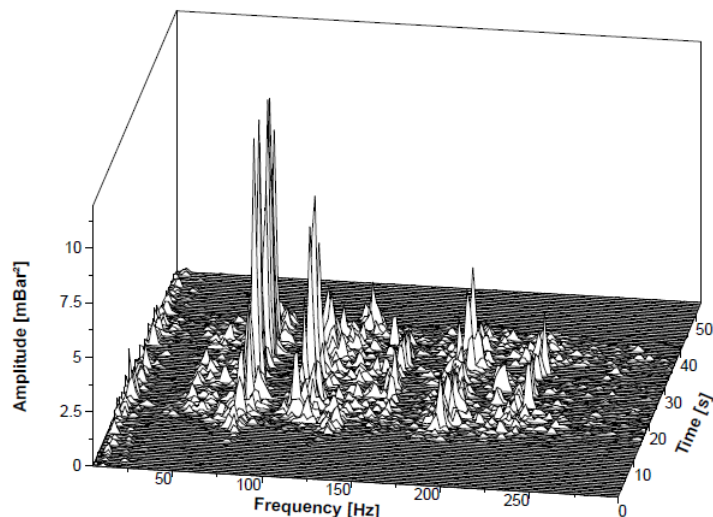


Figure 5.16: Left limit test 100%GMF: Diffuser outlet.

In order to evaluate the nature of the instability of the compression system, the pulsations of the outlet pressure is presented in Figure 5.17. The component that appears is a smeared version of the pressure pulsations from the rotating stall cell. This confirms that no mild surge occurs during this test. Instead, the encountered mode of instability is a transient to a new operating point in rotating stall at a reduced flow and pressure head, which is characteristic of systems with low plenum volumes.

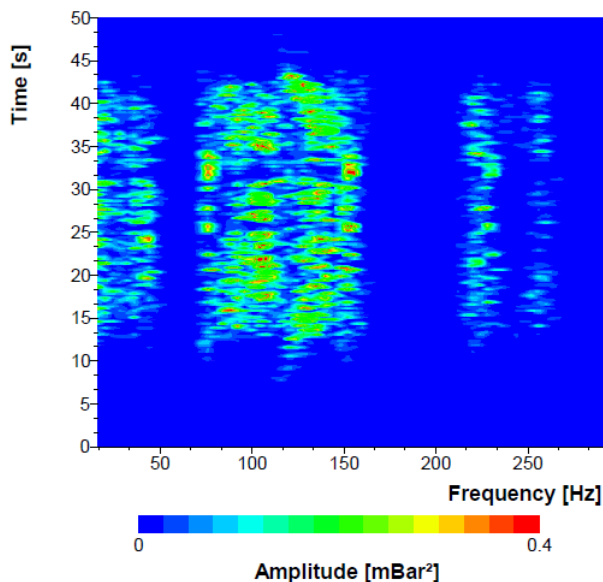


Figure 5.17: Left limit test 100%GMF: Outlet pipe.

Figure 5.18 and 5.19 shows the dynamic pressure measurements observed in the left limit test performed at wet conditions. The spectrum will not be analyzed in detail, since the components observed are similar as for dry conditions. A difference however, is that the 75 Hz-component gives no warning before causing compressor instability. This is addressed in the following paragraphs.

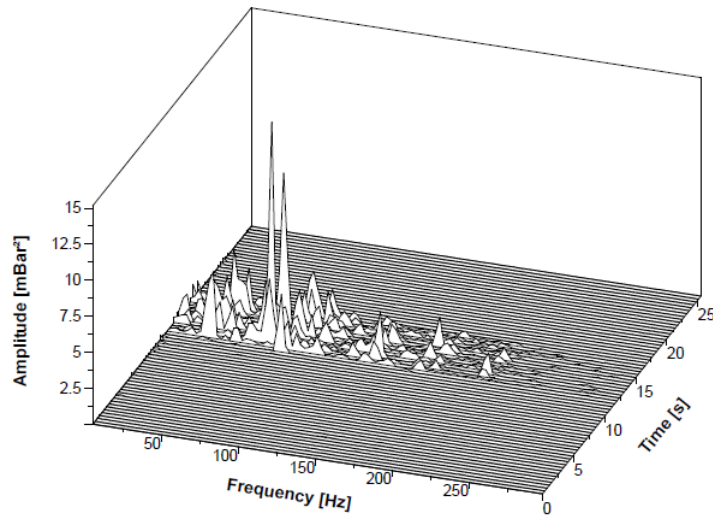


Figure 5.18: Left limit test 90%GMF: Impeller outlet.

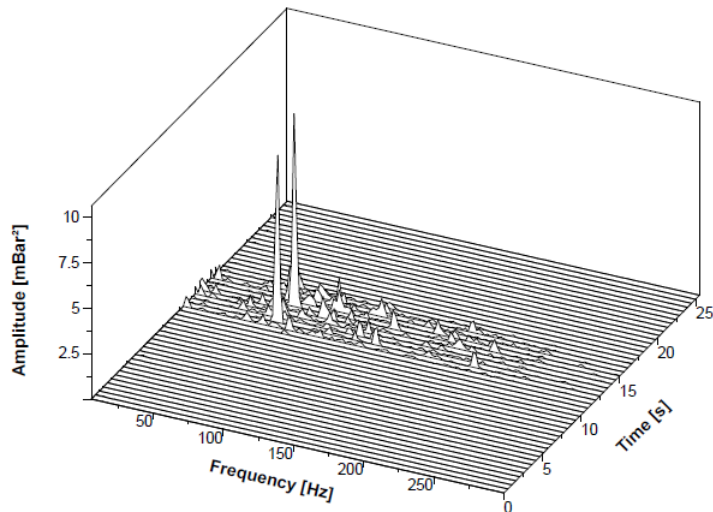


Figure 5.19: Left limit test 90%GMF: Diffuser outlet.

Because the test is performed by gradually closing the outlet valve while keeping the water supply constant, a reduction in calculated GMF follows, as documented by Figure 5.20. However, this is counteracted by a major backflow of liquid in the inlet pipe, as showed by three still frames in Figure 5.21, taken from a video of the test. The exact amount of water that is held up in the pipe is not possible to measure, but considering that the water supply at this test was set to 0.078 l/s, it is likely that this far outweighs the effect of reduced GMF due to reduced air flow rate. This indicates that the actual GMF inside the compressor is far higher than 0.90.

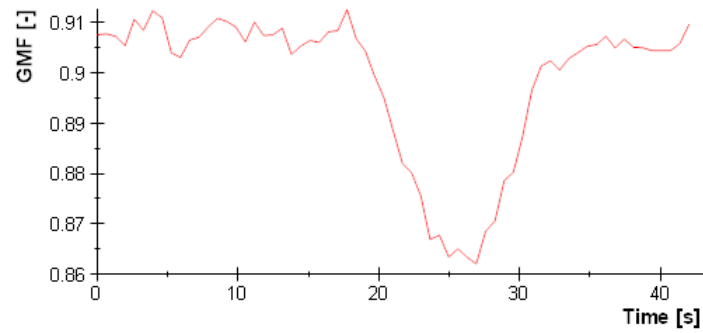


Figure 5.20: Calculated GMF during wet gas left limit test.

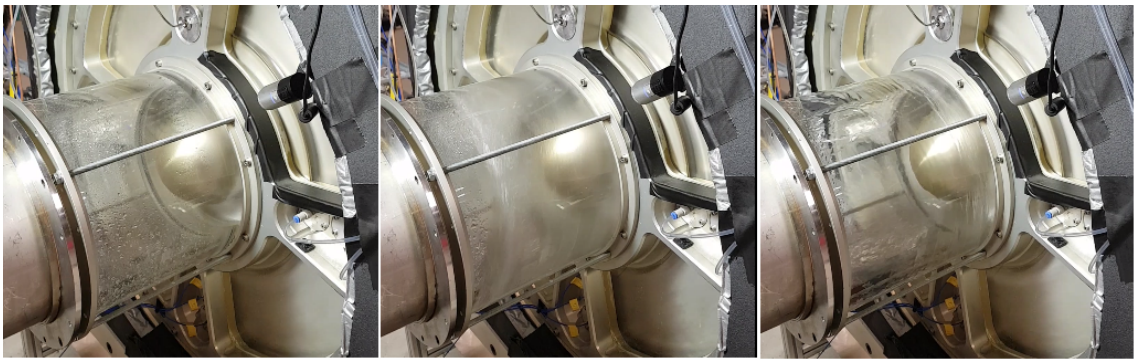


Figure 5.21: Backflow during wet gas left limit test.

The consequence of this is that upon closing the outlet valve, the compressor has two factors that increase the chance of stall cells appearing; reduction of air flow and increased GMF. The comparison of the compressors flow/pressure ratio trend during dry conditions (Figure 5.22) and wet conditions (Figure 5.23) confirms this, since the curve during wet gas conditions moves towards the dry gas curve. Figure 5.24 gives the wet gas curve superimposed onto the dry gas curve.

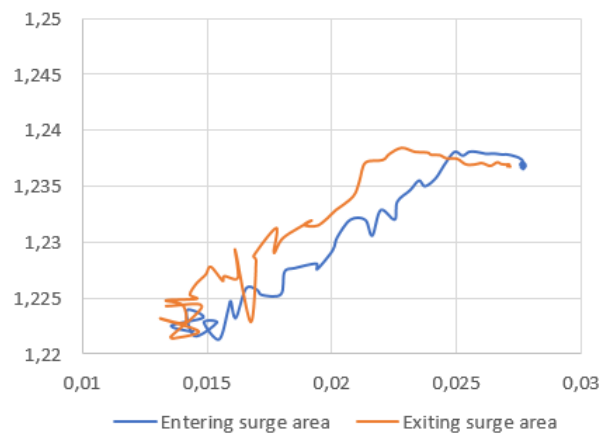


Figure 5.22: Compressor characteristics during left limit test at 100%GMF.

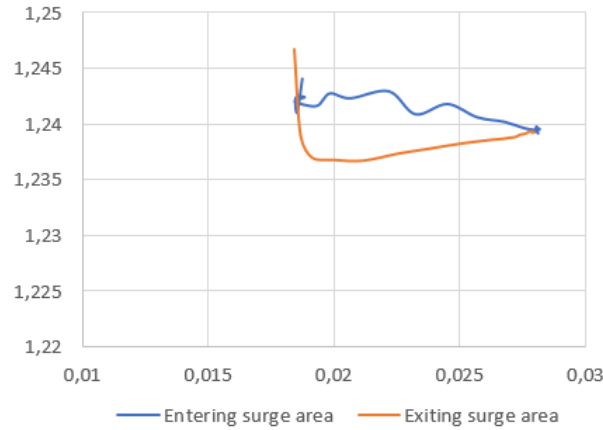


Figure 5.23: Compressor characteristics during left limit test at 90%GMF.

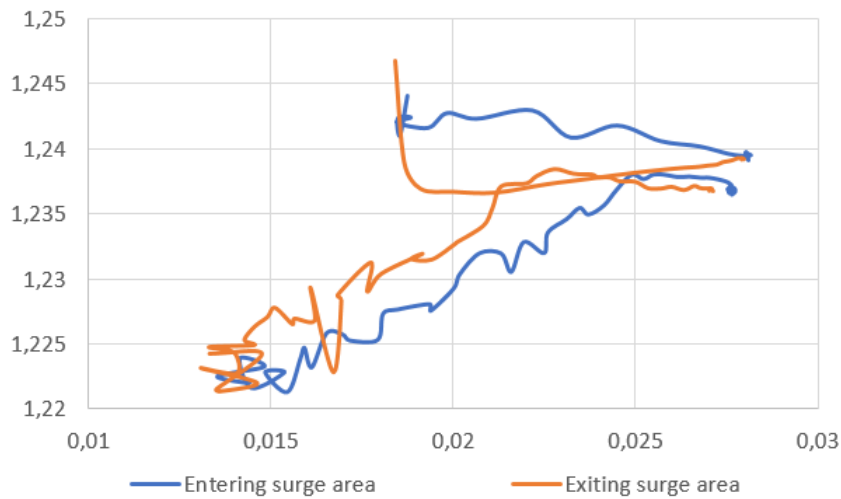


Figure 5.24: Superimposed compressor characteristics during left limit tests.

5.3.3 Slug

Since the slugs are transient by nature, it was of interest to evaluate the beneficial value of using windows designed to capture the response.

Figure 5.25 refers to a slug test at $\phi = 0.028$, where a comparison between the Hanning window and the exponential window is given. The transient that is captured and damped by the exponential window relates to the increased momentum of the flow that exits the impeller, resulting in a response signal just above the zero-frequency limit. This is not of interest when analyzing the pressure pulsations in the diffuser since it is too far away from the rotors natural frequency to lead to any vibration. Additionally, it results in very large side lobes that makes other sub-synchronous components impossible to identify. The Hanning window is therefore employed when analyzing the power spectral density in these tests. The spectra presented are focused on the low frequency area, both because this is where rotating stall cells are present, and because transient radial flow instabilities is expected

to make components appear around the rotors natural frequency if they are severe enough.

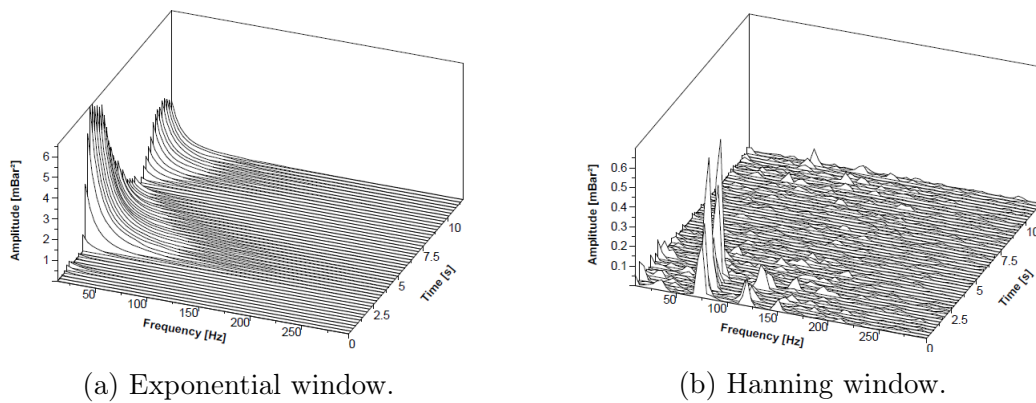


Figure 5.25: Window comparison during slug test.

Figure 5.26 to Figure 5.31 reports the results from six different slug tests performed at the surge limit $\phi = 0.28$ and in the surge area at $\phi = 0.24$. This is the region where rotating stall cells starts becoming significant. The dynamic pressure data is taken from the sensor by the impeller outlet.

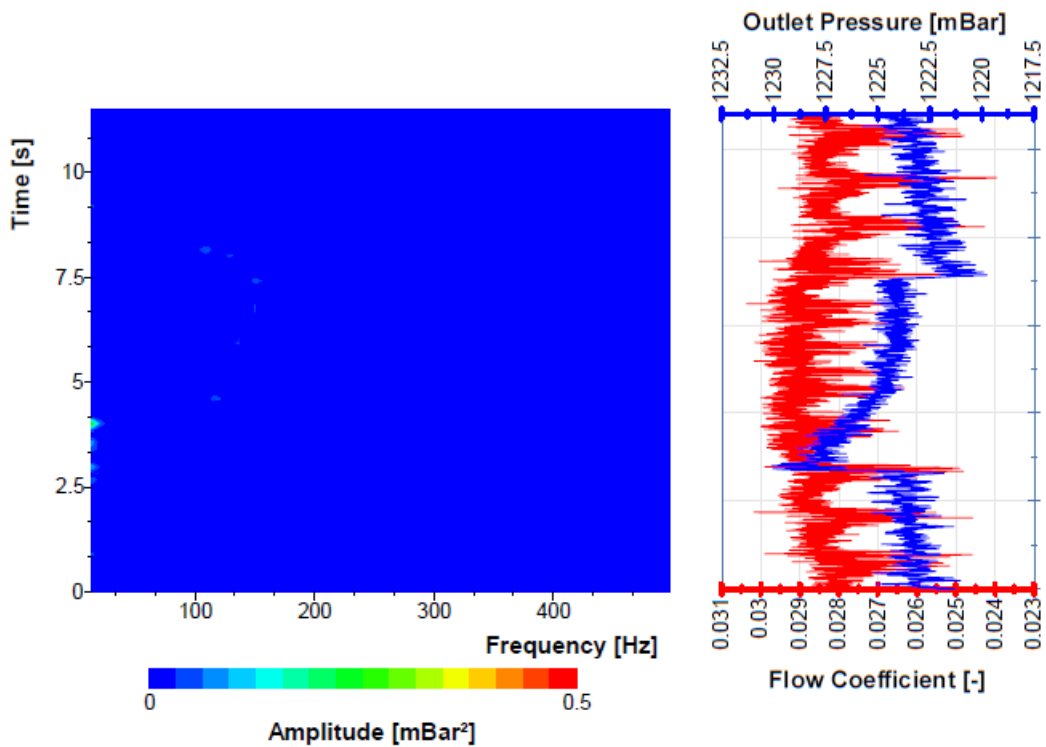
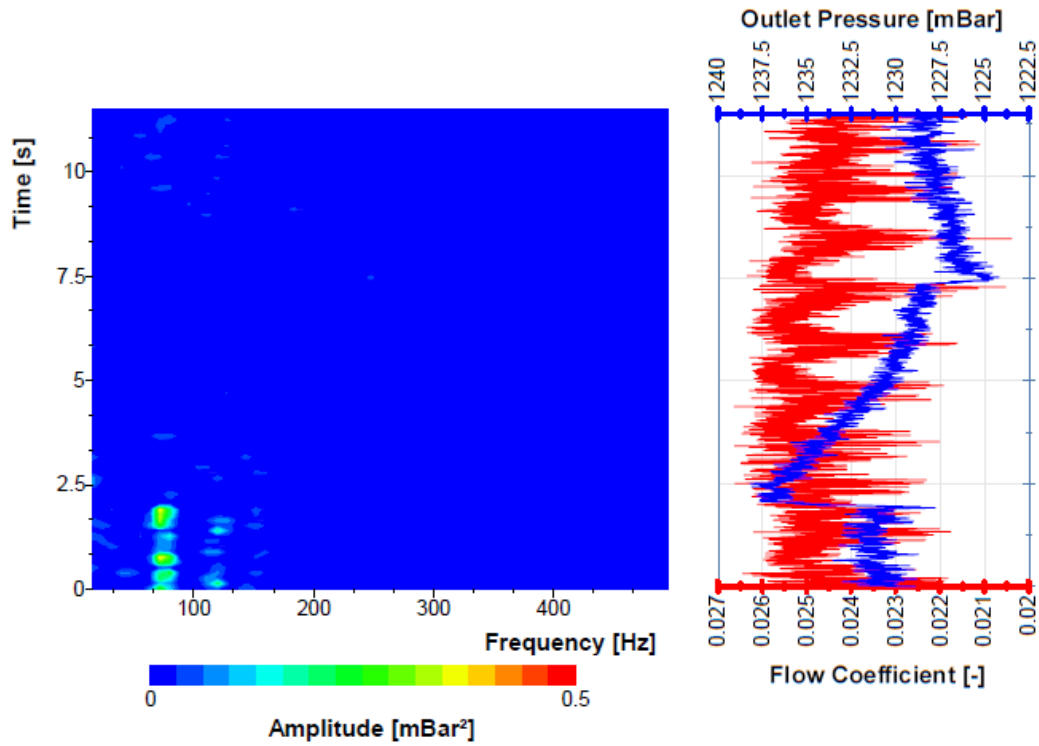
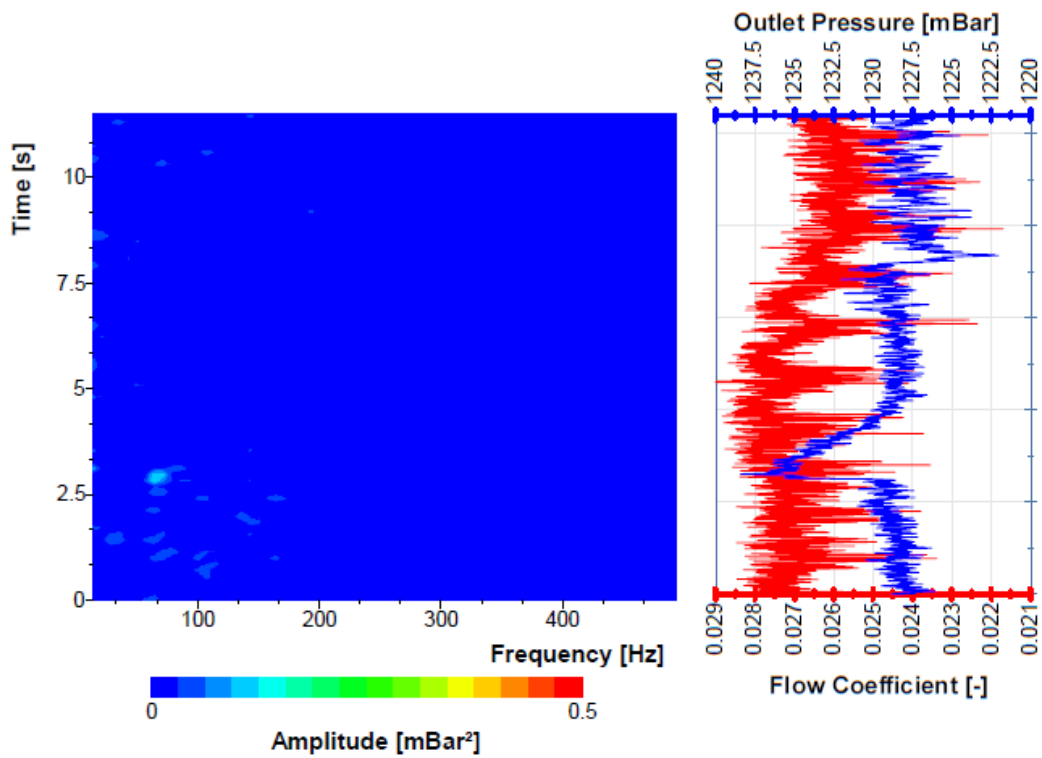
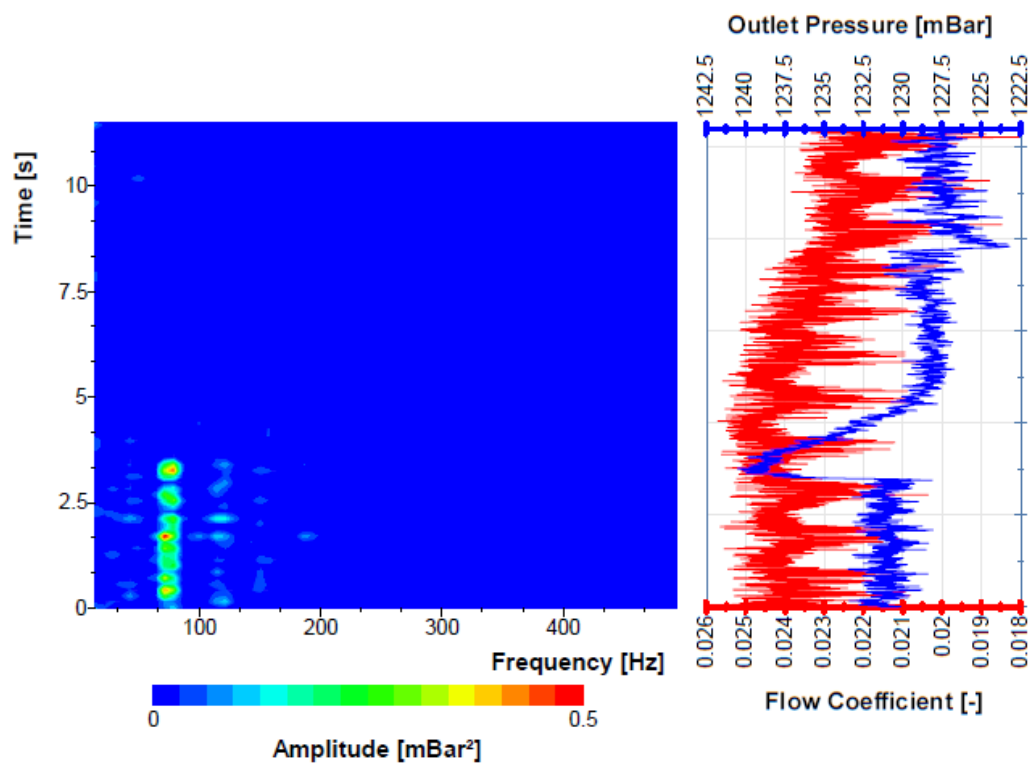
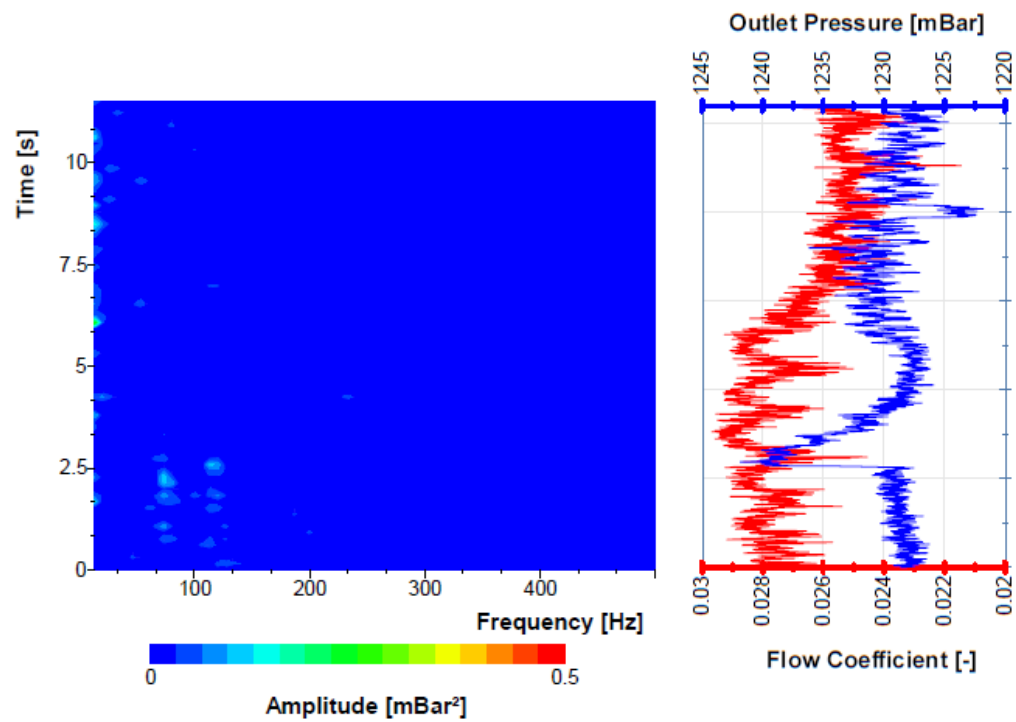


Figure 5.26: 90%GMF at $\phi = 0.28$

Figure 5.27: 90%GMF at $\phi = 0.24$ Figure 5.28: 80%GMF at $\phi = 0.28$

Figure 5.29: 80%GMF at $\phi = 0.24$ Figure 5.30: 100%GMF at $\phi = 0.28$

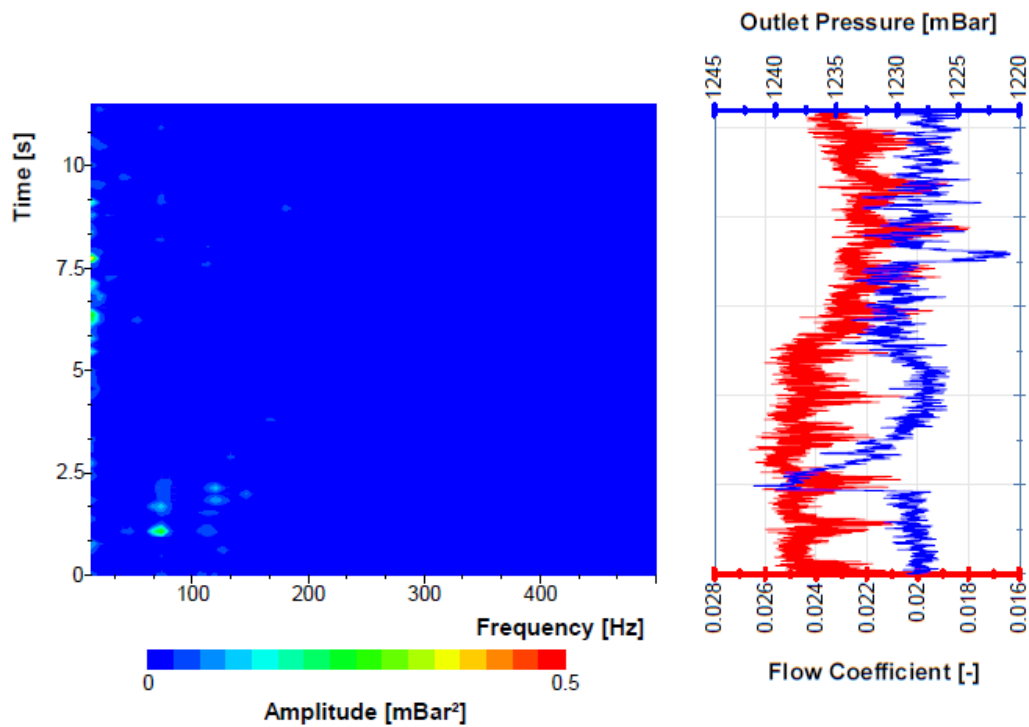


Figure 5.31: 100%GMF at $\phi = 0.24$

It is clear that the stalled regions quickly becomes re-energized and disappear when liquid is injected, even for low amounts of water. No excitation at the rotors natural frequency or other abnormalities are observed, suggesting that the slugs does not effect the rotor stability. The readings from the outlet pressure sensors in all cases shows a large peak with subsequent drop towards the steady state characteristic. This indicates a transition of the flow pattern through the diffuser and volute after the liquid has passed through the impeller. The moment when water supply is shut represents the dangerous point for the system stability, since the opposite is true and a large drop in outlet pressure occurs. Reappearance of stall cell after the slugs is delayed due to liquid being entrained around the impeller inlet after the water supply is closed.

Figure 5.32 refers to data from the outlet pressure sensor for a test where five slugs were injected in sequence.

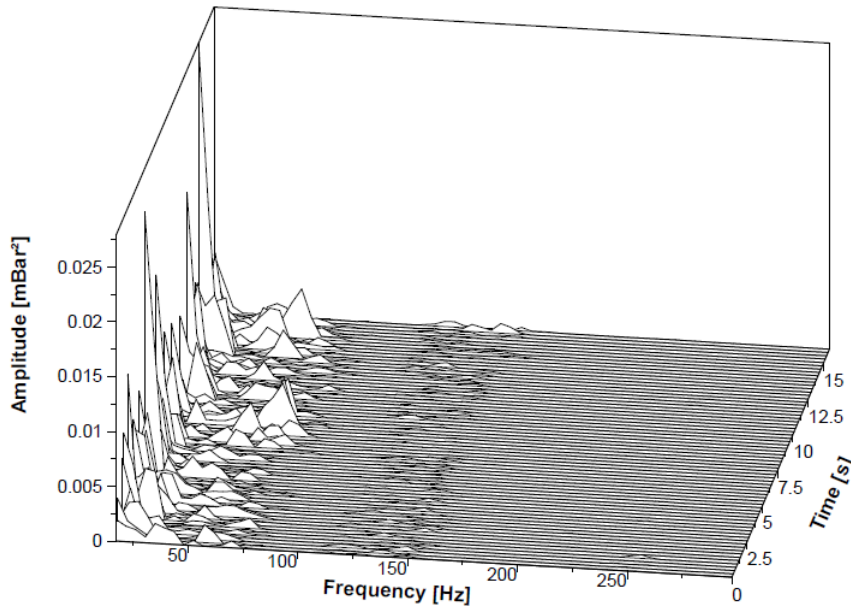


Figure 5.32: Outlet pressure during sequential slug injection at $\phi = 0.034$ with 80%GMF.

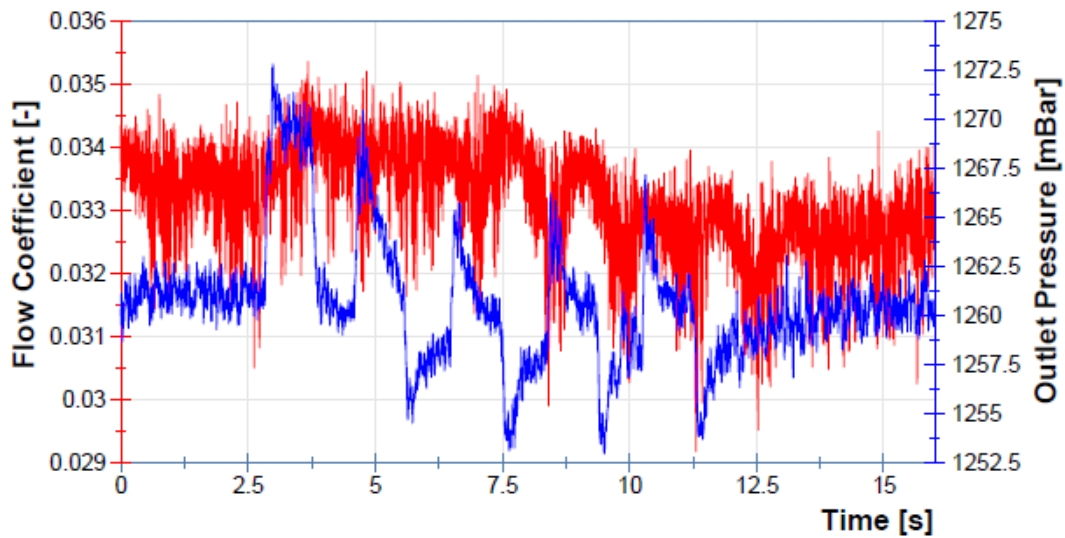


Figure 5.33: Pressure and flow during sequential slug injection at $\phi = 0.034$ with 80%GMF.

No indication of system instability is present, indicating that the systems natural frequency is far higher than the slug frequency. Only one of the tests are presented here because all tests gave similar results. It was chosen not to further pursue these kind of tests because it was unlikely that the slugs could induce oscillations at a frequency high enough to create system instability.

The outlet pressure and flow rate trend in Figure 5.33 is interesting because it shows a clear performance deterioration after the injection of the second slug, implying that the rapid change of flow pattern leads to a higher degree of interaction between the phases and increased friction losses through the compressor.

CONCLUSION

This thesis presents results of tests performed on a wet gas centrifugal compressor operating under transient conditions in the surge area. The main tool for detecting the transients is spectrum analysis, based on a time-frequency transformation performed by the Fast Fourier Transform. Analysis is primarily based on measurements from dynamic pressure sensors in the diffuser shroud wall. A thorough literature review of compressor flow dynamics, vibration, spectrum analysis and compressor instabilities has been given as this was deemed necessary in order to evaluate the data in a satisfactory manner.

The SINAD analysis performed at steady state documents a mildly decreased signal quality. This effect is attributed to the large acoustic impedance difference between the phases, leading to chaotic reflection of the pressure waves that intercept with dispersed liquid droplets in the diffuser.

The Hanning window together with power spectral density is found to give the best visualization of subsynchronous components; the strong components were enhanced, and sidelobes were damped. For analysis of slug tests the windows that are designed to capture transients, such as the exponential window, does not serve any purpose when evaluating dynamic pressure data because it only captures the momentum of the liquid slug flowing out of the impeller. On the other hand, this window is expected to very suitable if the data comes from sensors that monitor the rotor stability directly, since these sensors will not be disturbed directly by the change of flow regime.

The results from the left limit tests are in agreement with previous researchers who have reported an extended surge margin. Multiple subsynchronous periodic forces are observed, with a peak at 75 Hz identified as the main component and belonging to a rotating stall cell in the impeller. The same subsynchronous peaks are observed for dry and wet gas. In the wet gas test a more abrupt instability onset was experienced. The significant backflow that was visible in the inlet pipe suggested that this was because the real GMF in the compressor dropped quickly when shutting the outlet valve. Consequently, there are two destabilizing factors present when moving the compressor towards surge; decrease in flow rate and increase of GMF. This shows that it is critical for compressor operators to be aware of the liquid formation by the compressor inlet.

The rotor dynamics appear to be unaffected by the homogeneously injected slugs, as no excitations near the natural frequency is seen. On the contrary, subsynchronous frequencies immediately disappears in all tests performed at rotating stall, even at small liquid flow rates. Because of the low plenum volume, the natural frequency of the compression system is estimated to be too high for subsequent slugs to produce resonating pressure waves. The test results are in agreement with this and no sign of pressure buildup is seen. Instead, the subsequent slugs leads to performance deterioration. A possible reason for this is that the rapid change of flow pattern leads to increased interaction between the phases and more severe friction losses through the compressor.

Regarding task 3 in the thesis problem statement, the author refers to the test results and states that within the range of the tests there is no upper limit on the acceptable slug levels with respect to flow instability in the compressor, since the slugs acts as stabilizers.

For further work, the author has two recommendations:

- Further investigation of the Continuous Wavelet Transform in order to document possible advantages over the Fast Fourier Transform for detection of wet gas transients.
- Investigation of the possibility for performing slug tests on the NTNU test rig with inhomogeneous water injection into the compressor.

BIBLIOGRAPHY

- [1] Z.I. Al-Hashami, H.H. Al-Kayiem, and R.W. Time. Experimental investigation on the vibration induced by slug flow in horizontal pipe. *ARPJ Journal of Engineering and Applied Sciences*, 2016.
- [2] ASME. *Performance Test Code on Compressors and Exhausters*. Standard PTC-10, 1997.
- [3] R. H. Aungier. *Centrifugal Compressors: A Strategy for Aerodynamic Design and Analysis*. ASME, 2000.
- [4] Y. Bai and Q Bai. *Subsea Pipelines and Risers*. Elsevier Ltd, 1st edition, 2005.
- [5] L.E. Bakken. *Thermodynamics, Compression and Expansion Processes*. Compendium TEP04 Gas Turbines and Compressors, 2016.
- [6] L. Baldassarre, M. Fontana, A. Bernocchi, F. Maiuolo, and R. Emanuele. Axial thrust in high pressure centrifugal compressors: Description of a calculation model validated by experimental data from full load test. *44th Turbomachinery Symposia*, 2015.
- [7] T.L Bergman, A.S. Lavine, F.P. Incropera, and D.P. DeWitt. *Fundamentals of Heat and Mass Transfer*. John Wiley Sons, 7th edition, 2011.
- [8] M. Boyce. Method and apparatus for compressor surge control. *U.S. Patent No. 3,901,620*, 1975.
- [9] M. Boyce. *Gas Turbine Engineering Handbook*. McGraw-Hill, 3rd edition, 2006.
- [10] L. Brenne. *Straight-walled diffuser performance*. PhD thesis, Norwegian University of Science and Technology, Norway, 2004.
- [11] L. Brenne, T. Bjørge, J.L. Gilarranz, J. Koch, and H. Miller. Performance evaluation of a centrifugal compressor operating under wet-gas conditions. *Proceedings of the 34th Turbomachinery Symposium*, 111-120, 2005.
- [12] G. Brun, K. and Marybeth. *Guideline for Field Testing of Gas Turbine and Centrifugal Compressor Performance*. Gas Machinery Research Council Southwest Research Institute, 2006.

-
- [13] S. Cao. Replicate the fourier transform time-frequency domains correspondence illustration using tikz, retrieved from <https://tex.stackexchange.com> 20/04/2017.
- [14] N.A. Cumpsty. *Compressor Aerodynamics*. Longman Scientific Technical, 1989.
- [15] I. Day, J. Williams, and C. Freeman. Rain ingestion in axial flow compressors at part speed. *ASME Turbo Expo 2005: Power for Land, Sea, and Air*, 2005.
- [16] A.G. de Jager. Rotating stall and surge control: a survey. *Proceedings of the 34th IEEE conference on decision and control*, 1995.
- [17] R. Dehner, A. Selamet, P. Keller, and M. Becker. Simulation of deep surge in a turbocharger compression system. *Journal of Turbomachinery* 138(11), 2016.
- [18] D. Eckhardt. Detailed flow investigations within a high speed centrifugal compressor impeller. *Trans ASME Journal of Fluids Engineering* 89, pp. 390-402, 1976.
- [19] EP. Leak halts subsea compression on gullfaks, retrieved from <http://www.epmag.com/>, 25/05/2017.
- [20] Veronica Ferrara. *Wet Gas Compressors - Stability and Range*. PhD thesis, Norwegian University of Science and Technology, 2016.
- [21] D.A. Fink. *Surge Dynamics and Unsteady Flow Phenomena in Centrifugal Compressors*. PhD thesis, Department of Aeronautics and Astronautics, Massachusetts Institute of Technology, Cambridge, MA, 1988.
- [22] P. Frigne and R. Van Den Braembussche. Distinction between different types of impeller and diffuser rotating stall in a centrifugal compressor with vaneless diffuser. *Journal of Engineering for Gas Turbines and Power*, 106, 1984.
- [23] D. Garcia and G. Liskiewicz. Stable or not stable? recognizing surge based on the pressure signal. *12th International Symposium SYMKOM 2016*, 2016.
- [24] J.T. Gravdahl and O. Egeland. *Compressor Surge and Rotating Stall: Modeling and Control*. Springer Publishing Company, 1999.
- [25] E.M. Greitzer. Surge and rotating stall in axial flow compressors, part i: Theoretical compression system model. *ASME Journal for Engine Power*, 98(2), pp. 190-197, 1976.
- [26] T.G. Gruner, L.E. Bakken, L. Brenne, and T. Bjørge. An experimental investigation of airfoil performance in wet gas flow. *Proceedings of ASME Turbo Expo 2008: Power for Land, Sea and Air*, 2008.
- [27] T.G. Gruner. Instability characteristic of a single-stage centrifugal compressor exposed to dry and wet gas. *Proceedings of ASME Turbo Expo 2012*, 2012.

- [28] Ø. Hundseid. *Evaluation of Performance Models for Wet Gas Compressors*. Norwegian University of Science and Technology, 2008.
- [29] Ø. Hundseid and L.E. Bakken. Integrated wet gas compressor test facility. *Proceedings of ASME Turbo Expo 2015: Turbine Technical Conference and Exposition*, 2015.
- [30] Ø. Hundseid, L.E. Bakken, T. G. Grüner, L. Brenne, and T. Bjørge. Wet gas performance of a single stage centrifugal compressor. *Proceedings of ASME Turbo Expo 2008: Power for Land, Sea and Air*, 2008.
- [31] National Instruments. Understanding frequency performance specifications, retrieved from <http://www.ni.com/white-paper/3359/en/>, 2016.
- [32] National Instruments. Measuring vibration with accelerometers, retrieved from <http://www.ni.com/white-paper/3807/en/>, 2016.
- [33] National Instruments. The fundamentals of fft-based signal analysis and measurement in labview and labwindows/cvi, retrieved from <http://www.ni.com/white-paper/4278/en/>, 2008.
- [34] R. Izmaylov and A. Lebedev. Centrifugal compressor surge detecting method based on wavelet analysis of unsteady pressure fluctuations in typical stages. *IOP Conference Series: Materials Science and Engineering*, 2015.
- [35] Brun K. and G.N. Nored. *Application Guideline for Centrifugal Compressor Surge Control Systems*. Gas Machinery Research Council Southwest Research Institute, 2008.
- [36] N. Kammer and M. Rautenberg. A distinction between different types of stall in a centrifugal compressor stage. *Journal of Engineering for Gas Turbines and Power Vol. 108/83*, 1986.
- [37] L. Kinsler, A. Frey, A. Coppens, and J. Sanders. *Fundamentals of Acoustics*. John Wiley Sons, 2000.
- [38] Liu L. and Hsu H. Inversion and normalization of time-frequency transform. *AMIS 6 No. 1S pp. 67-74*, 2012.
- [39] K.H. Lüdtke. *Process Centrifugal Compressors: Basics, Function, Operation, Design, Application*. Springer, 2004.
- [40] F. Marshall and J.M. Sorokes. A review of aerodynamically induced forces acting on centrifugal compressors, and resulting vibration characteristics of rotors. *Proceedings of the 29th Turbomachinery Symposium: 263-280*, 2000.
- [41] R.J. McKee and E.E. Carl. Method and apparatus for detecting the occurrence of surge in a centrifugal compressor. *U.S. Patent No. 6,981,838*, 2006.
- [42] S. Mokhatab, W.A. Poe, and J.G. Speight. *Handbook of Natural Gas Transmission and Processing*. Gulf Professional Publishing, 1st edition, 2006.

- [43] Jon Fredrik Müller. Subsea processing is making its way up the technology curve, but still several challenges ahead, retrieved from <http://www.rystadenergy.com>, 25/05/2017.
- [44] S. Ohuchida, T. Kawakubo, and H. Tamaki. Experimental study of rotating stall in vaneless diffuser of a centrifugal compressor. *Proceedings of ASME Turbo Expo 2013: Turbine Technical Conference and Exposition*, 2013.
- [45] Oil and Gas People. Statoil to install ‘world’s first wet gas compressor., retrieved from <https://www.oilandgaspeople.com>, 25/05/2017.
- [46] pcb.com. Introduction to dynamic pressure sensors, retrieved from <http://www.pcb.com/>, 06/03/2017.
- [47] D. Ransom, L. Podesta, M. Wilcox, M. Camatti, M. Bertoneri, and M. Bigi. Mechanical performance of a two stage centrifugal compressor under wet gas conditions. *40th Turbomachinery Symposium*, 2011.
- [48] M. Rennemo. Wet gas compressor surge detection. Master’s thesis, Norwegian University of Science and Technology, Norway, 2013.
- [49] I. Roumeliotis and K. Mathioudakis. Water injection effects on compressor stage performance. *ASME Turbo Expo 2006: Power for Land, Sea and Air*, 2007.
- [50] Goldman S. *Vibration Spectrum Analysis*. Industrial Press Inc., 2nd edition, 1999.
- [51] Liao S. and Chen J. Time-frequency analysis of compressor rotating stall by means of wavelet transform. *ASME 1996 International Gas Turbine and Aero-engine Congress and Exhibition, Volume 1: Turbomachinery*, 1996.
- [52] J. Sanjeev. Wet compression – a powerful means of enhancing combustion turbine capacity. *Power-Gen International, Orlando, FL*, 2002.
- [53] H. Saravannamuttoo, G. Rogers, and H. Cohen. *Gas Turbine Theory*. Pearson Prentice Hall, 6th edition, 2009.
- [54] H Schlichting and K. Gersten. *Boundary-layer theory*. Springer Science Business Media, 2000.
- [55] H. Skjefstad. Impeller stage instabilities. Master’s thesis, Norwegian University of Science and Technology, Norway, 2015.
- [56] G.G Stokes. On the theories of the internal friction in fluids in motion, and of the equilibrium and motion of elastic solids. *Transaction of the Cambridge Philosophical Society, vol.8, 22, pp. 287-342*, 1845.
- [57] G. Strang. Wavelets. *American scientist*, 1994.
- [58] L.A. Sørvik. Validation of wet gas surge phenomena. Master’s thesis, Norwegian University of Science and Technology, Norway, 2012.

-
- [59] A. Tijsseling and W. Dienstverlening. Fluid-structure interaction in liquid-filled pipe systems: Sources, solutions and unsolved problems. *Report IWDE: 02-05*, 2002.
- [60] S. Timoshenko, D. Young, and W. Weaver Jr. *Vibration Problems in Engineering*. John Wiley Sons, 1974.
- [61] R.A Van den Braembussche and B.M. Hande. Experimental and theoretical study of the swirling flow in centrifugal compressor volutes. *Journal of Turbomachinery* 112(1): 38-43, 1990.
- [62] G. Vannini, M. Bertoneri, G. Del Vescovo, and M. Wilcox. Centrifugal compressor rotordynamics in wet gas conditions. *43rd Turbomachinery and 30th International Pump Users Symposia*, 2014.
- [63] T. Wan and S.W. Wu. Aerodynamic analysis under influence of heavy rain. *24th International Congress of the Aeronautical Sciences*, 2008.
- [64] Y. Wang, G. Wang, S. Li, and Y. Sun. Analysis on effects of wet compression on surge margin of a small gas turbine. *2002 International Joint Power Generation Conference*, pp. 247-252, 2002.
- [65] F. M. White. *Fluid Mechanics*. McGraw-Hill, 7th edition, 2011.
- [66] A.B. Wood. *A Text-Book of Sound*. 1944.
- [67] E. Zachary and D. Hudson. Method and apparatus for achieving power augmentation in gas turbine via wet compression. *US Patent 5,867,977, The Dow Chemical Company*, 1999.

APPENDIX

A.1 Derivation of Helmholtz Frequency

A Helmholtz resonator consists of a cavity of gas with an open hole. The compressible gas inside the cavity can be modelled as a spring that oscillates when the resonator is subjected to an external periodic force. For instance, if the container is supplied with gas from a compressor that operates unsteadily. The model assumes the wavelength of the pressure waves to be much longer than the dimensions of the resonator. This means that it is possible to neglect the pressure variations inside the volume of the cavity.

Figure A.1 shows a model of a Helmholtz oscillator containing air in a cavity with volume V and pressure p , and a neck that with length L and cross sectional area A . The "plug" of air is then pushed a small distance x into the bottle and compresses the air so that the volume V is reduced to $V - Ax$, leading to an increased pressure in the cavity $p + dp$.

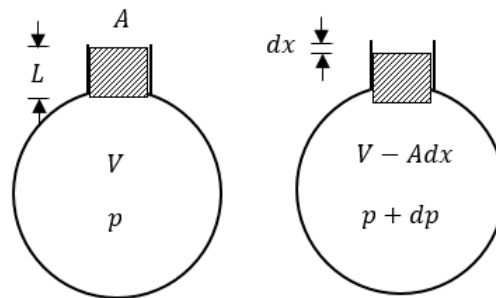


Figure A.1: Helmholtz resonator.

The increase in pressure can be found by assuming applying ideal gas behaviour and using the adiabatic compression relation. The pressure-volume relation is:

$$\frac{dp}{p} = -\gamma \frac{dV}{V} = -\gamma \frac{Adx}{V}$$

After the air "plug" has moved into the cavity it is subjected to a restoring force as a result of the pressure difference between the top and bottom of the neck dpA . A

term for the acceleration can be found by using Newton's Second law of motion

$$\frac{d^2x}{dt^2} = \frac{F}{m} = \frac{pA}{\rho AL} = -\frac{\gamma Ap}{\rho VL}x$$

This means that the restoring force is proportional to the displacement, which is the condition for simple harmonic motion. Simple harmonic motion has a frequency f that is $1/2\pi$ multiplied with the square root of the constant of proportionality, which gives:

$$f = \frac{1}{2\pi} \sqrt{\frac{\gamma Ap}{\rho VL}}$$

The term $\sqrt{\frac{\gamma p}{\rho}}$ is recognised as the speed of sound a . The Helmholtz oscillation frequency is then derived as:

$$f_H = \frac{a}{2\pi} \sqrt{\frac{Ap}{VL}}$$

A.2 Estimating the Helmholtz Frequency

The test rig configuration makes accurate prediction of the Helmholtz frequency difficult. It does not contain any clear boundary between the characteristic volume that produces the pressure oscillations and the plenum. In this case, the boundary between the diffuser and the volute was assumed to represent this boundary.

Because of the small outlet pipe, it would be inappropriate to neglect the volute volume. Unfortunately, the rate of cross-sectional area change in the volute was not known. However, the author got an opportunity to manually take measurement while it was being rebuilt. In order to calculate the volume of the volute it was instead divided into four segments, and the flow path inside each of them was assumed to follow the pattern of a circle segment, i.e. constant mean radius r_m . The volume was then calculated as for a truncated cylinder. The section from the volute tongue to the outlet pipe was assumed to have a constant rate of divergence. Figure A.2 and Figure A.3 illustrates the geometry and Table A.1 includes the measured parameters.

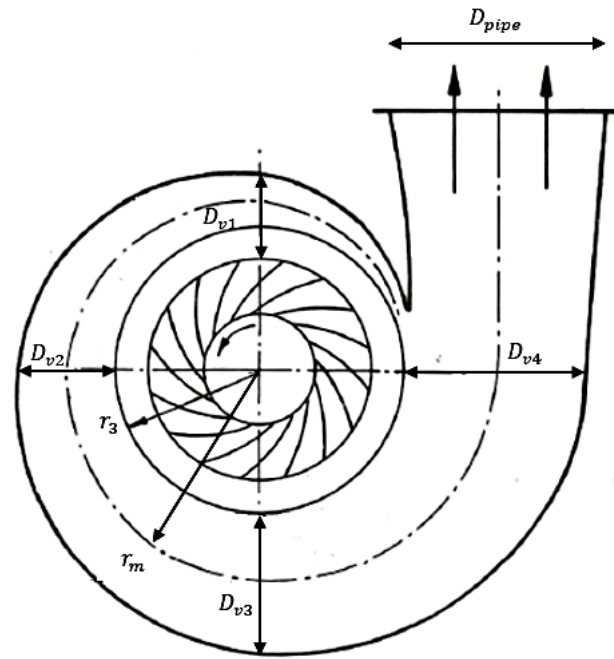


Figure A.2: Test rig volute geometry.

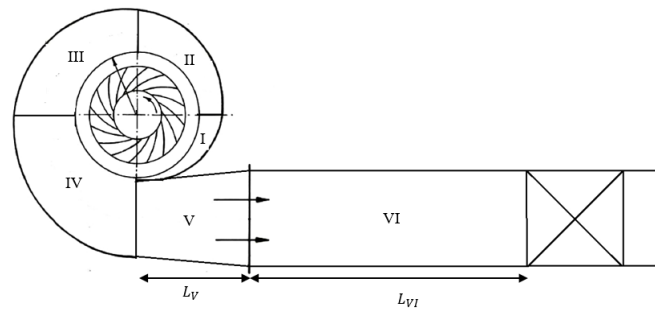


Figure A.3: Test rig compression system.

Table A.1: Plenum measurements.

r_3	0.380 m
D_{v0}	0
D_{v1}	0.077 m
D_{v2}	0.115 m
D_{v3}	0.137 m
D_{v4}	0.175 m
D_{pipe}	0.200 m
L_V	0.51 m
L_{VI}	2.48 m

The plenum volume can then be calculated:

$$V_p = V_I + V_{II} + V_{III} + V_{IV} + V_V + V_{VI}$$

where:

$$V_I = \frac{\pi}{12}(D_{v0}^2 + D_{v1}^2 + D_{v0}D_{v1})(\theta r_m)_I = \frac{\pi}{12}(D_{v0}^2 + D_{v1}^2 + D_{v0}D_{v1})\frac{\pi}{2}\left(r_3 + \frac{D_{v1} + D_{v2}}{2}\right)$$

$$V_{II} = \frac{\pi}{12}(D_{v1}^2 + D_{v2}^2 + D_{v1}D_{v2})(\theta r_m)_{II} = \frac{\pi}{12}(D_{v1}^2 + D_{v2}^2 + D_{v1}D_{v2})\frac{\pi}{2}\left(r_3 + \frac{D_{v1} + D_{v2}}{2}\right)$$

$$V_{III} = \frac{\pi}{12}(D_{v2}^2 + D_{v3}^2 + D_{v2}D_{v3})(\theta r_m)_{III} = \frac{\pi}{12}(D_{v2}^2 + D_{v3}^2 + D_{v2}D_{v3})\frac{\pi}{2}\left(r_3 + \frac{D_{v2} + D_{v3}}{2}\right)$$

$$V_{IV} = \frac{\pi}{12}(D_{v3}^2 + D_{v4}^2 + D_{v3}D_{v4})(\theta r_m)_{IV} = \frac{\pi}{12}(D_{v3}^2 + D_{v4}^2 + D_{v3}D_{v4})\frac{\pi}{2}\left(r_3 + \frac{D_{v3} + D_{v4}}{2}\right)$$

$$V_V = \frac{\pi}{12}(D_{v4}^2 + D_{pipe}^2 + D_{v4}D_{pipe})L_V$$

$$V_{VI} = \frac{\pi}{4}D_{pipe}^2 L_{VI}$$

The geometry of the compressor is given in table A.2.

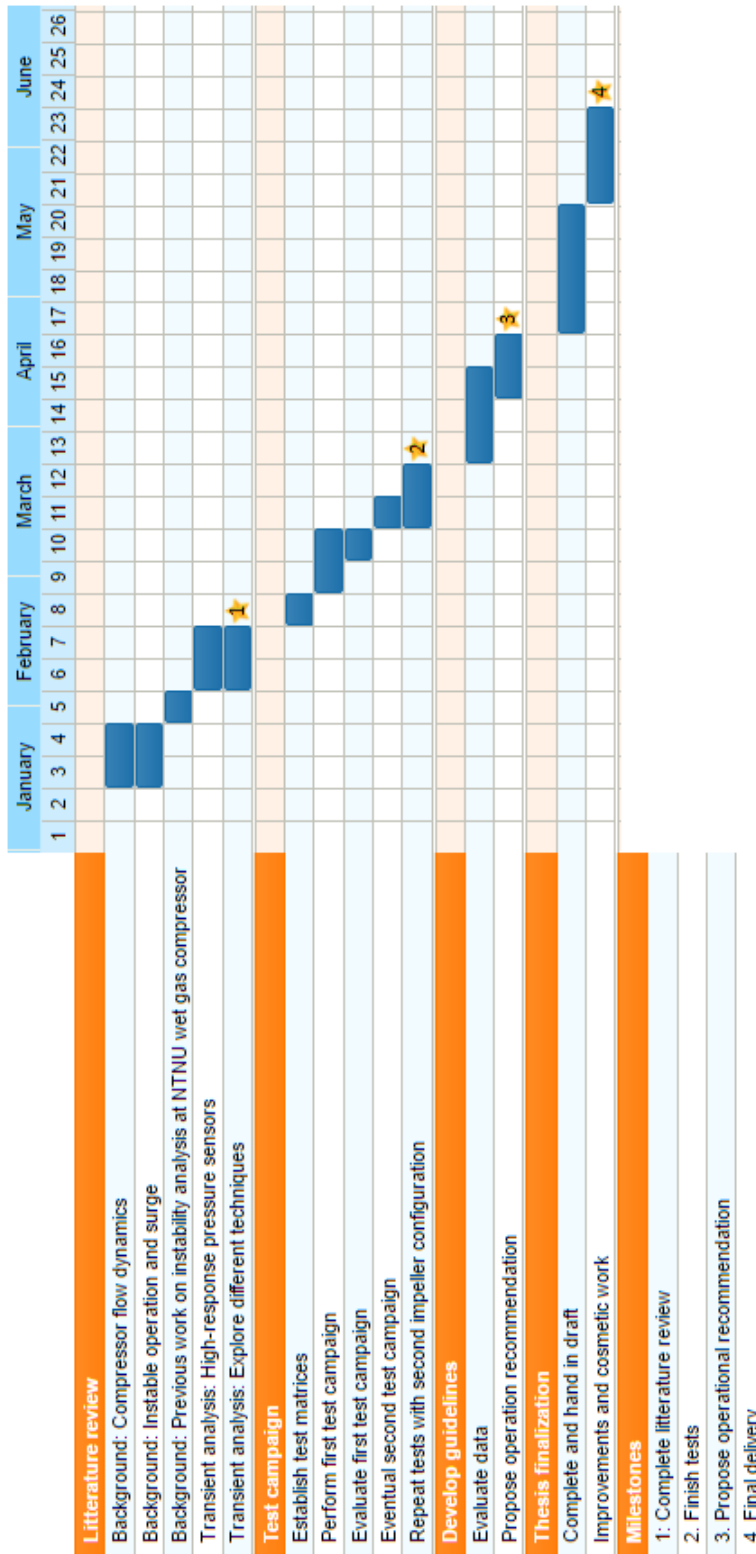
Table A.2: Compressor parameters

Diffuser ratio $r_3 - r_2$	150 mm
Impeller flow path	190 mm
Impeller eye area A_C	0.027 m^2
Impeller radius r_2	230 mm

The impeller eye area represents the characteristic area A_C and the diffuser ratio $r_3 - r_2$ together with an estimated impeller flow path length represents the Characteristic length L_C . The helmholtz frequency can now be given as a function of the speed of sound in the plenum:



$$f_H = \frac{a_p}{2\pi} \sqrt{\frac{0.027}{0.1246 * (0.150 + 0.190)}}$$

A.3 Research Plan



A.4 Risk Assessment

The following pages include the risk assessment performed by the author together with supervisor, in addition to *Attachment E: Procedure for Running Experiments* in the *Risk Assessment Report* for the wet gas compressor rig.

NTNU	Hazardous activity identification process	Prepared by	Number	Date	
		HSE section	HMSRV2601E	09.01.2013	
HSE		Approved by		Replaces	
		The Rector		01.12.2006	

Unit: Department of Energy and Process Engineering

Date:

Line manager: Olav Bolland

Participants in the identification process (including their function): Rig responsible Erik Langørgen and student Håkon Myklestad'

Short description of the main activity/main process: Master project for student Håkon Myklestad. Experiments on a wet gas compressor rig.

Is the project work purely theoretical? (YES/NO): No *Answer "YES" implies that supervisor is assured that no activities requiring risk assessment are involved in the work. If YES, briefly describe the activities below. The risk assessment form need not be filled out.*

Signatures: Responsible supervisor:



Student:



ID nr.	Activity/process	Responsible person	Existing documentation	Existing safety measures	Laws, regulations etc.	Comment
1	Compressor experiments dry/stable	Erik Langørgen	Risk Assessment Report	Procedure for Running Experiments	The Work Environment Act	Operating in unstable conditions is not explicitly covered in Procedure for Running Experiments
2	Compressor experiments wet/stable					
3	Compressor experiments dry/instable					
4	Compressor experiments wet/instable					
5	Compressor experiments slug					

NTNU	Risk assessment	Prepared by	Number	Date	
		HSE section	HMSRV2603E	04.02.2011	
HSE/KS		Approved by		Replaces	
		The Rector		01.12.2006	

Unit: Department of Energy and Process Engineering

Date:

Line manager: Olav Bolland

Participants in the identification process: Erik Langørgen (rig responsible) and Håkon Myklestad (student)

Short description of the main activity/main process: Master project for student Håkon Myklestad. Wet Gas Compression - Transients

Signatures: Responsible supervisor: *Erik Langørgen*

Student: *Håkon Myklestad*

Activity from the identification process form	Potential undesirable incident/strain	Likelihood: Likelihood (1-5)	Consequence:			Risk Value (human)	Comments/status Suggested measures
			Human (A-E)	Environment (A-E)	Economy/material (A-E)		
1	Loss of hearing and/or eyesight.	1	D	A	A	D1	Ear protection and eye protection.
2-5	Thermal or mechanical fatigue. Parts may detach, enter the rotating impeller and get flung out. Water accumulates in inlet pipe and pressure may build up.	1	D	A	D	D1	Gradually decrease flow. Closely monitor the liquid accumulation in inlet pipe during wet conditions. Stay in surge only for short periods. Avoid standing on the side of impeller.
5	Rapid increase of load. Risk of mechanical failure.	1	D	A	D	D1	Start with small slugs. Gradually increase size.

Likelihood, e.g.:


1. Minimal
2. Low
3. Medium
4. High
5. Very high

Consequence, e.g.:

- A. Safe
- B. Relatively safe
- C. Dangerous
- D. Critical
- E. Very critical

Risk value (each one to be estimated separately):

- Human = Likelihood x Human Consequence
 Environmental = Likelihood x Environmental consequence
 Financial/material = Likelihood x Consequence for Economy/material

NTNU  HSE/KS	Risk assessment	Prepared by	Number	Date	
		HSE section	HMSRV2603E	04.02.2011	
		Approved by		Replaces	
		The Rector		01.12.2006	

Potential undesirable incident/strain

Identify possible incidents and conditions that may lead to situations that pose a hazard to people, the environment and any materiel/equipment involved.

Criteria for the assessment of likelihood and consequence in relation to fieldwork

Each activity is assessed according to a worst-case scenario. Likelihood and consequence are to be assessed separately for each potential undesirable incident. Before starting on the quantification, the participants should agree what they understand by the assessment criteria:

Likelihood

Minimal 1	Low 2	Medium 3	High 4	Very high 5
Once every 50 years or less	Once every 10 years or less	Once a year or less	Once a month or less	Once a week

Consequence

Grading	Human	Environment	Financial/material
E Very critical	May produce fatality/ies	Very prolonged, non-reversible damage	Shutdown of work >1 year.
D Critical	Permanent injury, may produce serious serious health damage/sickness	Prolonged damage. Long recovery time.	Shutdown of work 0.5-1 year.
C Dangerous	Serious personal injury	Minor damage. Long recovery time	Shutdown of work < 1 month
B Relatively safe	Injury that requires medical treatment	Minor damage. Short recovery time	Shutdown of work < 1 week
A Safe	Injury that requires first aid	Insignificant damage. Short recovery time	Shutdown of work < 1 day

The unit makes its own decision as to whether opting to fill in or not consequences for economy/materiel, for example if the unit is going to use particularly valuable equipment. It is up to the individual unit to choose the assessment criteria for this column.

Risk = Likelihood x Consequence

Please calculate the risk value for "Human", "Environment" and, if chosen, "Economy/materiel", separately.

About the column "Comments/status, suggested preventative and corrective measures":

Measures can impact on both likelihood and consequences. Prioritise measures that can prevent the incident from occurring; in other words, likelihood-reducing measures are to be prioritised above greater emergency preparedness, i.e. consequence-reducing measures.

NTNU	Risk matrix	prepared by	Number	Date	
		HSE Section	HMSRV2604	8 March 2010	
HSE/KS		approved by	Page	Replaces	
	Rector	4 of 4	9 February 2010		

MATRIX FOR RISK ASSESSMENTS at NTNU

CONSEQUENCE	Extremely serious	E1	E2	E3	E4	E5
	Serious	D1	D2	D3	D4	D5
	Moderate	C1	C2	C3	C4	C5
	Minor	B1	B2	B3	B4	B5
	Not significant	A1	A2	A3	A4	A5
		Very low	Low	Medium	High	Very high
		LIKELIHOOD				

Principle for acceptance criteria. Explanation of the colours used in the risk matrix.

Colour	Description
Red	Unacceptable risk. Measures must be taken to reduce the risk.
Yellow	Assessment range. Measures must be considered.
Green	Acceptable risk Measures can be considered based on other considerations.

ATTACHMENT E: PROCEDURE FOR RUNNING EXPERIMENTS

Project Wet Gas Compressor		
Rig Wet Gas Compressor Rig		
Project leader Lars Eirik Bakken	Date	Signature
Plan for the experiment RPM LMF Goal Additional Equipment		

	Conditions for the experiment:	Completed
1	Experiments should be run in normal working hours, 08:00-16:00 during winter time and 08.00-15.00 during summer time. Experiments outside normal working hours shall be approved.	
2	One person must always be present while running experiments, and should be approved as an experimental leader.	
3	An early warning is given according to the lab rules, and accepted by authorized personnel.	
4	Be sure that everyone taking part of the experiment is wearing the necessary protecting equipment, (eyes and ear protection) and is aware of the shutdown procedure and escape routes.	
	Preparations	Carried out
6	Experiment area are tidy and clearly. Shut of the fire alarm for the rig area. Central by door to Kjelhuset, blue button	
7	Do visually inspection of the flanges and bolts on the impeller.	
8	Do visually inspection of the machinery shoes.	
9	Start the Labview programs The PXI : <ol style="list-style-type: none"> 1. Start Labview as administrator 2. Select Compressor monitor 3. Start Valve Controller, (IMPELLER HYDR/cRIO/Valvecontroller) 4. Startt Compressor monitor, (my computer/Main VI) Control PC <ol style="list-style-type: none"> 1. Start Labview 2. Impeller controller F500 temperature <ol style="list-style-type: none"> 1. Menu button 2. Scan external 3. Send to PC 	
	Start the hydraulic unit for the valves.	

	Write oil level:..... % , pressure after pump stops:..... Bar. Before filling of oil see MSDS Shell Tellus S3 M22	
	Starting up:	Carried out
10	Control air and wet-gas line Use a torch. Check air inlet, remove particles obstructions. Check visually outlet and inlet valve position. Start with valve in open position. Inside visual check of separator, Turn the impeller by hand. Should rotate unobstructed, listen for unusual sounds, (should be none).	
11	Control VSD , main button activated, emergency shutdown button not, (blue light)	
12	Start of lubrication unit. See that the run button is in off position. Start oil pump from control pc. Write: Oil level:.....% Pressure:.....bar (max 2,5 bar, ref. 3) Look for oil leaks, (tubing, bearings, connections and under bearing pedestal). Before filling of oil see MSDS Rando HDZ 46.	
13	Press reset button on control closet. If everything is ok, the checkmarks for lubrication are closed and green ok. <u>Do not run</u> the lubrication system without rotation of the shaft for more than one minute.	
14	Run the engine Put start button on desk in run position. If everything is ok, you'll have a green status in control system: Motor speed set to 2000 rpm. Operation below 2000 rpm to be avoided. Check for unusual sounds, vibration and leaks, visually inspection. Increase to 3000 rpm. When bearing temperature is approx. 30°C, increase speed step vice; to 6000 Resonance area at approx. 6300 – 7400 rpm to be avoided.	
15	Water injection tests Check water tank level and quality, filter in place and no obstructions. Check the waterline. Open the water cooling valve. Pump to be started at 10 Hz. Check suction and discharge pressure. Increase flow to required value, Check water flow meter, FT1.5	
	During experiments	Carried out
16	Frequent check of; -discharge temperature < 70° C , (limit of plexi) -discharge pressure, < 1.5 barA -oil pressure and level in tank -oil leakage -windings and bearing temperature -atmospheric conditions, humidity, water spill, smell -manual check of compressor casing temperature -water spill	
17	Notify any abnormal noise and vibrations.	
18	Avoid resonance speed area; 6300- 7400 rpm	
	End of experiment	
19	Discharge valve fully open	

20	Turn off the water pump. Close hydraulic valve for water.	
21	Close water injection valves before the nozzles.	
22	After water injection tests the rig has to be running for approx. 10 min in order to dry out any accumulated water.	
23	Compressor speed gradually reduced to 2000 rpm. Remain at 2000 rpm until the bearing temperature decreases, <70 ° C Stop utilizing «ABB VSD» control box to prevent restart.	
24	Stop the lube oil unit as soon as the shaft stops to rotate.	
25	Stop the VSD, run button and power switch.	
26	Remove all obstruction/barriers/signs around the experiment.	
27	Tidy up and clean-up work areas. Return all tools and equipment.	
29	Set equipment and systems back to their normal operation settings. Fire alarm, tubing, power supply.	
30	To reflect on before the next experiment and experience useful for others; <ul style="list-style-type: none"> • Was the experiment completed as planned and on scheduled in professional terms? • Was the competence which was needed for security and completion of the experiment available to you? • Do you have any information/ knowledge from the experiment that you should document and share with fellow colleagues? 	

Operator(s):

Name	Date	Signature
Erik Langørgen		
Øyvind Hunseid		
Martin Bakken		